DNA Scaffolds for Functional Hydrogels

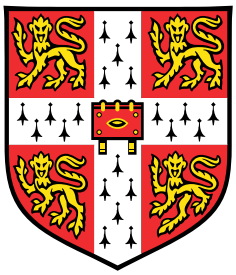

Zhongyang Xing

Department of Physics, Cavendish Laboratory

University of Cambridge

This dissertation is submitted for the degree of

Doctor of Philosophy

Jesus College

November 2018

This thesis is dedicated to my newborn baby,

who kicked the writing process along vigorously.

Declaration

This dissertation is the result of my own work and includes nothing which is the outcome of work done in collaboration except as declared in the Preface and specified in the text.

It is not substantially the same as any that I have submitted, or, is being concurrently submitted for a degree or diploma or other qualification at the University of Cambridge or any other University or similar institution except as declared in the Preface and specified in the text. I further state that no substantial part of my dissertation has already been submitted, or, is being concurrently submitted for any such degree, diploma or other qualification at the University of Cambridge or any other University or similar institution except as declared in the Preface and specified in the text.

This dissertation contains fewer than 60,000 words including appendices, bibliography, footnotes, tables and equations and has fewer than 150 figures.

The work within this thesis is partly based on the following articles:

Chapter 3:

Zhongyang Xing, Alessio Caciagli, Tianyang Cao, Iliya Stoev, Mykolas Zupkauskas, Thomas O'Neill, Tobias Wenzel, Robin Lamboll, Dongsheg Liu and Erika Eiser

Microrheology of DNA hydrogels

Proceeding of National Academy of Science (2018)

Chapter 4:

Zhongyang Xing, Christopher Ness, Daan Frenkel and Erika Eiser

Structural and linear elastic properties of DNA hydrogels by coarse-grained simulation

(Submitted to *Macromolecules*)

Chapter 5:

Yair Augusto Gutierrez Fosado, **Zhongyang Xing**, Erika Eiser and Oliver Henrich

A numerical study on three-armed DNA structures: an effect of inter bases on their topological features

(In preparation)

There are some side projects that I conducted during my PhD but not included in this thesis:

- Iliya Stoev, Alessio Caciagli, **Zhongyang Xing**, and Erika Eiser, "Using single-beam optical tweezers for the passive microrheology of complex fluids". *Optical Trapping and Optical Micromanipulation XV*. Vol. 10723. International Society for Optics and Photonics, 2018.

- Peicheng Xu, Yang Lan, **Zhongyang Xing**, and Erika Eiser. "Liquid crystalline behaviour of self-assembled LAPONITE®/PLL–PEG nanocomposites". *Soft Matter* **14**, no. 15 (2018): 2782-2788.

- Christopher Ness, **Zhongyang Xing** and Erika Eiser. "Oscillatory rheology of dense, athermal suspensions of nearly hard spheres below the jamming point". *Soft Matter* **13**, no. 19 (2017):3664-3674.

- Darshana Joshi, Dylan Bargteil, Alessio Caciagli, Jerome Burelbach, **Zhongyang Xing**, André S. Nunes, Diogo EP Pinto, Nuno AM Araújo, Jasna Brujic, and Erika Eiser. "Kinetic control of the coverage of oil droplets by DNA-functionalized colloids". *Science Advances* **2**, no. 8 (2016): e1600881.

Zhongyang Xing

November 2018

Acknowledgements

I started to draft my *Acknowledgements* in heart to people who I appreciate and truely thank since the beginning of my PhD. The list was getting longer and longer as time went on, and there was even a moment that I thought it would never end. Now the ending point finally comes, but I begin to find it so difficult to explicitly acknowledge all the help, support, stimulus and company that I have received during my past (nearly) four years in Cambridge. Still, I will try my best to do so.

First of all, I would like to thank my supervisor, Dr. Erika Eiser, who guided me through this long journey with great patience and warm care. Her tolerance to my silly faults and thoughtless actions encouraged me to explore new possibilities.

Special mention goes to people who spent their lives with me in the lab: Mykolas Zupkauskas and Darshana Joshi, for the initial guidance and company; Tine Curk, for the one-month crazy working shift day and night; Peian Li, for the endless maintenance of the equipment that you have never got a chance to use; Christopher Ness, for coming at the right time to use *this* equipment; Alessio Caciagli, for sharing the most hopeless microrheology time...

I would like to thank Dr. Christopher Ness, whose joining our group became a turning point of my PhD. Starting as an experimentalist, I would never have thought about initiating a simulation project on my own if not for his friendly encouragement and continuous help. This turns out to be the biggest decision on my PhD.

Talking about simulation, I cannot hide my sincere gratitude and admiration towards Prof. Daan Frenkel, who keeps inspiring me with his tremendous knowledge

and great kindness. I also benefit a lot from attending his group meetings and talking to his people, who are intelligent as well as welcoming.

Here I will not go into details about my other collaborators as their contributions are specified at the end of each chapter. But my best wishes to all my friends should not be skipped: Robin, for three years who seated by my side and knew my happiness and pain - I was even a bit struggling after you left; Mejd - I like the way you look at things; Sam, Angela & Kee - I miss so many lunches and festival feasts we used to have together; other friends in OE - you make the office time not that boring; my friends from Jesus College and NUDT community - you always make me feel like at home.

Robin should be mentioned again, for proofreading my thesis, and all the English 'teaching'. Other people who proofread the thesis in full or part are Erika, Chris, and Jeffery. I am very grateful to their useful comments and corrections.

Furthermore, I would like to extend my utmost wishes to all the Eiser Group members, past (Taiki, Rob, Simon, Darshana, Yang, Jerome, Zach...) and present (Talha, Myk, Peicheng, Alessio, Tom, Iliya, David and Iria), long-stay and short-visit (Clara, Tianyang, Peian...).

I also want to acknowledge National University of Defense Techonology for generously funding my PhD, and NanoDTC, Cambridge Philosophical Society and Jesus College for other subsidies.

The last special bit goes to my husband, Jiangbin Zhang, for always being by my side and supporting every single decision that I have ever made in my life. And of course, I should not forget about our unborn baby, because of whom this thesis comes out a couple of months earlier than it was planned to be.

Zhongyang Xing

August 2018

Abstract

DNA scaffolds self-assembled by short-stranded synthetic DNA can be tailored to build thermally reversible hydrogels with target binding sites. These hydrogels exhibit highly selective binding properties due to the specificity of DNA, and also provide an aqueous environment for various reactions to happen within the network constraints. Hence, a careful study on the assembly mechanism and other physical aspects of DNA hydrogels is required to facilitate the future design and construction of such materials at the precise control.

In this thesis I present the work on well-designed DNA nano-stars as scaffolds for functional bulk materials with potential applications in bio-sensing.

Chapter 1 starts with introducing the fundamental properties of DNA molecules, focusing on the advantages of utilising short-stranded DNA to programme and engineer micro- and macro- materials. Then it briefly reviews the field of rheology and micro-rheology, with the diffusing wave spectroscopy (DWS) technique illustrated explicitly as an example passive micro-rheology tool. Afterwards a critical literature review on computational modelling of DNA systems is present, followed by the thesis outline at the end.

Chapter 2 describes a simple DNA dendrimer systems self-assembled from three-armed DNA nano-stars. The characterisation tools such as UV-vis spectroscopy, gel electrophoresis and dynamic light scattering (DLS) are introduced to verify the final

production of the complex DNA structures. From this practice, we develop a routine for designing DNA scaffolds that yield optimal productivity.

Chapter 3 investigates the mechanical properties of DNA hydrogels made of three-armed DNA nano-stars and how they change upon cooling and heating empolying DWS micro-rheology. The resulting viscoelastic moduli over a broad range of frequencies reveal a clear, temperature-reversible percolation transition coinciding with the melting temperature of the system's sticky ends. This indicates that we can achieve precise control in mechanical properties of DNA hydrogels, which is beneficial for designing more sensitive molecular sensing tools and controlled release systems.

Chapter 4 develops a coarse-graining computational model of DNA hydrogels that resembles the system in Chapter 3 using LAMMPS, a classical molecular dynamics code. Thermodynamics, structural analysis and rheology tests were taken, qualitatively reproducing the physical phenomena of DNA assembly of the hydrogel network.

Chapter 5 studies the internal behaviours of three-armed DNA complexes using oxDNA model also implemented in LAMMPS, with particular focus on the effect of the inert bases in the core and between double-stranded branches and single-stranded sticky ends. A deep insight into sequence-dependent behaviour of such complex structures can guide the parameter optimisation of the individual building blocks for the model described in Chapter 4.

Chapter 6 concludes the thesis and presents an outlook for the future work that emerged out of my experimental and numerical studies.

Table of contents

List of figures

List of tables

Chapter 1

Introduction

1.1 Background: DNA as an intelligent glue

Since the double-helical structure of DNA (deoxyribonucleic acid) was first proposed by Watson and Crick in 1953 [1], DNA has been widely explored as carrier of genetic information as well as a generic bio-polyelectrolyte wifth interesting properties. In particular understanding the highly hierarchical packaging of DNA in chromosomes represents a challenging theoretical problem. Being found in all living bodies, DNA performs the crucial functions of storing and encoding genetic information. At the same time, its special physical and chemical properties as well as the easy synthesis of short strands have triggered ovefrwhelming interest in the field of materials science and engineering with control at the molecular level [2–4].

1.1.1 Chemical and physical properties of DNA polymers

Double-stranded DNA (dsDNA) consists of two single-stranded DNA (ssDNA) chains running anti-paralleled in terms of the sugar (3') and phosphate (5') ends of the backbone, which are bound to each other via hydrogen bridges between the nitrogenous

base guanine (G) and thymine (T), or cytosine (C) and adenine (A), as shown in Fig. 1.1(a). The ssDNA chain is a long flexible polymer chain in which each negatively charged sugar-phosphate repeat unit carries one of the four bases. In the linear, double-stranded form the bases G and C can form three hydrogen bonds (H-bonds) while the AT-pair only forms two H-bonds. Because of these topological constraints only two complementary ssDNA chains can bind fully to each other. Hence the sequence and directionality of complementary ssDNA provide a high specificity allowing the encoding of a large amount of information. Details of the chemical components of the nucleotides are illustrated in Fig. 1.1(b).

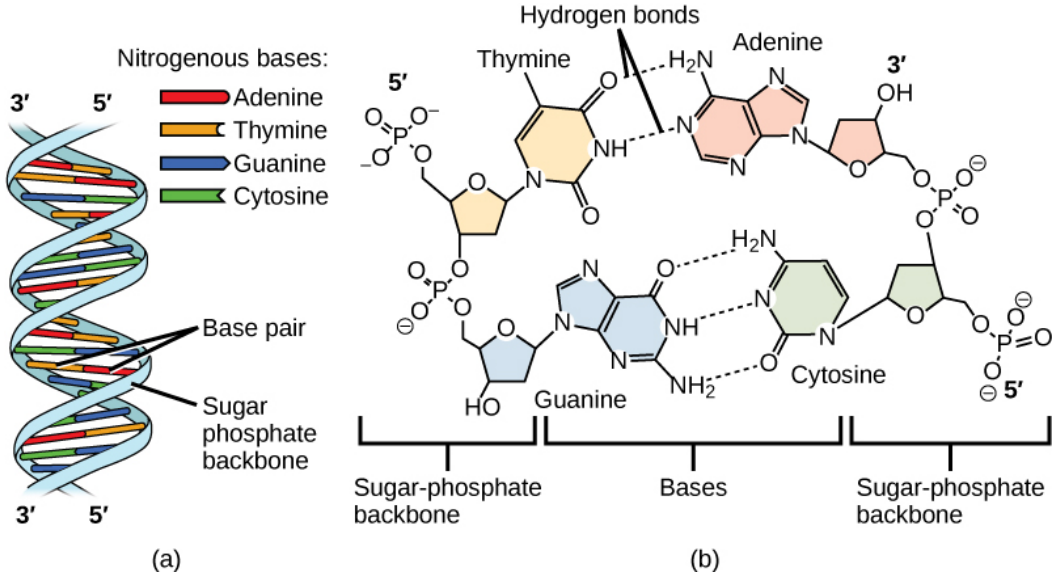

Fig. 1.1 Schematics of DNA structures. **(a)** Doulbe helical structure of DNA. **(b)** Chemical components of nucleotides. Image taken from [5].

The stability of DNA duplex is primarily dominated by the base pairing, but it is also affected by base stacking [6]. The base paring strength depends on the number of H-bonds given by the specific sequence used as well as external conditions such as temperature, pH and ionic concentration of the solvent, and even the DNA configurations that can be adopted. The typical energy of a H-bond varies from 1 to 40 kcal/mole, which is far weaker than covalent or ionic bonds [7]. Base stacking, on the

other hand, refers to the interactions between adjacent bases, which are hydrophobic and electrostatic in nature [6]. The strength of base-stacking interactions is comparable the to the strength of H-bond but it also depends on the next-neighbour (NN) pair, for instance AC/TG. There are 10 possible permutations of pairs in a linear duplex. This base-pair stacking interactions contribute to the twist in the double-stranded DNA structure.

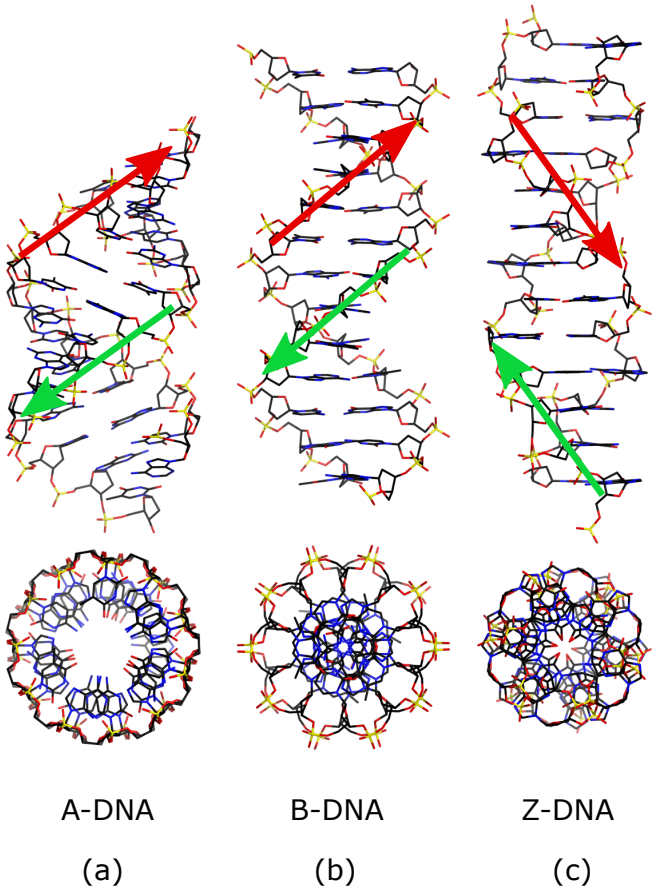

Fig. 1.2 Illustrations of the side and top views of the three commonly recognised DNA conformations: **(a)** A-DNA, **(b)** B-DNA and **(c)** Z-DNA. A-DNA and B-DNA are right-handed, where Z-DNA is left-handed. Red and green arrows indicate the 5'-to-3' directions of the two complementary ssDNA chains. The image is re-adapted from Ref. [8].

There are three commonly regarded types of dsDNA, namely A-DNA, B-DNA and Z-DNA, as is shown in Fig. 1.2. They differ from each other in geometry and

dimensions, and exist under different conditions. Here we shall focus on the B-form as it is the most commonly found conformation in nature; details about other conformations are detailed in Ref. [9–11]. The diameter of a B-DNA is 2.0 nm, and the distance between two consecutive base pairs alongside the chain is about 0.332 nm. As the twist angle between two adjacent base-pair stacks is approximately 36°, the helix undergoes a full turn every 10 bps (3.32 nm) [12]. Because the persistence length [1] of dsDNA is approximately 50 nm ($\approx$ 150 bp), it can remain fairly rigid for a couple of turns. On the other hand, ssDNA is rather floppy with the persistence length only at 1 nm ($\approx$ 3 bases). Since the dsDNA found in biological systems is normally at the length scale of several tens of kbp or above, they can be regarded as long flexible polyelectrolytes with physical properties and behaviour in aqueous conditions following the same scaling laws as synthetic polyelectrolytes. But in the more recently emerging field of structural DNA nanotechnology, researchers have started to play with short DNA strands that are synthesised via base-wise chemical reactions. The short DNA strands are normally about 100 bp long. The main advantage using short ssDNA is that one can programme their self-assembly into nano-scaled materials such as nanomachines or DNA origamis [3, 4, 13, 14].

Besides the most common double-helical chains, the hydrogen bonds in DNA may also form exotic DNA structures such as G-quadruplexes [15] and i-motifs [16] as is shown in Fig. 1.3 [17]. A G-quadruplex (also known as G-tetrad) is a square arrangement of guanines, which typically occur via Hoogsteen hydrogen bonding[2] when the DNA sequence rich in sequences with four consecutive guanines (G). Conversely, the i-motif is a cross-structure of four DNA strands based on intercalated C-C^+ base pairs. Holliday junctions are also possible [19] and shall be introduced in Chapter 2

[1] Persistence length is a parameter quantifying the stiffness of a polymer, within which the polymer is considered as 'rigid'.

[2] Hoogsteen hydrogen bonding is a variation of base-pair bondings in nucleic acids. Two bases are bonded via hydrogen bonds but in a different manner from Watson-Crick pairs [18].

with more details. Fig. 1.3 shows a schematic of a G-quadruplex (Fig. 1.3(a)) and an i-motif structure (Fig. 1.3(b)), both of which are widely studied in DNA-structure researches [20]. They used to be considered as 'unexpected structures' in the design of DNA self-assembly systems, which are normally dominated by Watson-Crick pairing, but nowadays they are becoming more popular for manipulating and constructing DNA nano-machines and -structures [21, 22]. Details of relevant research shall be introduced in the following section.

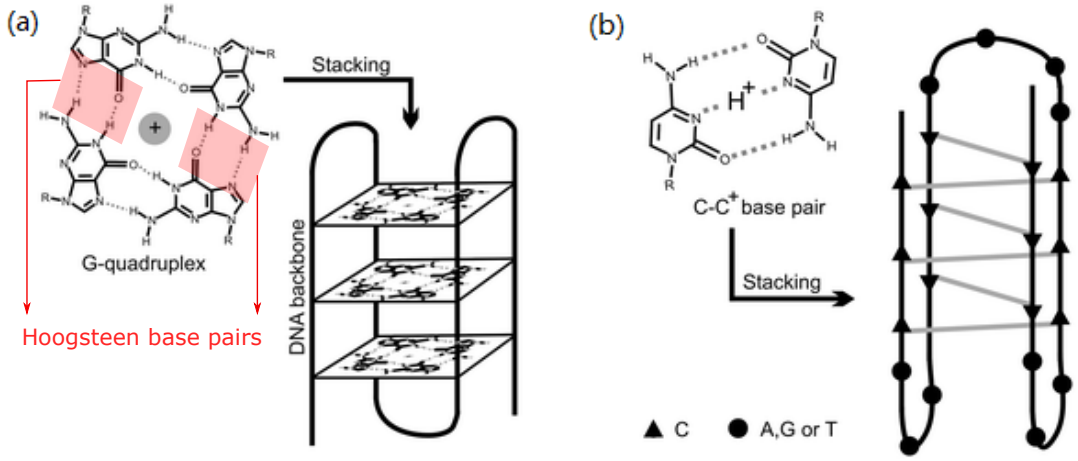

Fig. 1.3 Exotic DNA structures. **(a)** G-quadruplex: four guanines bind via hydrogen bonding. The resulting squares are stacked as depicted in the figure. **(b)** I-motif: a strand with many cystosines can make hydrogen bonds between these nucleotides at low pH. Image taken from [17]. © 2010 Royal Society of Chemistry.

1.1.2 DNA thermodynamics

DNA thermodynamics gives information on how temperature affects dsDNA melting and hybridisation, which refers to the disassociation and association of the hydrogen bonds between complementary oligo strands. It can be described by a chemical reaction shown in Fig. 1.4 *Top*, where AB stands for the duplex DNA, and A and B for the corresponding complementary ssDNAs. A typical parameter to characterise this process is the melting temperature T_m, at which half of the base-pairs in the AB duplex are

un-bound whilst the other half remains bound. For a detailed analysis of the chemical reaction and its relation to T_m, see the supporting information of Ref. [23].

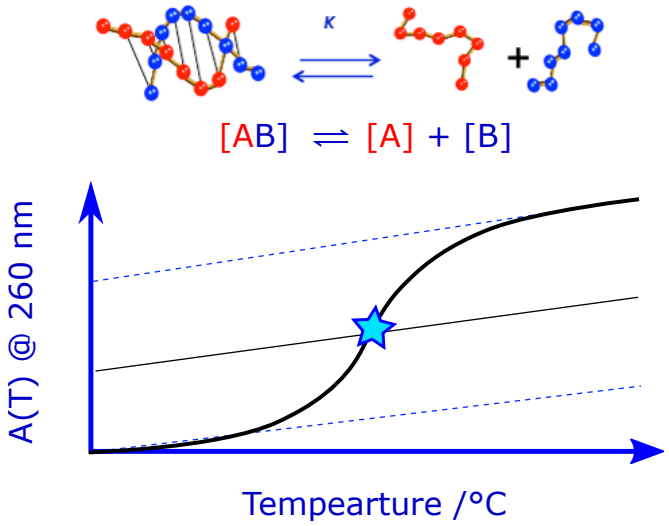

Fig. 1.4 Typical UV absorbance at 260 nm as a function of temperature observed for DNA melting. Linear base lines fitted to high- and low-temperature plateaus are drawn in dash. Melting temperature can be extracted from the crossover between the melting curve and the intermediate solid line.

Given a specific DNA sequence, the value of T_m can be theoretically calculated based on the Nearest-Neighbour (NN) model proposed by John SantaLucia [24]. In NN model, the Gibbs free energy ΔG° that describes the DNA hybridisation reaction is given by [24]

$$\Delta G^\circ = \sum_i n_i \Delta G^\circ(i) + \Delta G^\circ(\text{init}\frac{\text{w}}{\text{term}} G\cdot C) + \Delta G^\circ(\text{init}\frac{\text{w}}{\text{term}} A\cdot T) + \Delta G^\circ(\text{sym}). \quad (1.1)$$

In Eq. 1.1, the first term on the right-hand side is the sum of the contributions from all neighbouring base pairs in a row, with $\Delta G^\circ(i)$ being the standard free-energy changes for the 10 possible Watson-Crick NNs, the database of which are given in [24]. The second and third terms are initiation energies from A-T or C-G pairs at the two ends of the duplex, and the forth term comes from the sequence symmetry.

The Gibbs free energy ΔG° can also be expressed in terms of the system's enthalpy ΔH° and entropy ΔS°:

$$\Delta G^\circ_{\mathrm{T}} = \Delta H^\circ - T\Delta S^\circ, \tag{1.2}$$

with ΔH° and ΔS° being calculated in the same way as ΔG° done in Eq. 1.1 [25, 24]. T_m can then be computed from the measured ΔH° and ΔS° that are tabulated, following the equation:

$$T_m = \Delta H^\circ / (\Delta S^\circ + \mathrm{R} \ln C_{\mathrm{T}}). \tag{1.3}$$

Here R=1.987 cal/Kmol is the gas constant and C_{T} is the total ssDNA concentration[3]. Note that the added NaCl concentration is also considered in the NN model, which enters as additional term in Eq. 1.1 [24]. However, the so-called 'inert tails' that are dangling on the DNA ends without being involved in the hybridisation process had not been taken into account, and was only recently discussed by Di Michele *et al.* in Ref. [23].

Experimentally, the melting (or hybridisation) process of dsDNA is depicted in Fig. 1.4, where the absorbance of a DNA solution is measured at 260 nm as a function of temperature using UV-vis spectroscopy. This is because ssDNA absorbs the wavelength of 260 nm about 37 % more than dsDNA. Hence, one observes a plateau in the UV-vis data well above the melting temperature of DNA when all duplexes are melted, while the plateau at lowest temperature is established when all allowed base pairs are formed. Normally, there is no hysteresis between the cooling and heating ramps for equilibrium hybridisation. The melting temperature is defined as the temperature at which half of all hydrogen bonds are unbound and can be defined as the median between the two measured plateaus (marked by the star in Fig. 1.4).

[3]More details about the deduction see Section 4.3.1.

1.1.3 Examples of DNA-based smart materials

Due to the highly specific binding properties, DNA (particularly ssDNA) can serve as an intelligent 'glue' to adhere building blocks with its complementary counterpart. For instance, ssDNA-coated colloids (DNACCs) have been widely used to direct the specific aggregation of micron- or nano-sized particles since 1996 when this strategy was first proposed [26, 27]. Over the past decades, many research studies on DNACCs have boosted this topic, in particular the formation of DNA-programmed nanocrystals [28–31], DNA-intermediate colloidal-gels [32–36] and their utilizations as frameworks and sensors [37, 38]. Also colloidal oil droplets were successfully surface coated with short DNA strands to achieve directed assembly [39–43]. One advantage of using emulsion droplets is the mobility of the linkers on their liquid interface, which gives an extra degree of freedom that may allow aggregated oil droplets (with sizes ranging from 20 nm to 10 µm in diameter) to re-arrange even after aggregation [40].

Apart from forming 'bridges' for other materials, DNA can also self-fold into complex structures. A well-known example are DNA origamis that can form 2D or 3D nanoscale architectures fabricated by a single, long genome DNA strand with numerous short ssDNA staples that attach to specific binding sites on the long one [13, 44–46, 45, 47]. Since the feasibility of DNA origamis was first demonstrated in 2006 [13], researchers' enthusiasm and passion of building up more 'fancy' origami structures has expanded [44–46, 45, 47]. In 2012, Peng Yin's group published a new design strategy of DNA origami, where the long 'scaffold' DNA is not needed anymore; instead, thousands of pre-designed ssDNA can self-assemble into target frameworks themselves [48]. To distinguish their approach from the traditional origami folding, they gave it the name 'DNA bricks' - because the ssDNA strands can be used like 'Lego-bricks' that can be stacked to form a 3D structure. In 2017, the same group reported a different DNA origami folding approach in which a single long ss- DNA or RNA is able to fold on its

own [49]. Fig. 1.5 presents these three typical origami folding approaches. Though being demonstrated to self-fold into arbitrary eye-catching user-prescribed shapes, DNA origamis have not yet proved to be affordable materials for making functional frameworks or devices in reality due to its incredibly high cost.

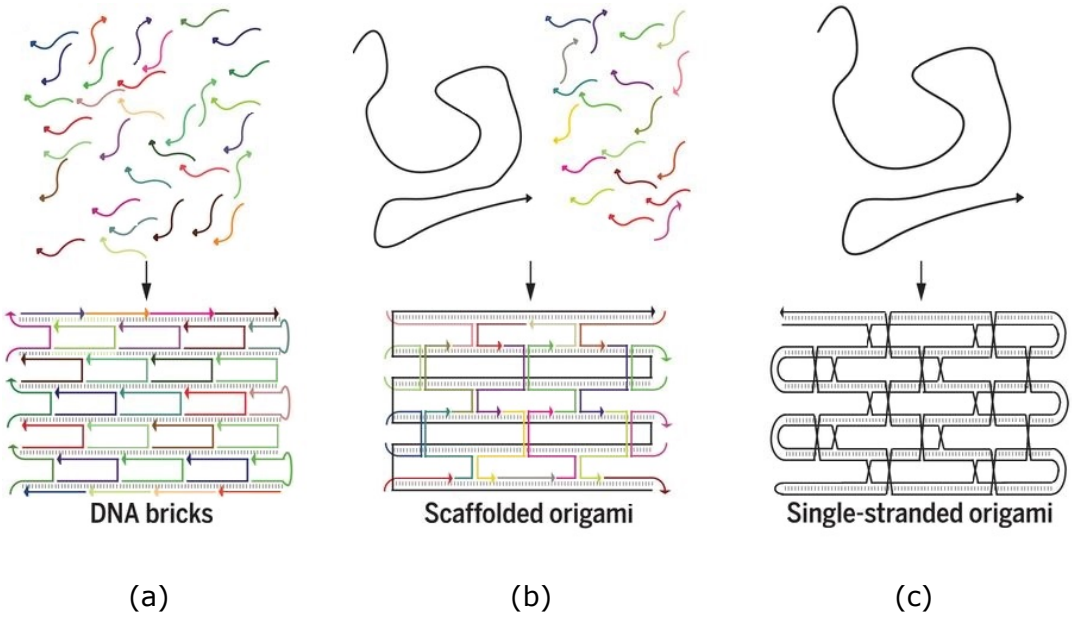

Fig. 1.5 Cartoon comparing different folding strategies such as **(a)** DNA bricks, **(b)** scaffold origami and **(c)** single-stranded DNA or RNA origami. The image is taken from [49]. © 2017 The American Association for the Advancement of Science.

Unlike densely-packed origami, DNA hydrogels have less ordered structures but more empty space within the framework, which can retain huge amounts of water. I will present a detailed literature review on DNA hydrogels in the following section 1.2. While I do not cover all aspects of DNA-functionalised materials and DNA-based nanotechnology here, some important publications on assisting rational design and precise control of nano-materials and devices can be found in several references [50–54, 2].

1.2 DNA hydrogels

DNA hydrogels are semi-flexible polymeric networks made of well-defined DNA building-blocks that are connected to each other either via chemical or physical crosslinkers [55, 20]. These man-made bulk DNA hydrogels (pure or hybrid) have been widely studied as functional materials that can be potentially used for controlled drug delivery [56–58], tissue engineering [59], bio-sensing [60], bio-printing [61, 62] and other applications in the fields of nanotechnology and bioengineering mainly because of their bio-compatibility and the ability to mix them with other (bio)polymers. While current studies mostly focus on the fabrication [63–66] and utilization [67] of DNA hydrogels, the fundamental physics relating the microstructure of these gels to their macroscopically observed viscoelastic properties still lacks good understanding. This motivated us to employ microrheology to investigate the mechanical properties of DNA hydrogels at the micro-length scale, which may further facilitate the design of more sensitive molecular sensing tools and controlled release systems.

There are different ways of categorizing DNA hydrogels, one of which is by the type of crosslinkers that associate the network. In this section, I will first introduce current research on DNA hydrogels conducted by various research groups sorted by the crosslinking strategy: ligation, i-motif and DNA hybridisation. One should also note that here I deliberately left out the DNA hydrogels that are formed via physical entanglement of natural, long DNA strands [68–70]. Then I will briefly discuss the hydrogel system that I have been working on. As review of rheology and microrheology will be presented in the next section.

The first DNA hydrogels were reported in 2006 by Soong Ho Um *et al.* [56], where self-assembled branched DNA were constructed into bulk hydrogels via ligase-catalysed reactions (Fig. 1.6(a)). The 4-base-long sticky ends of branched DNA were hybridized with their complementary counterparts, and the separated phosphate backbones were

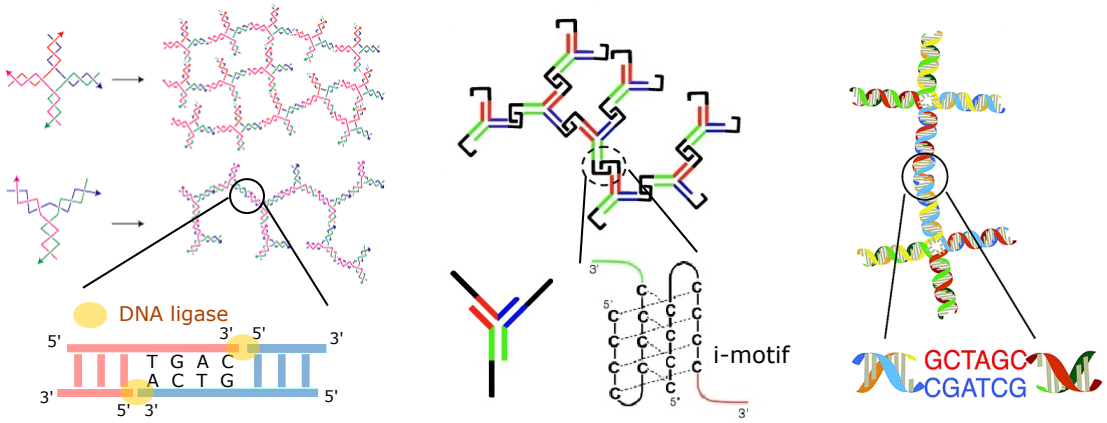

Fig. 1.6 Cartoons illustrating different crosslinking strategies for DNA hydrogels: **(a)** DNA ligation, **(b)** i-motif structure and **(c)** DNA hybridisation. Image (a) was taken from from [56], © 2006 Springer Nature; (b) from [71], © 2009 John Wiley and Sons; (c) from [72] © 2015 Royal Society of Chemistry.

then joint together covalently with the help of a DNA ligation enzyme [56]. DNA ligation creates stronger connections between DNA monomers, but the irreversibility of the gelling process may reduce our control over these smart materials.

Dongsheng Liu's group later proposed a strategy of using the 'i-motif' structure (see sec. 1.1) as switchable crosslinkers to form and deform DNA hydrogels (Fig. 1.6(b)) [71]. These DNA hydrogels can switch between sol-gel states by simply controlling the environmental pH values, as i-motifs are only stable within pH 3 to 7, depending on the sequences and total ionic strength used [20]. Based on the i-motif interlocking, hybrid DNA hydrogels with pH-sensitive functional properties (e.g. swelling) and applications (e.g. sensing, and controlled releases) have also been thoroughly explored over the past decade [73–80]. However sensitive the response is, the i-motif structures can only achieve a single recognition and thus respond to a single stimulus (sometimes more than one, but only in hybrid DNA hydrogels where other stimuli are introduced by

other components). Hence, the most powerful aspects of DNA, *i. e.* its high specificity, is lost in this type of systems.

Here we come back to the most classic way of using DNA as an intelligent glue - DNA hybridisation via Watson-Crick pairing (see Fig. 1.6(c)). It provides a unique way to achieve programmable self-assembly of thermally reversible gels with precise functionality. An example are hydrogels that are self-assembled from 2-, 3-, and n-valent DNA nanostars and their mixtures that were investigated by the group of Sciortino [81, 82]. They have carried out a series of computational and experimental studies focusing on the phase diagram and dynamics of DNA hydrogels at various temperatures and concentrations, providing a good reference for creating thermally reversible, percolating gels upon cooling [72, 81–90].

In this thesis, I specifically discuss one class of DNA hydrogel that is self-assembled from tri-valent DNA-nanostars, which we refer to as Y-shapes or Y-DNA. These are made of 3 ssDNA chains that are partially complementary so that they form a core of three dsDNA arms that carry the same sticky ssDNA ends. On their own these Y-shapes (formed at higher temperatures) cannot hybridize to each other at any temperature as they all have the same ends. Hence we mix them with Y'-shapes, which have the same dsDNA core but complementary sticky ssDNA ends. As I will show later, the T_m of the complementary overhangs of the Y- and Y'-DNA nanostars was designed such that they form well below the melting temperature of the Y-shapes themselfs. Their 1:1 mixtures then from thermally reversible, viscoelastic hydrogels.

1.3 Rheology and micro-rheology

Rheology is a study of how matter deforms and flows when expose to an external force. The system can be solid-like (simple solids), fluid-like (simple fluids), or displaying an intermediate behaviour (complex fluids). Simple solids are described by their

elasticities, *i. e.* the deformation in response to an applied stress, while simple liquids are characterized by their viscosity, which a material property. Most soft materials exhibits both properties, hence they are called viscoelastic. Examples are colloidal suspensions, emulsions, polymer melts and solutions, liquid crystals, or surfactant phases [91, 92].

1.3.1 Bulk rheology

The linear viscoelasticity of a complex fluid is normally measured by applying a modest, oscillatory deformation giving the storage modulus $G'(\omega)$ and the loss modulus $G''(\omega)$ [91]. The measured response reveals the mechanical and fluid properties of the material at various angular frequencies ω corresponding to different timescales and therefore the underlying structures [93]. Traditionally the shear moduli of complex materials are measured using a mechanical or bulk rheometer, which usually requires macroscopic amounts of the sample under investigation. In the linear viscoelastic regime the frequency-dependent moduli $G'(\omega)$ and $G''(\omega)$ can be calculated following the Eq. 1.4 [91],

$$\sigma(t) = \gamma_0[G'(\omega)\sin(\omega t) + G''(\omega)\cos(\omega t)], \tag{1.4}$$

where $\sigma(t)$ is the time-dependent shear stress, γ_0 is the strain amplitude, and ω is the angular frequency of the applied shear stress. $G'(\omega)$ and $G''(\omega)$ can be combined into the complex modulus $G^*(\omega)$ via Eq. 1.5:

$$G^*(\omega) = G'(\omega) + iG''(\omega). \tag{1.5}$$

The ratio of G'' and G' determines whether the material is more solid-like (when $G''/G' < 1$) or liquid-like (when $G''/G' > 1$).

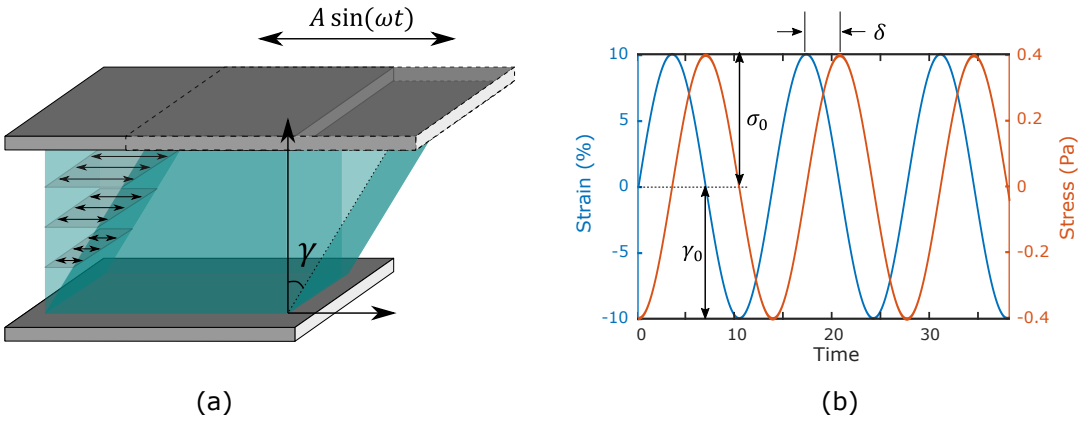

Fig. 1.7 **(a)** Illustration of oscillatory shear, applying a time-dependent sinusoidal deformation. **(b)** Oscillatory test for viscoelastic behaviour, presented as a sinusoidal function versus time, e.g. with preset shear strain and resulting shear stress; the two curves are offset by the phase shift δ.

As mentioned before, one disadvantage of using traditional bulk rheology is the requirement of large sample volumes ($\sim$ ml or more). Further, due to the high inertia of the geometries used in bulk rheology (such as cone-plate or Couette-geometries) frequencies only up to a few hundred Hz can be reached, which means only true bulk properties and very slow dynamics can be tested. Furthermore, the sample cells are usually open to the environment. Hence evaporation can interfere with high temperature and long-time experiments. These limitations encouraged the development of microrheology techniques that relay on measuring the motion of micron-sized probe particles embedded in the materials of interest [92, 94, 95].

1.3.2 Micro-rheology

Current microrheological techniques can be categorized into 'active' and 'passive' microrheology, with the distinction being whether the motion of probe particles embedded is driven by an applied external forces (the former) or by simply measuring the thermal motion of that probe particle. In recent decades, the evolution in instrumentation has

boosted the development of the field of microrheolgy. Active microrheology relies on state-of-the-art instruments that can supply driving forces that are able to manipulate sub-micron particles, such as optical tweezers [96–98], magnetic tweezers (when using fereomagnetic beads) [99–101], and AFM tips [102, 103]. Passive microrheology is mainly based on particle tracking or light-scattering techniques (single or multiple scatterings) that can detect the thermal motion of either the embedded probes or the materials themselves. But also weak trapping of the probe bead and monitoring its thermal fluctuations in time is a form of passive microrheology. Fig. 1.8 illustrates a schematic representation of single-particle video tracking based on an optical tweezer setup in our lab; for more details please see [104]. In the following context, we shall briefly introduce diffusing-wave spectroscopy (DWS), which is another microrheology technique that was used in this thesis.

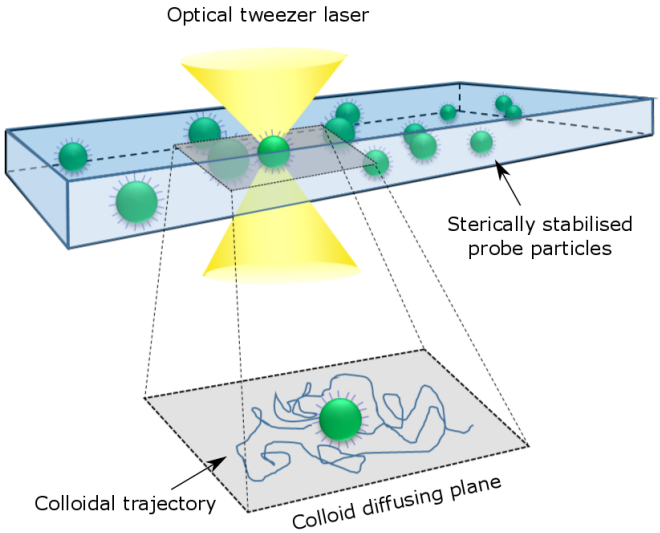

Fig. 1.8 Illustration of a passive micro-rheology setup based on an optical tweezing technique to extract rheological parameters of a sample from the trajectory of the embedded probe colloids.

Diffusing-wave spectroscopy (DWS), a technique that measures the dynamics of strongly scattering samples [105, 106] is an established technique to perform microrheo-

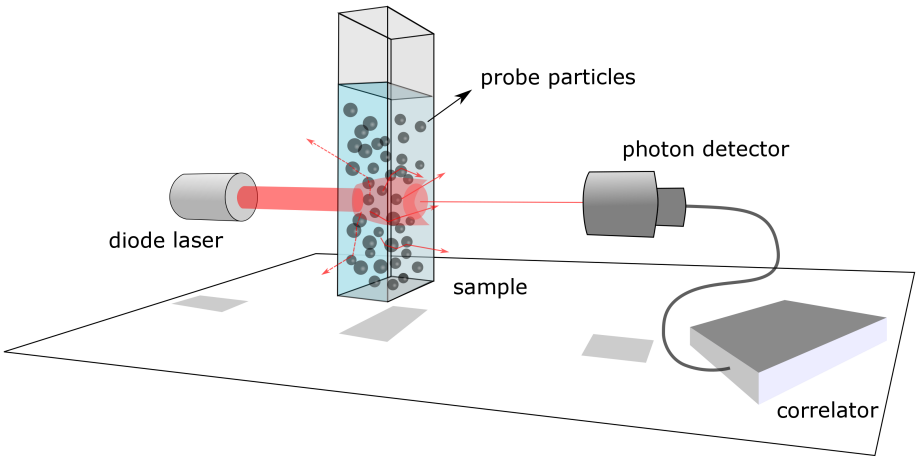

Fig. 1.9 Schematic illustration of the diffusing-wave spectroscopy (DWS) setup: a 685 nm diode laser beam impinges onto the sample, and the diffusely scattered light is collected by the photodiode on the other side of the sample. Probe particles are uniformly embedded inside the sample.

logical studies of complex fluids at much shorter time and length scales than conventional bulk-rheology can achieve [107–110]. DWS measurements rely on time correlations of diffusively scattered light caused by submicron-sized spherical tracer particles embedded in the measuring sample (see Fig. 1.9). The thermal motion of the particles is described by the mean-square displacement (MSD), denoted as $\langle \Delta r(t)^2 \rangle$. This is measured by the real-time fluctuations of the scattered light collected by a photon-detector and presented as the intensity-autocorrelation function (ICF), $g_2(\tau) = \langle I(\tau)I(0) \rangle_t / \langle I(0) \rangle_t^2$, where $I(0)$ and $I(\tau)$ are the scattered intensities at time zero and some delay time τ later. The decay of $g_2(\tau)$ is related to the time evolution of particle motion, allowing for the MSD of the particle to be measured [105]. The complex viscoelastic modulus and MSD are related to each other through the generalized Stokes-Einstein relation (GSER) given in Eq. 1.6, assuming the fluctuation-dissipation theorem holds[107, 106]:

$$\tilde{G}(s) \approx \frac{k_B T}{\pi R s \langle \Delta \tilde{r}^2(s) \rangle}. \tag{1.6}$$

Here $\tilde{G}(s)$ and $\langle \Delta \tilde{r}(s)^2 \rangle$ are the Laplace transforms of the complex shear modulus and the MSD; R is the radius of the tracer particles, and s the Laplace frequency. By replacing s with $i\omega$ we obtain the $G'(\omega)$ and $G''(\omega)$ from the complex shear modulus $G^*(\omega) = G'(\omega) + iG''(\omega)$ [106, 107]. Data analysis of DWS microrheology see Appendix B.0.3.

1.4 Computational modelling of DNA

Computational modelling of DNA and DNA-based systems emerged in the 1980s [111, 112] and has been greatly expanded in the past few decades [113–118]. These models are coarse-grained (CG) at different levels to address the thermodynamic and physical properties of DNA systems at differetn time and length-scales (Fig. 1.10). For example, in the field of biology, DNA folding and its interaction with proteins is often emphasised, which requires a deep understanding of DNA conformation and mechanics [119–124]. On the other hand, in non-biological systems, where DNA is normally treated as an interacting medium bridging other building blocks, the accurate prediction of DNA self-assembly that represent the programmability of DNA sequences is of importance [125–133]. These simulation models allow for a more efficient way to charaterize the vast parameter space in DNA systems, thus replacing some of the exhaustive and costly experiments of designing and exploring new DNA systems.

Atomistic models of DNA simulation (Fig. 1.10(a)), where short DNA strands (usually tens-of-bps long) are represented by a set of atoms employed with classical force-fields such as CHARMM [136] and AMBER [137], provide the highest level of details on DNA crystal structures [134, 138, 139]. In such models, interactions between all the atoms in DNA molecules and the surrounding solvent are considered; thus, the performance of a model is mainly dominated by the accuracy of its force-field

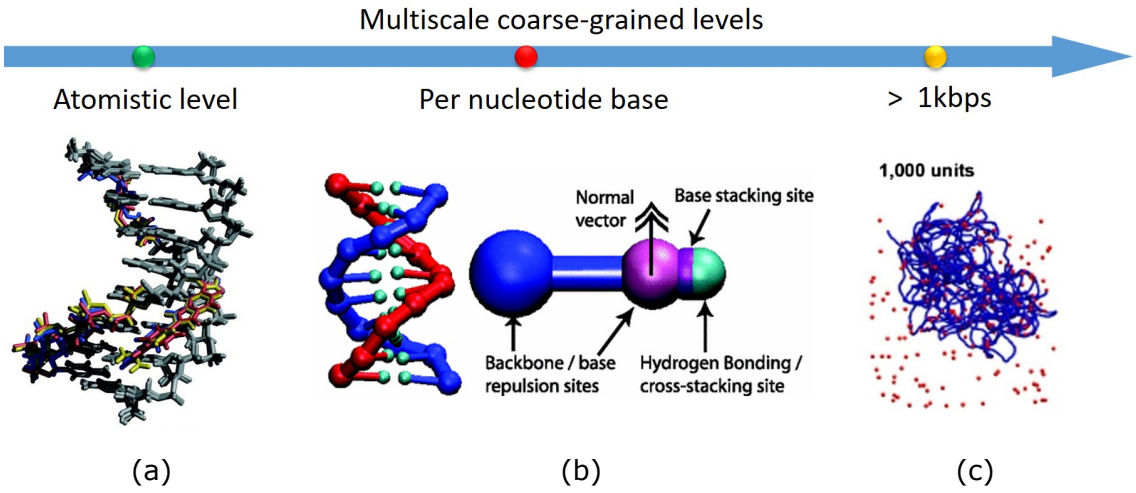

Fig. 1.10 Examples of DNA simulation models at different coarse-grain levels. **(a)** Atomistic DNA model exploring nucleic acid structures influenced by solvent and ions. Image taken from [134]. **(b)** oxDNA model to study the thermodynamics and configuration of short DNA strands. Image taken from [128]. **(c)** Genomic DNA model investigating DNA-binding proteins and genome organization. Image taken from [135].

approximation[4]. These models have been successfully applied to study the mechanical behaviours of short pieces of DNA such as stretching, twisting and bending, and also to simulate DNA recognition by other molecules such as ligands and proteins [113, 117]. However, the price is high to keep the fullest information at the all-atom level, as the heavy calculation limits the length-scale ($\lesssim$ 100 bps) and time-scale ($\lesssim$ µs) of DNA systems one can play with.

The worm-like chain (WLC) model describes long, flexible polymer chains by a string of connected beads with bond, angle and rotation restrictions. It can be adapted to represent long strands ($\gtrsim$ kbps) of dsDNA molecules [116, 12] (Fig. 1.10(c)). In DNA computational models using the WLC theory, each bead is uniformly packaged with segments of dsDNA that can vary on length scales from several bps to kbps from case to case. These models are normally parameterised by the persistence length of dsDNA, and result in good agreement with experimental data for diffusion and

[4]A detailed literature review of force-fields in atomistic models can be found in [117].

structural relaxation of long DNA chains [114, 116]. Though low in resolution, they are sufficient and efficient enough to study large DNA systems, e.g. DNA wrapping into chromatin, where a higher level of details is not relevant [135, 140].

The rapidly growing field of DNA nanotechnology utilising the pairwise recognition of DNA sequences has accumulated vast experimental data, and the design of DNA-based nanoscale materials is in great demand [141]. Computational models that can capture the essential physics of DNA melting and hybridisation transitions would facilitate the design process and dramatically save the testing cost in experiments. However, neither atomistic nor WCL models are ideal to achieve this goal. Therefore, an intermediate coarse-graining level of DNA simulation model is in need to represent the conformational and thermal properties of short DNA strands (10 $\sim$ 1000 bps). These CG models can be divided into two groups according to whether the parameterisation strategy is a *top-down* approach [130, 141–144], where the interactions are empirically parameterised to match the available experimental data, or a *bottom-up* one [145–147], where the force fields are vigorously extracted from reference atomistic simulations. In the following text I will introduce two notable models, namely the 3SPN and the oxDNA model, both of which are based on top-down approaches. I refer to Ref. [114] for a comprehensive overview of other models at similar coarse-graining levels.

Juan de Pablo's group reported the first **3-S**ite-**P**er-**N**ucleic (3SPN) coarse-grained model for DNA in 2007 [130], which reduces the complexity of a nucleotide into three interaction sites corresponding to the phosphate (P), sugar (S) and the base (b). Among these, the base sites are further specified into four subcategories (Ab, Tb, Cb and Gb), each representing one type of base in DNA. The coordinates of each site are determined accordingly from those of a standard B-form DNA, in order to map the basic geometry of a DNA duplex with the major and minor grooves included explicitly. Isotropic potentials are applied to feature base-paring and base-stacking interactions,

and electrostatic forces are also considered as a key element. By successfully reproducing the persistence length of ssDNA and dsDNA, salt-dependent melting temperatures and the dynamics of bubble formation using this model, 3SPN proves to be a reasonable description of DNA at the molecular level. Subsequent efforts have been made by the same group to refine the original 3SPN model, ending up with the 3SPN.1 model [148] in 2009 and the 3SPN.2 model [144] in 2013 as the second and third generations of the previous version. Significant improvements have been adapted to the latest version such that it captures structural and thermal properties more accurately and consistently with experimental data [149–152]. Besides being predictive model for DNA hybridisation, it also shows the capability to investigate DNA-protein interactions, which is a focus in the field of biophysics.

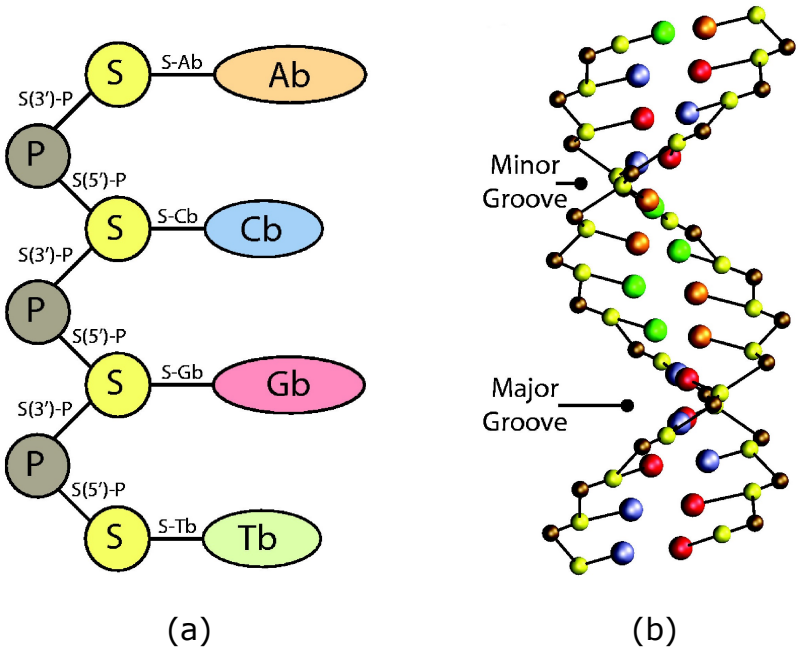

Fig. 1.11 Schematics of 3SPN model. **(a)** Depiction of CG interaction sites for nucleotides. **(b)** 3D representation of 13 bps dsDNA. Image adapted from Ref. [130]. © 2007 AIP Publishing.

Another well-known example in the same coarse-graining division is the oxDNA model (named after Oxford, where it was originated), which was introduced by Thomas Ouldridge and co-workers in 2010 [153]. After nearly a decade's development, the oxDNA model is now seen as the most successful CG model in DNA nanotechnology [154–156]. The original oxDNA model represented each nucleotide with one interaction site for the backbone, three for the base, and an additional normal vector indicating the plane of the base (Fig. 1.10(b)); however, it should be noted that all the bases are identical, i.e. sequence specificity was not yet considered. This model captured the essential thermodynamics and structural properties of short DNA strands [157], and successfully reproduced the free-energy landscape of DNA nanotweezers [153] and the topology of DNA kissing complexes [158]. Subsequently, a sequence-dependent parameterisation was introduced in a more refined version , called oxDNA1.5 [154], which correctly reproduced the formation of major and minor grooves. The latest version is called oxDNA2 [155]. These improvements substantially extend the capability and adaptability of oxDNA, opening up a variety of new applications for the model [127, 159–164].

1.5 Outline of the thesis

The work presented in this thesis focuses on designing and understanding DNA scaffolds for constructing functional hydrogels.

In **Chapter 2**, I report the work I carried out at the beginning of my PhD studies. It concerns the fabrication and characterisation methods of dendrimer-like DNA complexes self-assembled from Y-shaped DNA-nanostars. The design of the Y-shaped structures was originally inspired by similar work done by Dan Luo [165], but later modified and adapted to our own use. I successfully constructed Y-shaped DNA building blocks and dendrimer-like DNA complexes in experiments, and demonstrated

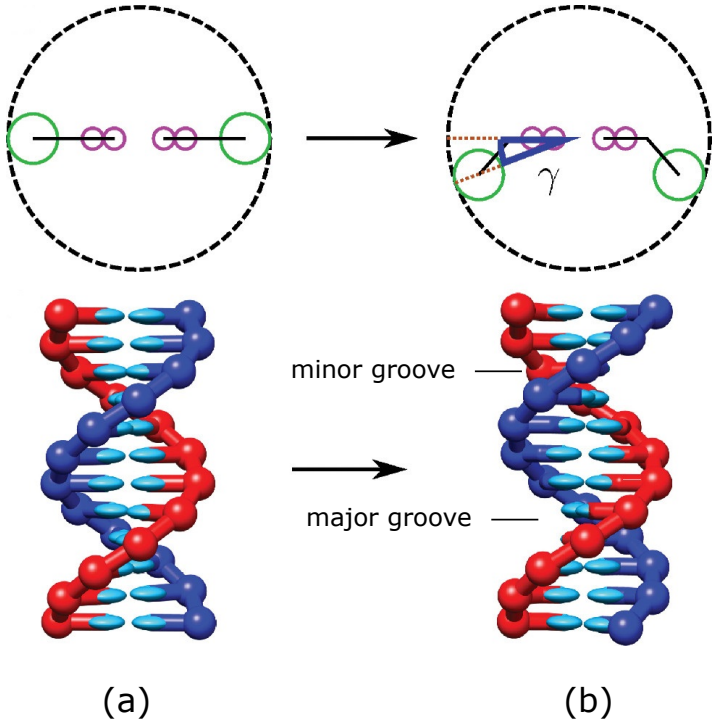

Fig. 1.12 Schematics comparing **(a)** the original oxDNA model with equal groove widths with the **(b)** oxDNA2 that can differentiated major and minor grooves. The dash circle sketches the transverse section of dsDNA, and the solid circles inside represent the interaction sites for backbones and bases. Image adapted from [155].

the high yield of their formation, which assures the design principle in return. The whole work presented in this chapter is the basis of my subsequent projects in exploring DNA hydrogels.

I have dedicated the largest fraction of my PhD time to explore the microrheology on DNA hydrogels, which is presented in **Chapter 3**. Here we performed microrheology measurements using diffusing-wave spectroscopy (DWS) to investigate the viscoelastic behavior of a hydrogel made of Y-shaped DNA nanostars over a wide range of frequencies and temperatures. The results show a clear liquid-to-equilibrium-gel transition as the temperature cycles up and down across the melting-temperature region for which the Y-shape DNA bind to each other. This transition can be easily shifted in temperature by changing the DNA-bond length between the Y-shapes. Employing also bulk rheology,

we further demonstrate that by reducing the flexibility between the Y-shaped DNA bonds we can go from a semi-flexible transient network to a more energy-driven hydrogel with higher elasticity while keeping the microstructure the same. This level of control in mechanical properties will facilitate the design of more sensitive molecular sensing tools and controlled release systems.

In **Chapter 4**, I introduce a coarse-grained numerical model that represents a generic DNA hydrogel consisting of Y-shaped building blocks. Each building block comprises three dsDNA arms with ssDNA sticky ends, mimicked by chains of beads and patchy particles, respectively, to allow for an accurate representation of both the basic geometry of the building blocks and the interactions between complementary units. We demonstrate that our coarse-grained model reproduces the correct melting-behaviour between the complementary Y-shapes, and their assembly into a percolation network. Structural analysis of this network reveals three-dimensional features consistent with a uniform distribution of inter-building block dihedral angles. When applying an oscillatory shear strain to the percolation system, we show that the system exhibits a linear elastic response when fully connected. We finally discuss to what extend the system's elastic modulus may be controlled by simple changes to the building block complementarity. Our model offers a computationally tractable approach to predict the structural and mechanical properties of DNA hydrogels made of different types of building blocks.

Chapter 5 gives a thorough insight of structural and angular properties of Y-shaped DNA foldings by employing oxDNA simulation model. This work is done in collaboration with Yair Augusto Gutierrez Fosado (University of Edinburgh, the U.K.) and Dr. Oliver Henrich (University of Strathclyde, the U.K.). In particular, we played with the structures of the individual building block by the inert bases, i.e. bases does not hybridise in an individual assembly, in the middle twisting core and the flexible

joint part. The data we acquired in this work can help further developing the hydrogel model described in Chapter 4.

Finally, **Chapter 6** concludes the thesis and presents an outlook for the future work that have been emerged out of my experimental and numerical studies.

Chapter 2

Assembly and characterisation of dendrimer-like DNA complexes

Branched DNA complex structures can lead to the development of functional materials with controlled release and programming self-assembling properties. In this chapter I describe an exploratory study of a hierarchical structure of branched DNA complexes self-assembled by three-armed DNA building blocks, which is also known as 'dendrimer-like DNA' or 'DNA dendrimers'. Basic experimental methods that were used to characterise the structures are introduced, e.g. UV-vis spectroscopy and gel electrophoresis. In particular, the melting curves of three-armed building blocks in various conditions were carefully examined via UV-vis spectroscopy, which provides a deeper understanding of the thermodynamics of DNA hybridisation. The studies conducted in this chapter lay the foundation of my following work of exploring functional DNA hydrogels.

2.1 Introduction

Emerging from the *Holliday Junction* (see Fig. 2.1), which was first proposed by Robin Holliday in 1964 [166], branched DNA structures [167–170] with multiple dsDNA arms emanating from a central point have generated great interest in the field of structural DNA nanotechnology in the past decades. The opening-up of this field dates back to 1982 with a paper published by Nadrian Seeman [171], where he came up with the idea of generating 2D arrays or 3D lattices of nucleic acids by using branched DNA junctions adapted from the Holliday junction. Particularly, care needs to be taken into account in the design of the modified sequences to fulfil prescribed design-conditions for forming more n-armed DNA building-blocks and how they bind to each other. Such design principles directly control the adherence and symmetry of the branches, the 'rigidity' of the central point of the DNA buildingblock, and the minimisation of secondary structures. In addition, the bond between DNA-building blocks can be achieved with great specificity, using either sticky-ended ligation techniques [171, 56] or simply DNA hybridisation [63, 81]. Nowadays, those branched DNA junctions can be easily tailored to construct targeting DNA architectures on larger scales other than the initially proposed periodic arrays or networks.

Dendrimers are tree-like, branched macromolecules with highly repetitive and symmetric geometrical properties, which can be synthesised in a stepwise fashion from a central core [172, 173]. In 2004, Dan Luo's group reported a dendritic structure constructed through ligation of branched DNA molecules with three double-stranded arms and a 4-base sticky end on each arm [165] (Fig. 2.2). In their paper two approaches for synthesising three-armed DNA (which they call 'Y-shaped DNA') were described: in the *a) step-wise synthesis* two partially complementary ssDNAs were hybridised first, and then a third, partially complementary ssDNA oligomer was added; in the *b) all-in-one synthesis*, all the three ssDNAs were mixed at once and hybridised together

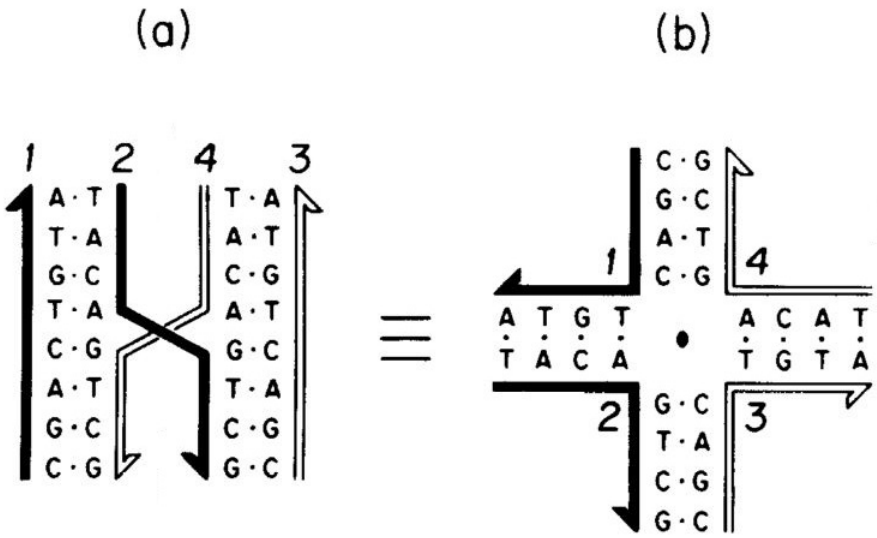

Fig. 2.1 **(a)** Schematics of a Holliday Junction originally proposed [166], and **(b)** its identical representation. The black and white lines with half-arrows indicate the backbones of a single nucleotide, where the arrows show the direction in which the 5' to 3' ends point towards. The image is adapted from [171]. © 1982 Elsevier.

by cooling their solution slowely to below the systems T_m. They also demonstrated that there was no difference between these two approaches in terms of the yield of Y-shaped DNA formation - which was close to 100%. The repetitive structures (called 'generations') were grown via a sticky-end-directed ligation process, so that the dendritic structure was assembled and subsequently connected covalently. The yield of the target structure was $> 80\%$ after four generations. These dendrimer-like DNA molecules could be studied for multiplexed detection and drug delivery as they exhibit the capability to carry and release multiple molecular cargoes simultaneously [174–176]. Unlike Dan Luo's study of using ligation techniques to assemble different generations, I designed the dendrimer-like DNA complexes, whose subsequent generations were connected via DNA hybridisation of the sticky ends (Fig. 2.3(a)). There are two main advantages of this technique: *i.* driven by DNA thermodynamics, the structure is self-assembled without adding extra chemicals (*e.g.* DNA ligase), which provides a more robust reaction environment; *ii.* owing to the reversibility of hydrogen bonds between the sticky ends,

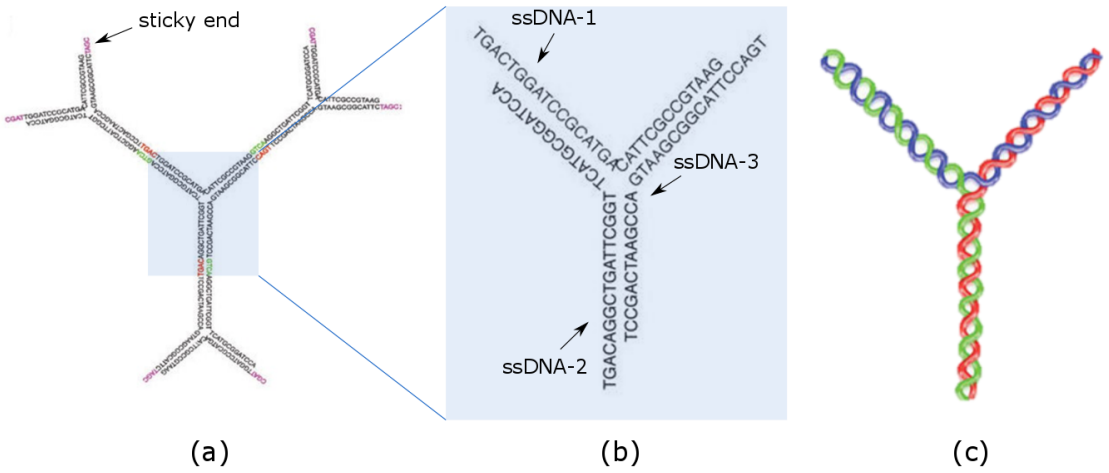

Fig. 2.2 Schematics of the 2nd generation dendrimer-like DNA and its Y-shaped building blocks. **(a)** A dendrimer-like DNA structure with the core and its first generation. Coloured sequences indicate the sticky ends. **(b)** Zoom of the central Y-shaped DNA assembled by three partially complimentary ssDNAs. **(c)** An illustration of Y-shaped building-block formation. Images were redrawn from [165].

the resulting structure can dissociate and reassociate, which broadens the function of these materials. In my study, the sequences of the building blocks and the sticky ends were carefully designed to achieve a melting-temperature ladder between the different generations in a cascade, resulting in a temperature-dependent hierarchical structure (Fig. 2.3(b)-(c)). Here I used the *all-in-one* approach to construct the three-armed DNA building blocks (see Fig. 2.3(b)). The melting curves of the building blocks with and without sticky ends in various solution conditions were characterised using UV-vis spectroscopy. The partial and full formations of three-armed DNA and the dendrimers were tested by gel electrophoresis techniques. Finally, I measured the size of the dendrimer-like DNA structure by performing dynamic light scattering (DLS) measurements, demonstrating a growing-up cluster size along with the growth of the generations of the molecule.

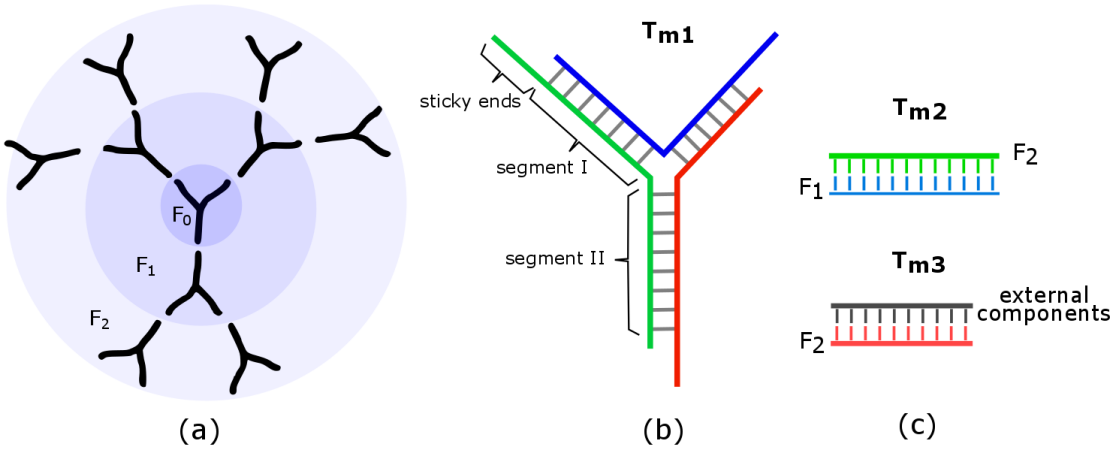

Fig. 2.3 Schematics of dendrimer-like DNA and the three-armed building blocks in my study. **(a)** A dendrimer-like DNA structure with three generations, namely F_0, F_1 and F_2. **(b)** An illustration of a Y-shaped DNA. Each ssDNA consists of three functional pieces: a sticky end, segment I and segment II. The melting temperature of the Y-shaped assembly is denoted as T_{m1}. **(c)** Illustration of the sticky ends connecting consecutive generations, defined by their melting temperatures for the inner (T_{m2}) and the outer terminals (T_{m2}).

2.2 Materials and Methods

2.2.1 Sequence design

Three typical melting temperatures were considered in the design of the dendrimer-like DNA structure: T_{m1}, for the assembly of the three-armed DNA building blocks; T_{m2}, for connecting individual three-armed DNAs into an overall structure; T_{m3}, for detecting the external components that are attached with ssDNAs in the future (Fig. 2.3(b)-(c)). The *melting-temperature ladder* means the values of them should meet the condition that $T_{m1} > T_{m2} > T_{m3}$ at reasonable intervals. For example, at a the sodium concentration of 50 mM, the melting transition of a dsDNA below 100 bps is roughly 5∼10 °C, so I aimed at the interval of around 10∼15 °C to avoid a temperature-response overlap between neighbouring assembling levels.

All sequences were first randomly generated using online tools provided by specialised websites[1], and then selected following the flow chart shown in Fig. 2.4. This involves the melting temperatures, secondary structures and self-dimers that can be analysed via OligoAnalyzer 3.1[2]. Detailed explanations of theoretical or empirical rules for designing DNA sequences can be found in Ref. [167, 168, 177].

Table 2.1 lists the final sequences designed for constructing the dendrimer-like DNA complexes. The F_0, F_1 and F_2 form the three-armed DNA nanostar in the core, and the consecutive 1^{st} and 2^{nd} generation respectively (see Fig. 2.3(a)); the subscripts a, b and c denote the single strands that assemble into the individual three-armed Y-shapes. Complementary oligo strands in one Y-shaped DNA are marked in the same colour (red, blue or black); the length of each double-stranded arm is 15 bp, which is much shorter than the persistence length of dsDNA (*i.e.* 150 bp), so they appear rigid. The sticky ends for linking the building blocks within a denderimer are 12 bp long, with the calculated melting temperature T_{m2} = 45∼50 °C; however, the sequences are distinct so that only F_0-F_1 and F_1-F_2 linkages are possible. The melting temperature of the external sticky ends, T_{m3} is about 30∼35 °C and has a length of 10 bp. All strands are also designed to avoid any conflicting binding with each other. It should be noted that the melting temperature values given here were estimated for the solution condition that [NaCl] = 50 mM and [DNA] = 0.25 µM; they can deviate when the ionic strength and DNA concentration are changed.

The melting temperature of the three-armed assemblies (T_{m1}) cannot be simply calculated in the same way as dsDNA, as the topological structures and sticky-end overhangs can play a role in it. Therefore the melting properties of such formations need to be examined experimentally, which shall be described in a later section.

[1] e.g. http://www.faculty.ucr.edu/~mmaduro/random.htm
[2] One possible online tool is available at http://www.idtdna.com/calc/analyzer.

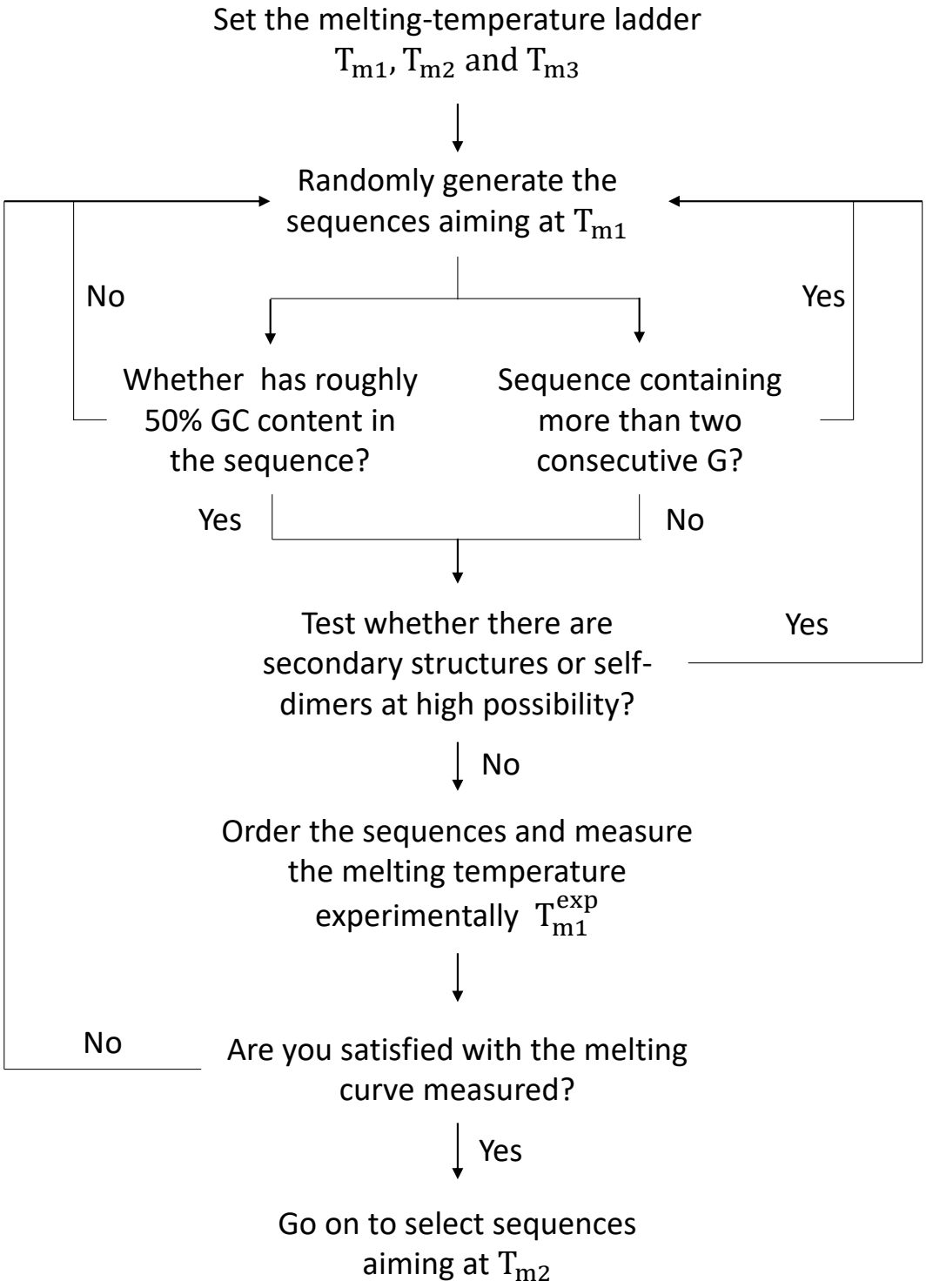

Fig. 2.4 Flow chat of designing the main-body of the Y-shaped DNA.

Table 2.1 Oligonucleotides sequences for forming dendrimer-like DNA complexes

Label		Sticky ends	Rigid part	
			Segment I	Segment II
F_0	F_{0a}	5'-TGTCACTCACAG	TGGATCCGCATGATC	CATTCGCCGTAAGTA -3'
	F_{0b}		TACTTACGGCGAATG	ACACCGAATCAGCCT-3'
	F_{0c}		AGGCTGATTCGGTGT	GATCATGCGGATCCA-3'
F_1	F_{1a}	5'-CTGTGAGTGACA	TGGATCCGCATGATC	CATTCGCCGTAAGTA-3'
	F_{1b}	5'-GTATGACGACCA	TACTTACGGCGAATG	ACACCGAATCAGCCT-3'
	F_{1c}		AGGCTGATTCGGTGT	GATCATGCGGATCCA-3'
F_2	F_{2a}	5'-TGGTCGTCATAC	TGGATCCGCATGATC	CATTCGCCGTAAGTA -3'
	F_{2b}	5'-ATTGGATTGG	TACTTACGGCGAATG	ACACCGAATCAGCCT-3'
	F_{2c}		AGGCTGATTCGGTGT	GATCATGCGGATCCA-3'

2.2.2 Synthesis of dendrimber-like DNA

Oligonucleotides were purchased from Integrated DNA Technologies, Inc. in a dry state and used without further purification. The dry material was suspended in 1 × TE buffer (10 mM Tris, pH = 8.0, 1 mM EDTA) creating DNA stock solutions with a concentration of around 20 µM. These were then stored in a freezer at −20 °C until further use. The DNA concentration in the stock solutions was re-measured using a NanoDrop™ 2000 Spectrophotometers (Thermo Fisher Scientific Inc) before use. Technical details of the DNA quantification can be found in Ref. [178].

To assemble the three-armed building blocks, three corresponding non-purified solutions of corresponding single DNA strands were mixed to a final concentration of 5 µM, where each strand solution in 1 × TE buffer was supplemented with 150 mM NaCl to assist the DNA hybridisation process. The reactions are shown in Eq. 2.1.

$$\begin{aligned} F_{0a} + F_{0b} + F_{0c} &\rightleftharpoons F_0 \\ F_{1a} + F_{1b} + F_{1c} &\rightleftharpoons F_1 \\ F_{2a} + F_{2b} + F_{2c} &\rightleftharpoons F_2 \end{aligned} \tag{2.1}$$

The oligo mixtures were then annealed in a PCR thermo-cycler (Mastercycler™ personal) following a temperature-ramp protocol described in the text below. The mixtures containing the three partially complementary ssDNAs were first denatured at 94 °C for 5 minutes, and incubated at 80 °C for 2 minutes. After a fast cooling to 72 °C, the temperature was then further decrease at a rate of −1 °C/s until it reached 42 °C. Then it was reheated rapidly to 72 °C, followed by a repeated slow-cooling process. After 5 repetitions, the samples were cooled down to 20 °C and retained there for 10 minutes. Finally the samples were incubated at 4 °C for storage.

Likewise, dendrimer-like DNA complexes were assembled by the corresponding three-armed building blocks at an equal-number ratio to maximize the yield. Reactions of the assembly are described by Eq. 2.2 below,

$$\begin{aligned} F_0 + 3F_1 &\rightleftharpoons G_1 \\ F_0 + 3F_1 + 6F_2 &\rightleftharpoons G_2 \end{aligned} \tag{2.2}$$

where G_1 and G_2 denote the 1^{st} and 2^{nd} generations of the denderimer respectively.

To avoid denaturing the pre-formed building blocks, the mixtures were first incubated at 53 °C for 10 minutes. Then the solutions were slowly cooled down to 33 °C at the rate of −1 °C/s with 30 s incubation per degree. The resulting solutions were finally stored at 4 °C for later use.

2.2.3 Characterisations: UV-vis spectroscopy, gel electrophoresis, and DLS measurements

UV-vis spectroscopy

The DNA melting curves were characterised using a Cary 300 UV-vis Spectrophotometer (from Agilent Technologies) equipped with a temperature-controlling Peltier element.

A quartz cuvette with a path length of 1 cm was used to load the sample solution. The cuvette was inserted into the cell holder of the instrument. Meanwhile, a blank cuvette with the background solvent of the DNA sample was also used in oder to subtract the background absorption during the measurement. The 260 nm absorbance of the DNA sample was measured as a function of temperature, reflecting the so-called melting curves. The results are shown in section 2.3.

To prepare the sample for the melting curve measurement, one should first estimate the final concentration of the measuring sample. Assuming that all ssDNAs are equal-molar in the solution, the estimated concentration value per strand can be calculated by Eq. 2.3,

$$[\text{DNA}] = \frac{A}{\sum \epsilon_i \cdot l}, \tag{2.3}$$

where A is the absorbance, ϵ_i is the molar extinction coefficient for ssDNA i at the wavelength of 260 nm, and $l = 1$ cm is the path length through the cuvette. The value of absorbance normaly ranges from 0 to 1, and was empirically selected here as 0.8. For fundamental information on light absorbance see Ref. [179].

Gel electrophoresis

The formation of DNA complexes were characterised by employing the gel electrophoresis technique [180]. This technique is widely used for separating and analysing charged DNA, RNA and proteins by detecting the migration distance of those samples driven in an applied electric field. The migration happens in an agarose or polyacrymide gel, with a tunable pore-size that was controlled by the polymer concentration. The migration distance gives information about the sample such as molecular weight, since the frictional resistance increases as the molecule gets larger.

As mentioned before, the gel electrophoresis measurement can be applied either in an agarose gel or a polyacrylamide gel. The main differences between these two

are the way of making the gels (as the former is a physical gel while the latter is a chemical one) and the pore-size range of the resulting gels (agarose normally has a larger pore-size that the polyacrylamide one). In my experiments, measurements using both gels have been performed for different sizes of my samples.

Agarose gel electrophoresis was conducted in a horizontal setup as shown in Fig. 2.5. The gel was placed in an box filled with running buffer, which provides the conductive and migrating environment. A parallel electric field was applied to the box from top to bottom, while the migration direction of the DNA sample is the other way around due to the negative charges along the phosphate-sugar backbones. A comb was inserted before the formation of the gel matrix to shape the loading wells of the sample. The whole apparatus was incubated in an ice bath to enhance the measurement performance.

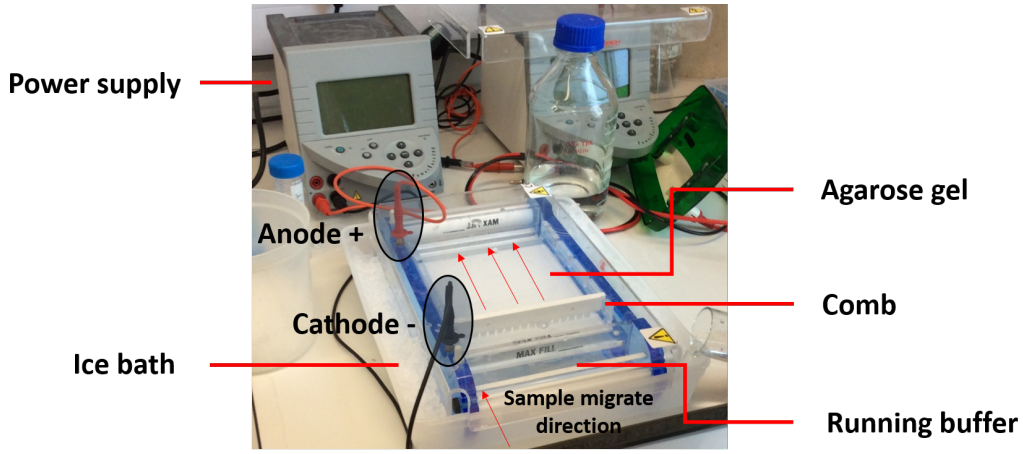

Fig. 2.5 An agarose gel electrophoresis setup.

To make an agarose gel, a given amount (depending on the required pore size) of powered agarose (purchased from Sigma-Aldrich®) was added to 0.5 × TBE buffer (44.5 mM Tris-borate and 1 mM EDTA, pH = 8.3, purchased from Sigma-Aldrich®), and then put into a heating and cooling procedure as shown in Fig. 2.6. In my experiments, the optimum gel concentration was $1.8 \sim 2$ w/v%. The electrophoresis

was normally conducted at an applied voltage ranging between 60 V and 100 V for about 2 h, depending on the sample properties and the expecting resolution.

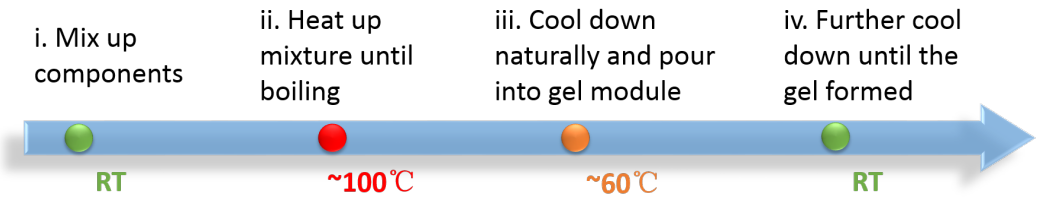

Fig. 2.6 Flow chart of making an agarose gel. RT stands for Room Temperature.

Polyacrylamide gel electrophoresis (PAGE) was performed in a vertical setup shown in Fig. 2.7(a) (Mini-PROTEAN ® Tetra Cell, Bio-Rad Laboratories, Inc.). The working principle of this apparatus is the same as that of an agarose setup, except that the electric field is applied vertically (see Fig. 2.7(b)). A 10 w/v% polyacrylamide gel supplemented with 11 mM $MgCl_2$ (purchased from Sigma-Aldrich®) was made by the polymerisation of acrylamide (purchased from Sigma-Aldrich®) following the protocol in Appendix A. After loading the sample, an electric field of 100 V was applied for $60 \sim 85$ minutes at RT.

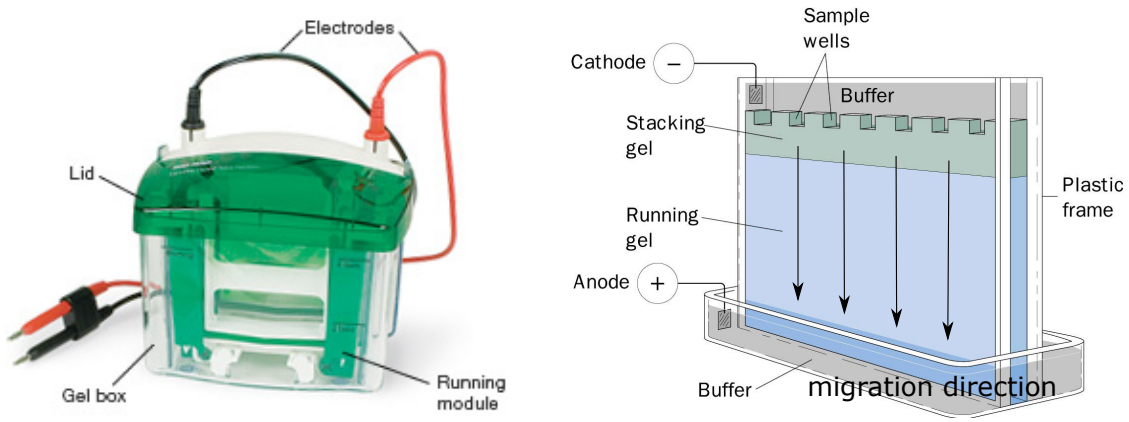

Fig. 2.7 Illustration of a PAGE setup. **(a)** Snapshot of the apparatus. The image was taken from [181]. **(b)** Schematic working principle. The image was taken from [182].

After running the electrophoresis, both agarose and polyacrylamide gels were stained by a nucleic acid gel stain (GelRed®, produced by Biotium) for about 20 minutes, and visualised under a UV illuminator (GelDoc-It®, produced by UVP, LLC).

Dynamic light scattering (DLS) measurements

The dynamic light scatting (DLS) technique [183, 184] integrated into a Zetasizer Nano ZS (Malvern Panalytical Ltd.) was used to measure the size distribution of the DNA complexes. It is a spectroscopy method based on analysing the scattering pattern of a suspended sample (colloids, macromolecules, droplets, etc.) emanating from incident, monochromatic laser light. The scattered light is measured via a fast photon detector at a fixed scattering angle θ with respect to the incident laser light. The time-fluctuating intensity of the scattered light $I_s(q,t)$ is then correlated and outputted as an intensity-autocorrelation function g_2 written as:

$$g_2(q,\tau) = \frac{\langle I_s(q,t) I_s(q,t+\tau)\rangle}{\langle |I_s(q,t)|^2\rangle}, \tag{2.4}$$

where

$$q = \frac{4\pi n_0}{\lambda}\sin(\frac{\theta}{2}) \tag{2.5}$$

is the wave factor, with λ being the incident laser wavelength and $\mathrm{n_0}$ the refractive index of the solvent. τ in Eq. 2.4 stands for the time lag. As one should expect, g_2 shows a decay in time, and it is actually the part that holds the information about the diffusivity of the suspended particles [183].

In sufficiently dilute samples, in which only single scattering event take place, the decay of g_2 can be fitted with an exponential function:

$$g_2(q,\tau) = 1 + \exp(-q^2 D\tau). \tag{2.6}$$

Here D is the diffusion coefficient of the scattering object. It can be related to the particle size by applying Stokes-Einstein equation shown below

$$D = \frac{k_B T}{6\pi\eta R}, \tag{2.7}$$

where k_B is Boltzmann constant, T is the temperature in Kelvin, η is the viscosity of the solvent and R is the radius of the spherical scattering particles. Note that the measured radius is often referred to as the hydrodynamic radius R_h (subscript h stands for 'hydrodynamic'), which may appear a little larger than the 'dry' size of the particles because it drags a fluid layer around itself.

2.3 Results and discussions

2.3.1 Ionic effect on DNA melting/hybridisation

As briefly mentioned before, the phosphate-sugar backbone of DNA is negatively charged, which provides electrostatic repulsion between ss- or ds-DNAs, and may prevent complementary ssDNAs from hybridisation. Therefore additional salt (normally NaCl, but in some extreme cases $MgCl_2$, e.g. DNA origami) is used to screen the negative charges on the backbones, which would eventually facilitate the DNA hybridisation process.

To start with, I tested the salt effect on the hybridisation of a linear duplex system that had been used in our lab by adding an increasing concentration of NaCl in the sample solutions; results are shown in Fig. 2.8. The ssDNAs used here are called A_{short} and C_{active}, with the sequences as follows: A_{short}:5'-TTTTT GAGGAGGAAA GAGA-GAAAGA AGGAGAGGAG AAGGGAGAAA AGAGAGAGGG AAAGAGGGAA TTTTT CCGGCC-3'; C_{active}: 5'-TTCCCTCTTT CCCTCTCTCT TTTCTCCCTT

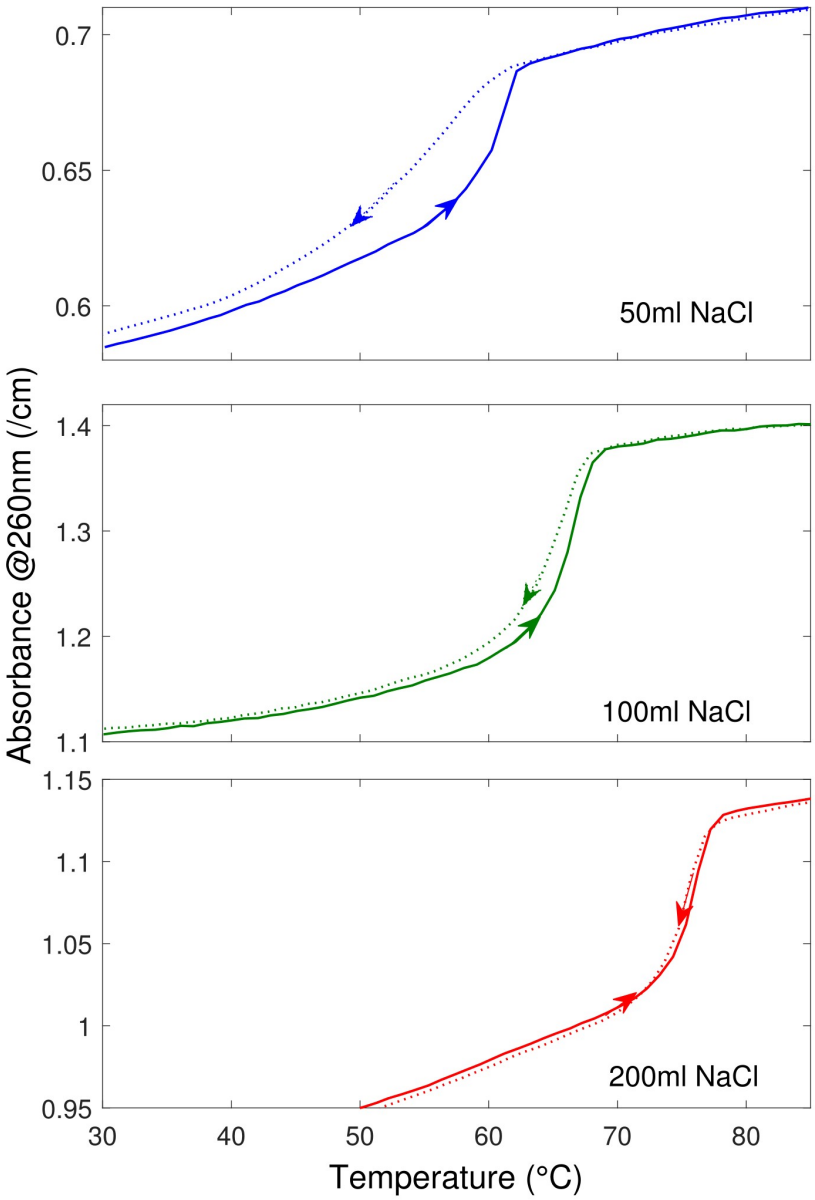

Fig. 2.8 Experimentally acquired melting curves of duplex DNA hybridised by ssDNA named A_{short} and C_{active}. In all cases we use TE buffer. From top to bottom, the NaCl concentrations used were 50 mM, 100 mM and 200 mM.

CTCCTCTCCT TCTTTCTCTC TTTCCTCCTC-3'. The sequences coloured in emerald are complementary to each other (60 bps). The measurements were conducted in the UV-vis spectroscopy (Section 2.2) between 30 and 85 °C with a heating ramp,

held there for 20 minutes and then cooled down again. The temperature was changed at 0.5 °C/minute, and the data were collected in 1 °C steps.

From Fig. 2.8 we see a clear shift towards high melting temperatures as the NaCl concentration increases (from ~ 60 °C $\rightarrow$ ~ 67 °C $\rightarrow$ ~ 75 °C). Besides, the melting transition is sharpened and narrowed down from roughly 10 °C to within 5 °C. However, for an individual melting curve, we observed a small gap in the melting transition between cooling and heating processes, indicating a non-equilibrium state of the sample. This gap is shown to decrease when the cooling/heating speed further slows down. Also, the hysteresis phenomenon is less serious for high-salt-concentration sample, which suggest the relaxation time of equilibrium process may relate to the ionic strength.

Accordingly, we tested the NaCl effect on three-armed DNA structures. Results of melting curves are shown in Fig. 2.9, which shows the same trend as the duplex DNA system. This further enhances the discussions above. The DNA sequences used in this model are:

1. 5'- TGT CAC TCA CAG TGG ATC CGC ATG ATC CAT TCG CCG TAA GTA - 3';
2. 5'- TGT CAC TCA CAG TAC TTA CGG CGA ATG ACA CCG AAT CAG CCT - 3';
3. 5'- TGT CAC TCA CAG AGG CTG ATT CGG TGT GAT CAT GCG GAT CCA - 3',

with colour-matched sequences complementary to each other, except for the black sticky ends that are inert. Here the heating/cooling rate was decreased to 0.2 °C/minute; therefore little hysteresis is seen as expected. Additional contributions to possible

hysteresis can be base-errors in the sequences and a mismatch in the number densities in the individual sequences.

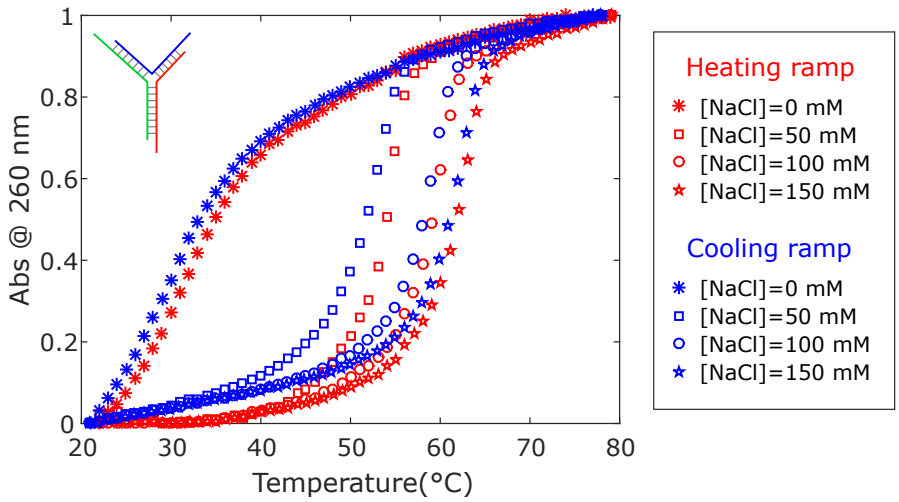

Fig. 2.9 Rescaled absorbance profiles for a sample with Y-shaped architecture. In all cases we used a TE buffer, and added NaCl at various concentrations.

2.3.2 Inert tails effect on DNA melting/hybridisation

In this section I shall present the results of a three-armed DNA structure (Ra-DNA) without inert tails, i.e. all the base pairs are fully bonded. Sequences of Ra-DNA are the same as those of the Y-shaped structure listed in the previous section, but without the black-coloured sticky ends. Melting-curve results and analysis are shown in Fig. 2.10. Four ramps were taken at a rate of 0.2 °C/minute to check the reproducibility of the measurements as well as the hysteresis.

Fig. 2.10 (b) presents a way of measuring the melting temperature, which is called the 'baseline method'. Here two linear lines $y_1(x)$ and $y_2(x)$ are fitted to the high- and low-temperature plateaus, where x stands for the temperature. Then an intermediate linear line $y_3(x)$ is drawn, whose slope and intercept are averaged from those of $y_1(x)$

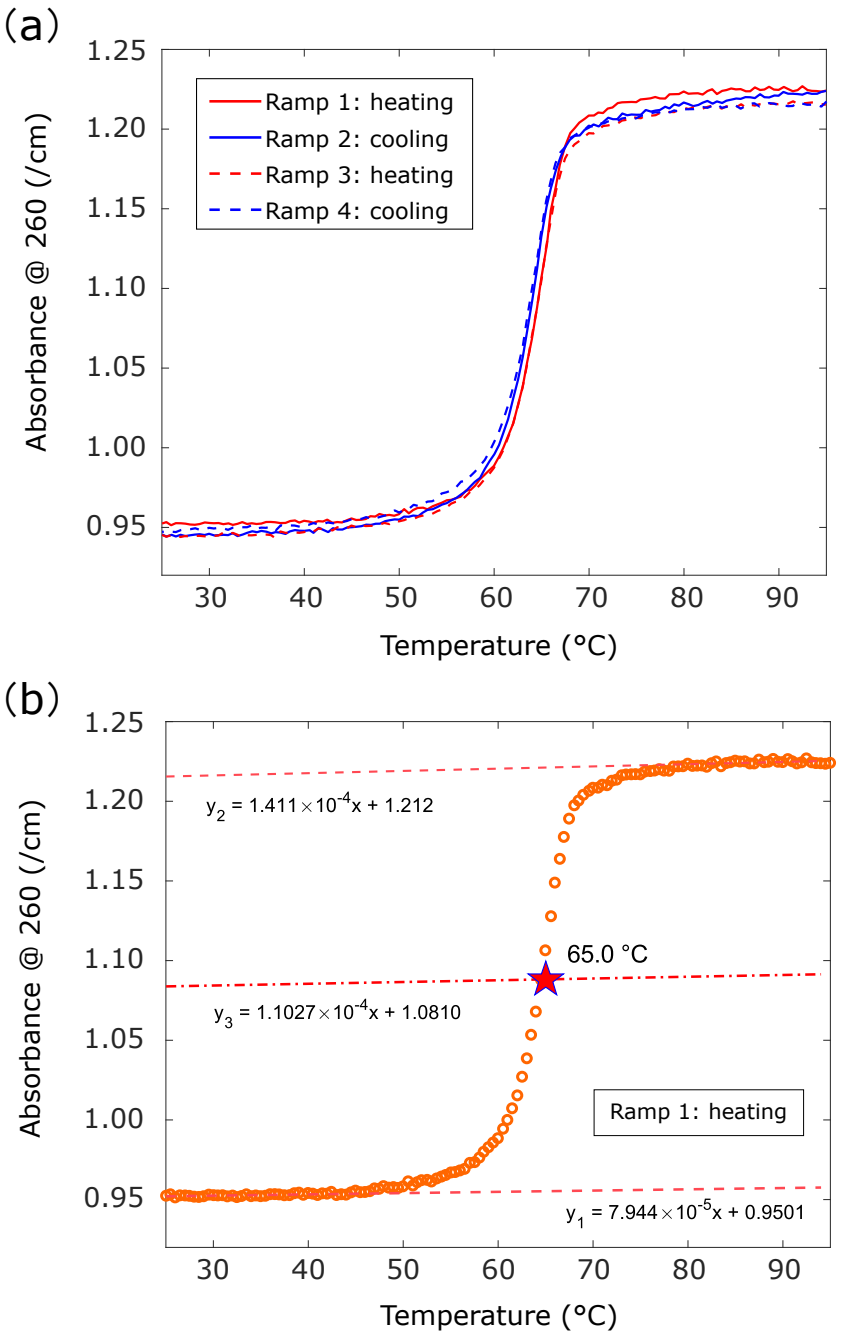

Fig. 2.10 **(a)** Absorbance profiles for R_a-DNA. In this case I used TE buffer complemented with 150 mM NaCl. **(b)** An illustration of the baseline method for analysing T_m.

and $y_2(x)$. The crossover between y_3 and the measured melting curve is the T_m. In the presented example, the melting temperature T_m is 65 °C.

From Fig. 2.10, we observe that: (i) the melting temperature of Ra-DNA is about 7 °C higher than that of its variation with inert sticky ends (Section 2.3.1) at the same ionic conditions, and (ii) the melting transition is also narrower; (iii) the high- and low-temperature slopes are also flatter. In addition, the perfect symmetric shape of the melting curves demonstrated the success of the three-armed formation. This is confirmed by gel electrophoresis results in Appendix A. In conclusion, Ra-DNA has been demonstrated to be a robust three-armed structure whose T_m satisfies our requirement for T_{m1}, thus the building-block sequences of dendrimer-like DNA structures are modified based on it.

2.3.3 Characterisations of three-armed DNA building blocks

The melting curves of the designed three-armed DNA building blocks F_0, F_1 and F_2 are presented in Fig. 2.11. The sequences have been given in Section 2.2.1. Measurements were taken in 150 mM NaCl concentration as the temperature went up from 35 to 85 °C at 0.2 °C/minute. We can calculate the melting temperatures of building block structures from each generation using the baseline method, and get them to be approximately 62 °C each. Not surprisingly, they are slightly lower than the T_m of the pure branched structure without sticky ends.

The PAGE result evaluating the effectiveness of these building-block formation is shown in Fig. 2.12. Samples loaded in lane 1-4 are as follows: F_0, F_{0a} + F_{0b}, F_{0b} + F_{0c}, and F_{0a} + F_{0c}, with all the ssDNAs mixed at equal amounts. The successful hybridisation between the complementary segments of F_{0a}, F_{0b} and F_{0c} is demonstrated by the positions of DNA bands, and the satisfactory yield of the building block formation is supported by the sharpness and strength of the dark bands in the gel.

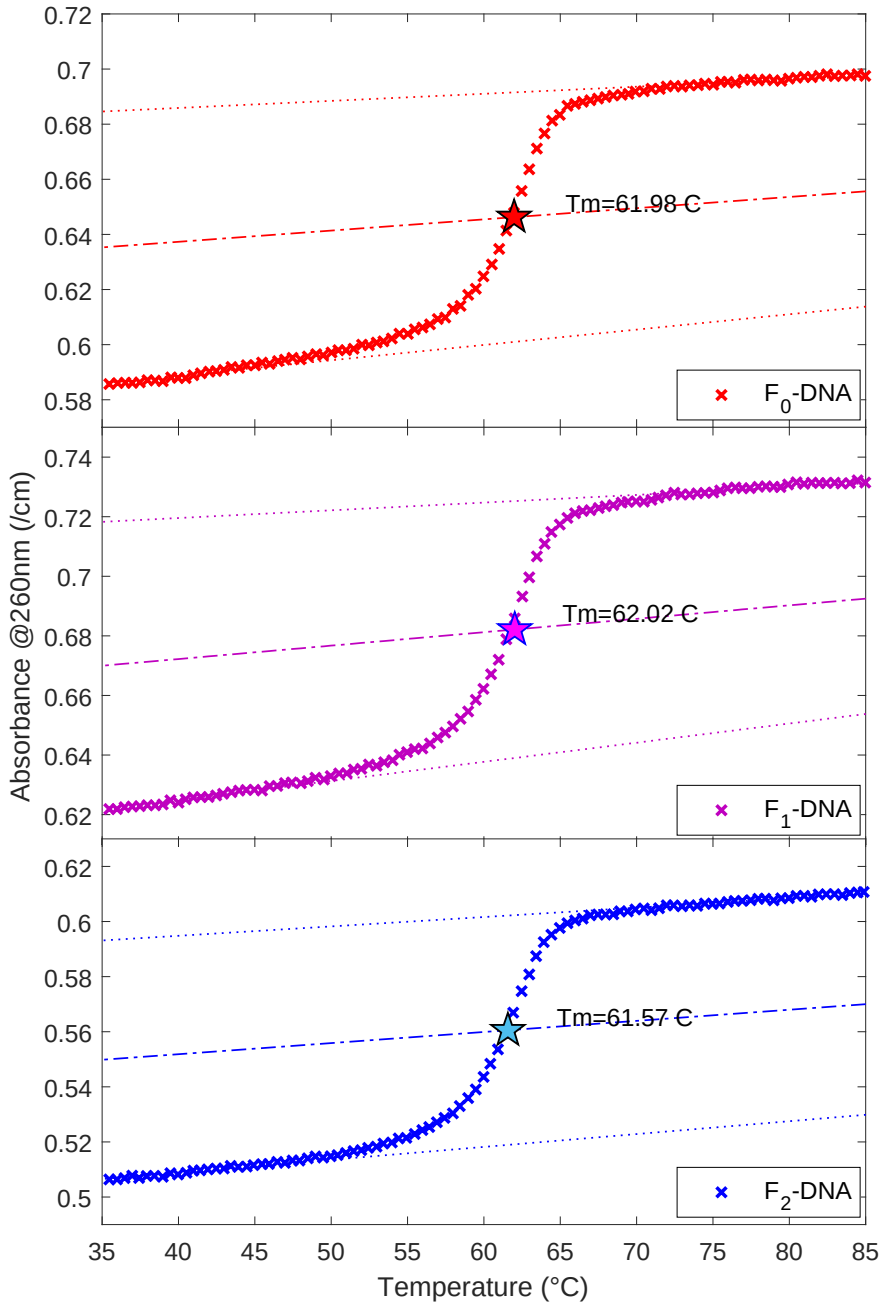

Fig. 2.11 Melting curves of three-armed DNA structures F_0, F_1 and F_2. The star-symbols represent the extracted melting temperatures.

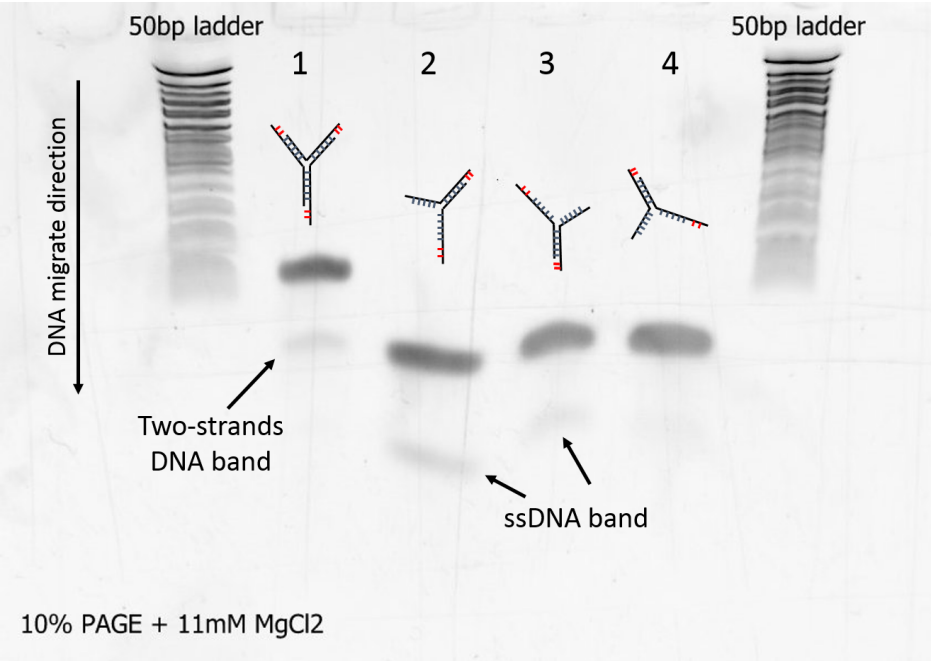

Fig. 2.12 PAGE results of partial and full formations of F_0-DNA. The DNA ladder (50 bp DNA ladder, purchased from New England BioLab ®) was used as reference to mark DNA migration distances as function of their molecular weight.

2.3.4 Characterisations of dendrimer-like DNA complexes

Agarose-gel electrophoresis results shown in Fig. 2.13 demonstrate the formation of the dendrimer structure. Tab. 2.2 shows the samples loaded in each lane with the relative amount of the components per well, and schematics of the corresponding structures are shown in Fig. 2.13(a). In Fig. 2.13(b)-(c), Lane 1-3 show sharp single bands at the same migrating distance, confirming the formation of building blocks and their high yield. Each lane in number 4 to 6 exhibits a main band at a shorter migrating distance, and a secondary band at the equivalent position as that in lane 1-3. The main band indicates the product we loaded, while the secondary band can be either the excess of the three-armed formation or the broken-down building blocks during migration.

Table 2.2 Samples loaded into each lane in Fig. 2.13.

Lane 1	Lane 2	Lane 3	Lane 4	Lane 5	Lane 6
F_0	F_1	F_2	$F_1 + 2F_2$	$F_0 + 3F_1$	$F_0 + 3F_1 + 6F_2$

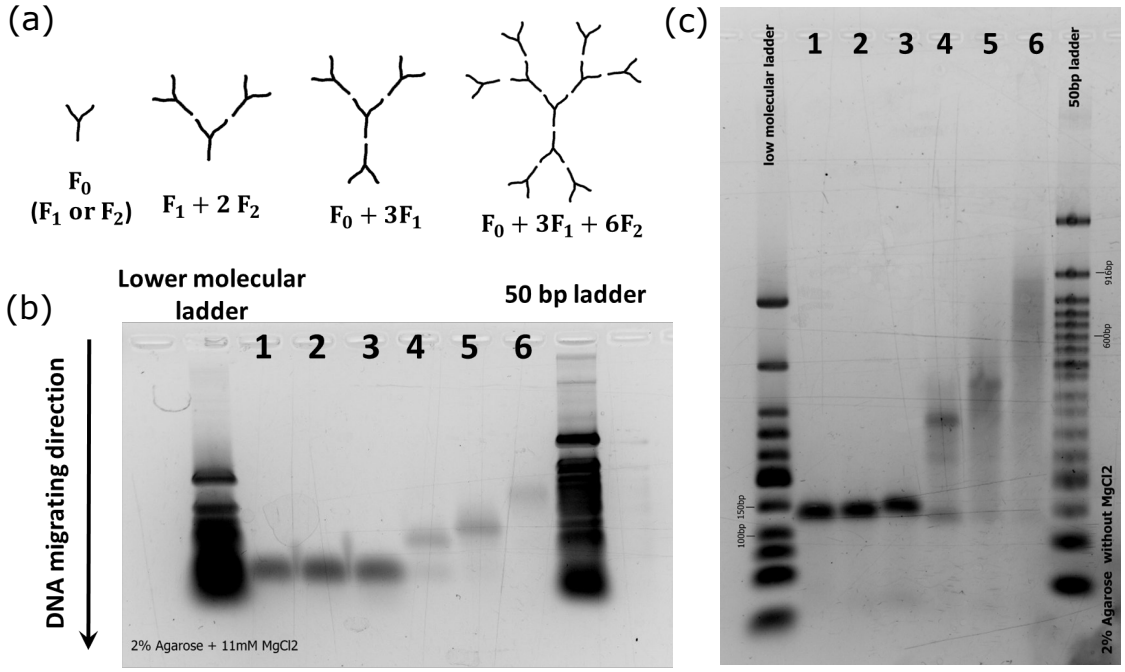

Fig. 2.13 **(a)** Schematic of products loaded in an agarose gel as specified in Tab. 2.2. **(b)**-**(c)** Agarose gel electrophoresis results evaluating the formation of dendrimer-like DNA complexes **(b)** with 11 mM $MgCl_2$ and **(c)** without additional $MgCl_2$, in 2 % gel. Lower molecular weight DNA Ladder and 50 bp DNA Ladder (both purchased from New England BioLab ®) were used as reference for the positions of the DNA bands.

We also conducted DLS measurement to characterise the size of dendrimer-like DNA complexes and got the averaged diameter of the core, 1st and 2nd are 3.7 nm, 22.6 nm and 30.1 nm correspondingly, which fits our expectation.

2.4 Conclusions

In this chapter, I have reported an approach to assemble dendrimer-like DNA complexes purely based on DNA hybridisation, and demonstrated the success of their formations

up to three generations. The structures synthesised here were assembled by three-armed DNA, but the building blocks are not limited to only three arms (e.g. 4-, 5- and n-arms). Neither should the structures be limited to just three generations. But for growing larger dendrimer structures, purification processes might be introduced to avoid the fragmented structures of the dendrimer in between. Also, the linkage between neighbouring generations may need to be strengthened to minimize the chance of dendrimers breaking down into the fragments. Advantages of these structures are the highly precise recognition and thermally reversible property due to the DNA sequences, and the multiple carriage capability owing to the dendrimer terminals, which could enable the future design of functional materials with high sensitivity, specificity and capacity.

The characterisation tools used here are widely applied in the topic of DNA nanotechnology, and will be further employed in my other experimental work presented in the next chapters in this thesis.

Chapter 3

Microrheology of DNA hydrogels

A key objective in DNA-based material science is understanding and precisely controlling the mechanical properties of DNA hydrogels. Employing diffusing-wave spectroscopy (DWS) microrheology to investigate the mechanical properties of DNA hydrogels at the micro-length scale, we map the viscoelastic response over a broad range of frequencies and temperatures. Results show a clear liquid-to-equilibrium-gel transition as the temperature cycles up and down across the melting-temperature region for which the Y-shaped DNA nanostars bind to each other. Our measurements reveal a crossover between the elastic $G'(\omega)$ and viscous $G''(\omega)$ around the melting temperature T_m of the DNA building blocks, which coincides with the systems percolating transition. This transition can be easily shifted in temperature by changing the DNA-bond length between the Y-shapes. Employing also bulk rheology, we further demonstrate that by reducing the flexibility between the Y-shaped DNA bonds we can go from a semi-flexible transient network to a more energy-driven hydrogel with higher elasticity while keeping the microstructure the same. This level of control in mechanical properties will facilitate the design of more sensitive molecular sensing tools and controlled release systems.

3.1 Introduction

DNA hydrogels are a type of tenuous, semi-flexible polymeric network that consists of precisely designed synthetic nucleotide strands as chemical or physical cross-linkers [56, 68, 185, 20, 63]. These man-made bulk DNA hydrogels have been widely studied as functional materials that can be potentially used for controlled drug delivery, tissue engineering, biosensing and other applications in the fields of nanotechnology and bioengineering mainly becasue of their bio-compatibility and the ability to mix them with other (bio)polymers [186–190]. In particular, the vast combinations of the Watson-Crick pairing provide a unique way to achieve programmable self-assembly of thermally reversible gels with precise functionality [84, 191]. Current studies mostly focus on the fabrication and utilisation of DNA hydrogels, while the fundamental physics of these gels still lacks good understanding [63, 192, 188]. In recent years, a series of computational and experimental studies were carried out on the phase diagram of DNA hydrogels made of 2-, 3- and n-valent nano-stars and their mixtures, which provides a good reference for creating volume-spanning, percolating gels [84, 81, 72, 193, 89, 194].

The study of transient networks has been at the heart of many theoretical [195–197] and experimental studies [198, 199] for their display of complex phase diagrams and dynamics [200]. Different to chemically crosslinked networks such as rubbers, the crosslinks in transient networks can be mediated by the short sticky ends of telechelic polymers [201], telechelic dendrimers [202], triblock-copolymers [203] or charged end-groups [204], which have a finite life time, thus rendering these networks yield-stress fluids. Other transient but active networks are formed by the semiflexible actin filaments crosslinked via proteins are of great importance for giving shape to cells and their locomotion [205]. Vitrimers, in which the bonds or crosslinks can be exchanged through a catalytic process, are another class of transient networks with self-healing properties relevant in biological tissue engineering [206–208]. With their small building

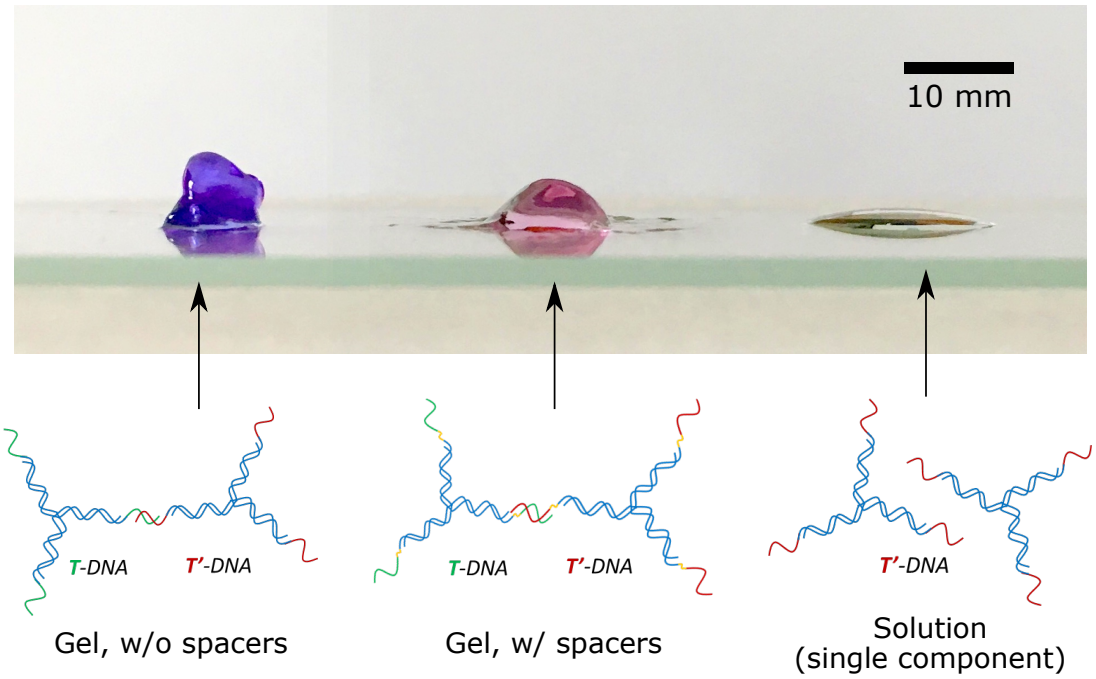

Fig. 3.1 From left to right: DNA hydrogels without free joint, with free joint and only one component. All three samples are made of Y-shaped DNA at 500 µM. The sample maintains its original shape at the time scale of several minutes.

blocks, DNA nano-stars present very similar water-based networks, however, with much greater versatility. Recent rheological studies [209, 210, 185] in the low frequency range showed that the specific structure and connectivity of the DNA-nanostars has a strong influence on their macroscopic mechanical response. However, a detailed understanding of the relation between a repeat-unit and the overall macroscopic response and the related relaxation processes is not yet fully understood. Here we present micro-rheology studies that shed light on these aspects, which aim to be of great importance in the design of new functional materials [68].

Diffusing-wave spectroscopy (DWS), a technique that measures the dynamics of strongly scattering samples [105, 106] is an established technique to perform microrheological studies of complex fluids at much shorter time and length scales than conventional bulk-rheology can achieve [107–110]. Here we present DWS microrheology

studies of DNA hydrogels, probing the rheological properties in a dramatically larger frequency range than the few studies done so far using bulk rheology, where only the effect of built-in flexibility in the joints was measured at the long-time response of the gel [209, 211]. Typical short-time relaxations inherent to the fast making and breaking times of the transient DNA-gel in the melt-transition region can not be accessed in bulk rheology. We elucidate the relation between the system's characteristic binding-unbinding processes and the local and global mechanical properties of the gel over a temperature range that covers the full melting region between the DNA nanostars.

In this chapter, we first introduce the design principle of the Y-DNA building blocks that form the hydrogel and their characterization. Secondly, we present DWS measurements of our Y-DNA system in a concentration range showing a continuous transition from a fluid to equilibrium-gel phase, presenting $G'(\omega)$ and $G''(\omega)$ over a broad range of frequencies and temperatures. We choose this system because it represents an efficient model to investigate the general physics of an n-valent DNA hydrogel with varied rigidities, percolation behaviour and valency. These results will provide strong guidance to future design of more complicated DNA hydrogel frameworks with controlled mechanical properties.

3.2 Materials and methods

3.2.1 DNA-design

The DNA hydrogels used in this study are composed of Y-shaped DNA building blocks made of three partially complementary oligonucleotides (analogous to those described in Chapter 2), here denoted $\mathbf{S_i}$ (Fig. 3.2 and Table 3.1). These single-stranded S-oligos are 41 bases long and consist of four functional parts: a sticky end (9 bases), a free

joint of 4 Thymines providing flexibility, and two segments (I & II) that form the core of the Y-shape. Segments I and II of say ssDNA $\mathbf{S}_1$ are designed to be partially complementary to the respective segments of $\mathbf{S}_2$ and $\mathbf{S}_3$, thus making up the three dsDNA arms at the centre of the Y-shape. Note that the centre is created to be fully binding, leaving no non-binding bases at the center thus reducing its flexibility. The respective binding sequences of the three dsDNA arms are given in Table. 3.1 while the full sequences of the **S**-oligos are given in the Table 3.3. The sticky ends can specifically bind to their complementary sequence due to Watson-Crick pairing. In all following gels we use the same Y-shape cores carrying either sticky ends named **T** or the complementary **T'** DNA, such that Y-shapes with **T**-ends can only bind to those with **T'**-ends. We keep the **T** to **T'** DNA ratio 1:1, thus maximizing the system's connectivity.

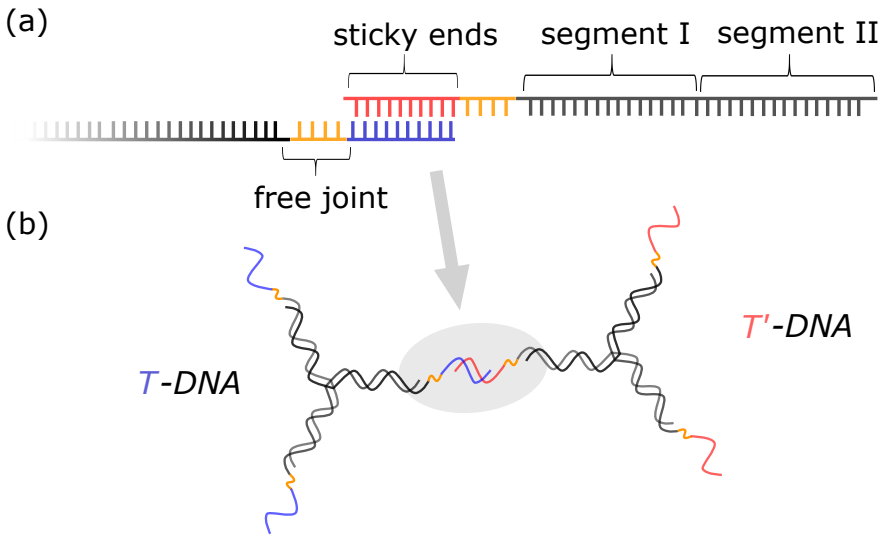

Fig. 3.2 Design and characterization of the DNA hydrogel building blocks. (a) Schematic of the ssDNA $\mathbf{S}_i$ used. Each oligo strand consists of four functional parts: the sticky end, free joint, segment I and segment II. Segment I & II are part of the double stranded core-DNA; sticky ends are for cross-linking the Y-shapes to a network. (b) Cartoon of **T** and **T'** DNA connected via hybridisation of complementary sticky ends.

Table 3.1 The sequences of dsDNA arms

Name	Segment I	Segment II
$\mathbf{S}_1$	5'-TGG ATC CGC ATG ATC	CAT TCG CCG TAA GTA-3'
$\mathbf{S}_2$	5'-TAC TTA CGG CGA ATG	ACA CCG AAT CAG CCT-3'
$\mathbf{S}_3$	5'-AGG CTG ATT CGG TGT	GAT CAT GCG GAT CCA-3'

3.2.2 Oligonucleotides synthesis and Y-shaped DNA hybridisation

Oligonucleotides were synthesized using the DNA synthesizer (BioAutomation MerMade-12, BioAutomation) followed by a HPLC purification process. They were stored in TE buffer (10 mM Tris, pH = 8.0, 1 mM EDTA, and 0 mM NaCl) at 4 °C. Equimolar quantities of the three corresponding strands were mixed in TE buffer solution with 200 mM NaCl to assist the DNA hybridisation process. A total volume of 100 µl DNA mixtures were filled in 0.2 ml PCR tubes. All mixtures were first denatured at 94 °C for 10 minutes, then slowly cooled down to 20 °C at a rate of -1 °C s^{-1}. Finally, we held it at 4 °C. The temperature control process was carried out using a PCR machine.

3.2.3 Oligonucleotides for bulk-rheology

For bulk-rheology and photographic realizations of the gels we used the same DNA sequences as those for the 9 sticky base pairs but with 7 and 12 bp overhangs, as well as the equivalents without the flexible T-spacers. All these oligonucleotides were purchased from were purchased from Integrated DNA Technologies.

3.2.4 UV-vis spectroscopy characterisation

The melting temperature of Y-shaped building blocks was pictured by measuring the 260 nm-peak absorbance of DNA mixture solution using UV-vis spectroscopy equipped with a temperature controlling system.

3.2.5 DNA hydrogels preparation

DNA hydrogels were hybridized by mixing equimolar quantities of T-DNA and T'-DNA in TE buffer with a NaCl concentration of 200 mM. The melting temperature of the sticky ends, T_m = 37 °C, was estimated using the nearest-neighbour model. The temperature was brought up to 45 °C for 20 minutes to break apart the sticky ends and retain the Y-shaped structure at the same time. Subsequently, the sample was cooled down slowly at a cooling speed of 0.02 °C/s to 10 °C. Then, the sample was kept at 4 °C until reused in the next measurement. The total volume of the sample was 200 $\sim$ 500 µl depending on the path length of the performing cuvette.

3.2.6 Tracer particles

We used 600 nm and 230 nm (in radius) polystyrene particles as tracer particles. The particles are densely coated with PEG chains for stablization. The synthesize and coating protocol is described by M. Zupkauskas *et al* [36].

3.2.7 Sample loading

We added 1 % tracer particles into the T-DNA and T'-DNA solutions respectively, and then mixed them up thoroughly. The final sample was loaded into a transparent cuvette holder (optical path length = 1 mm) for future use in DWS measurements.

3.2.8 Diffusing-wave spectroscopy measurements

Diffusing-wave spectroscopy measurements were performed on a commercial DWS instrument (DWS RheoLab, LS Instruments AG) in transmission mode. A 10 mm wide an 1 mm thick cuvette was used as sample cell and the temperature could be controlled within ± 0.2 °C. Calibration was performed on deionized water with the 1 % w/v of

the same tracer particles and the same cuvette to acquire the standard transport mean free path l^* in this setting. The scattering measurement was performed by the machine, outputting an intensity correlation function to a PC for further analysis of the data.

3.2.9 Bulk rheology

Bulk-rheology measurements were performed using a stress-controlled rheometer (Anton Paar MCR 500) with true-gap technology in the cone-plate geometry. In all measurements we used a cone with 25 mm diameter, inclination of 1 °C, and core-plate gap at 50 µm. We performed the oscillatory frequency sweep measurements with angular frequencies ω = 1-100 rad/s under a fixed strain amplitude of 1%, at 10 °C and 20 °C respectively. The temperature control was achieved by a Peltier system equipped on the bottom plate. A custom-made cover was used to minimize evaporation during the measurements.

3.3 Results and discussions

3.3.1 Characterisation of Y-shaped DNA

Melting profiles measured for dilute samples

The melting temperature profiles of the Y-shapes carrying either **T** or **T'** sticky ends (Fig. 3.3) were determined by measuring the absorbance of 260 nm in 1 µM DNA in Tris-EDTA buffer solution at pH = 8.0 containing 150 mM NaCl, as ssDNA adsorbs 260 nm stronger than dsDNA. Starting at 90 °C we observe a plateau in the absorbance until roughly 65 °C, marking the point at which hybridisation (binding) sets in. Until this temperature the individual ssDNAs are all in the unbound state. Upon further cooling the absorption decreases continuously until the low temperature plateau is reached at which all single strands have hybridized into Y-shapes. The melt temperature (denoted

T_m) is defined as the point at which half of all possible base pairs are dissociated. T_{m1} was obtained from the median between the linear curves fitting the low- and high-temperature plateaus and found to be $T_m \approx 58$ °C for both Y-shapes with **T** or **T'** overhangs, for the concentrations used in the melt temperature measurements. As shown previously [23], non-binding ssDNA tails slightly lowered the value of T_m with respect to the value based on tabulated data by Santalucia, which is, averaged over all three arms, $T_{m1} \geq 60$ °C [24].

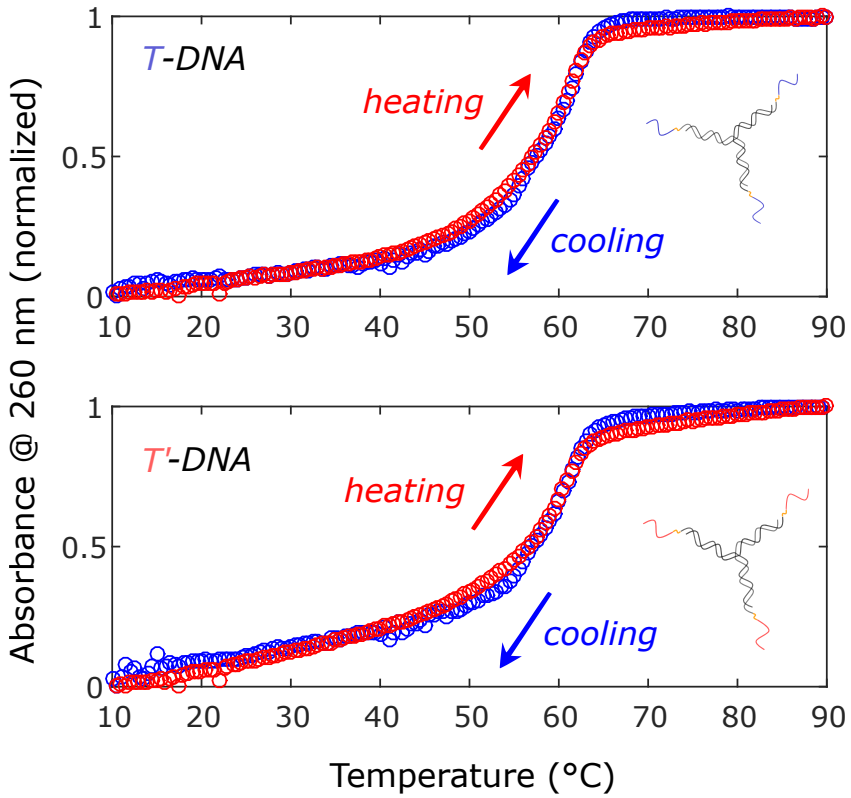

Fig. 3.3 Melting (cooling) and heating (hybridisation) curves of **T** and **T'** DNA in Tris-EDTA buffer containing 150 mM NaCl, measured using by UV-vis spectroscopy.

Estimate of T_{m1} at the gel condition

The melting temperature of dsDNA is estimated by computing the hybridization free energy, ΔG^0, of the complementary sequences, which can be predicted using the unified nearest-neighbor (NN) thermodynamics model[1] [24]. In the NN model, ΔG^0 is computed by summing up the standard free-energy contributions of all neighbouring bases in a DNA sequence, respecting the orientation of the two complementary ssDNA running antiparrallel, plus an initiation energy and the energy contributions coming from the 'dangling ends'; the salt concentration is also taken into account. The enthalpy, ΔH^0, and entropy, ΔS^0, of the strands can be calculated via tabulated values accordingly, and they relate to the Gibbs free energy using Eq. 3.1:

$$\Delta G^0 = \Delta H^0 - T\Delta S^0. \tag{3.1}$$

The melting temperature, T_m, at which half of the double-helical strands are melted, can then be predicted using Eq. 3.2 [24]:

$$T_m = \frac{\Delta H^0}{\Delta S^0 + R\ln(\rho/2)}, \tag{3.2}$$

where R = 1.978 cal/Kmol is the gas constant, and $\rho = \rho_{AA'} = \rho_A = \rho_{A'}$ is the concentration of the dsDNA, when all ssDNAs are hybridized. An empirical salt concentration effect is also included as a compensation in ΔG^0.

However, the T_m of our structure is influenced by further factors: (i) Since three arms are joined together in our Y-shapes, they should not be treated as independent double helices; (ii) di Michele et al. [23] have shown that inert tails on dsDNA (here the sticky overhangs) cause a decrease in melting temperature by about 3 °C to 7 °C, depending on the length of these inert tail; (iii) The solvent conditions will

[1] Details see Section 1.1.2.

also influence T_m. In this study we used TE buffer (10 mM Tris, 1 mM EDTA, adjusted to pH 8.0 with HCl) to stabilise the DNA. For instance, the T_m of a given complementary pair AA' in TE buffer is different to that in de-ionized water. The analytical approach to comprise all these effects in Eq. 3.2 is unavailable, but we can combine the experimental measurements and the NN model routine to estimate the melting curves for experimental conditions that do not allow a direct measurement of T_m.

Table 3.2 The sequences of dsDNA arms and the predicted T_m

Name	Sequences	Predicted T_m (@[NaCl]=150 mM, [DNA]=1 µM	Predicted T_m (@[NaCl]=200 mM, [DNA]=500 µM)
Arm 1	5'- TGG ATC CGC ATG ATC - 3' 3'- ACC TAG GCG TAC TAG -5'	55.27 °C	68.91 °C
Arm 2	5' - TAC TTA CGG CGA ATG - 3' 3' - ATG AAT GCC GCT TAC - 5'	52.47 °C	65.69 °C
Arm 3	5'- AGG CTG ATT CGG TGT - 3' 3' - TCC GAC TAA GCC ACA - 5'	57.34 °C	71.31 °C

Table 3.2 lists the calculated melting temperatures of three arms for an added NaCl concentration of 150 mM and a total ssDNA concentration of 1 µM based on the NN model. We took the average melting temperatures of these arms as the melting temperature of the Y-shaped body as the starting point, i.e. $T_m^{Y-shape} = \frac{1}{3}(T_m^{arm1} + T_m^{arm2} + T_m^{arm3}) \approx 55.02$ °C. This is comparable to the experimentally measured melting temperatures for T-DNA and T'-DNA described in the main text, which indicates that the three factors mentioned above can compensate each other in our case. Similarly, we estimated the averaged melting temperature of the Y-shaped body at the working condition ([NaCl]=200 mM, [ssDNA]=500 µM, in TE buffer) being 68.64 °C.

PAGE characterisation

To check the hybridization effectiveness of the Y-shaped DNA, we performed polyacrylamide gel electrophoresis (PAGE) with a 10 % gel. The preparation of the gel is introduced in Appx. A. The loading sample contains $50 \sim 250$ ng DNA strands in total and $1\times$ gel loading dye (Purple, New England BioLabs ®) per lane. DNA ladders were loaded into lane 5 (Low Molecular Weight DNA Ladder, New England BioLab ®) and lane 10 (50 bp DNA Ladder, purchased from New England BioLab ®) to scale the migration of the DNA samples in the parallel lanes (Fig. 3.4). The specific sequences used for PAGE are listed in Table 3.3: f_1, f_2 and f_3 are the components of T-DNA; f_{p1}, f_{p2} and f_{p3} are for T'-DNA. So $f_{(p)i}$ and $f_{(p)j}$ $(i, j = 1, 2, 3$ and $i \neq j)$ are partially complementary to each other, and therefore can hybridize together at room temperature. Lanes 1-3 were loaded with the mixture of f_i and f_j $(i, j = 1, 2, 3$ and $i \neq j)$ at 1:1 molar ratio , and lane 4 was loaded with the mixture of f_1, f_2 and f_3 at 1:1:1 molar ratio. Lanes 6-8 were loaded with the mixture of f_{p1} and f_{pj} $(i, j = 1, 2, 3$ and $i \neq j)$ at 1:1 molar ratio, and lane 9 was loaded with the mixture of f_{p1}, f_{p2} and f_{p3} at 1:1:1 molar ratio. The samples were electrophoresed at 100 V for 90 min at room temperature.

The electrophoresis results are shown in Fig. 3.4. The sharp and distinct principle bands in lanes 1-4 and lanes 6-9 show a high-yield hybridization of DNA complexes. The principle bands in lane 1-3 and 6-8 were near the position of the 50 bps marker in lane 10, in accordance with the mass of the two hybridized ssDNAs (46 bases per ssDNA). The dark bands in lane 4 and lane 9 represent the migration of the T-DNA and T'-DNA complexes respectively.

Table 3.3 The oligonucleotides sequences of PAGE loading samples

Name	Sticky end	Free joint	Segment I	Segment II
f_1	5'- TGT CAC TCA CAG	TTTT	TGG ATC CGC ATG ATC	CAT TCG CCG TAA GTA -3'
f_2	5'- TGT CAC TCA CAG	TTTT	TAC TTA CGG CGA ATG	ACA CCG AAT CAG CCT -3'
f_3	5'- TGT CAC TCA CAG	TTTT	AGG CTG ATT CGG TGT	GAT CAT GCG GAT CCA -3'
f_{p1}	5'- CTG TGA GTG ACA	TTTT	TGG ATC CGC ATG ATC	CAT TCG CCG TAA GTA -3'
f_{p2}	5'- CTG TGA GTG ACA	TTTT	TAC TTA CGG CGA ATG	ACA CCG AAT CAG CCT -3'
f_{p3}	5'- CTG TGA GTG ACA	TTTT	AGG CTG ATT CGG TGT	GAT CAT GCG GAT CCA -3'

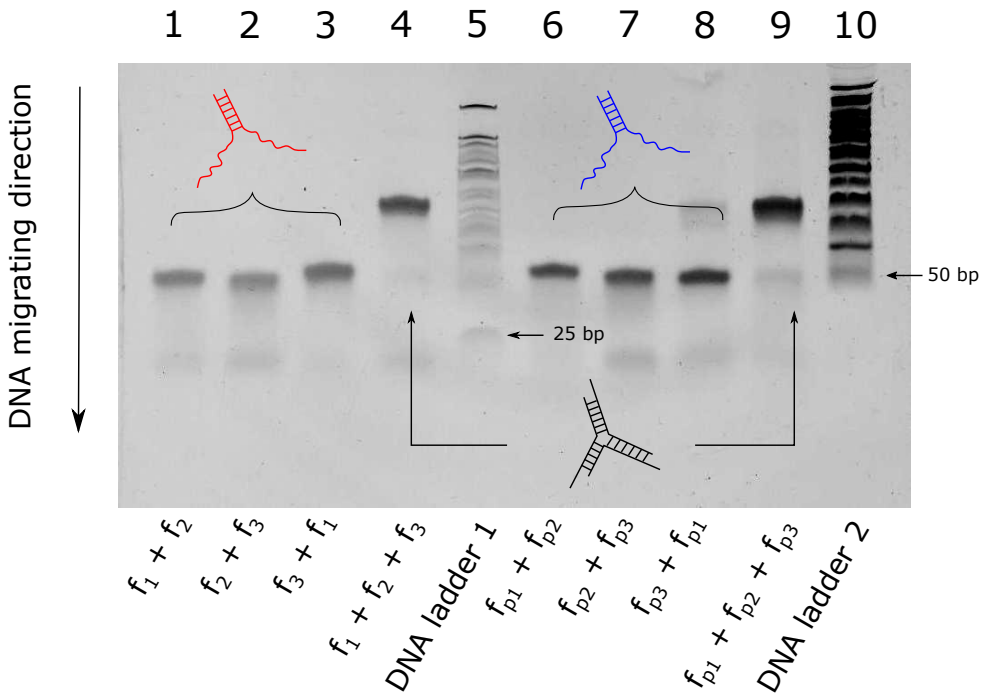

Fig. 3.4 Polyacrylamide gel electrophoresis characterization on various ssDNA mixutres.

3.3.2 DWS microrhelogy using 600 nm probe particles

Our DNA hydrogels were studied using DWS in echo-mode of the Light Instrument Rheolab allowing for long correlation times. The light source was a 685 nm wavelength diode laser. The measured ICF where fitted and then converted into a mean-squared displacement (MSD) using both the instrument software and for comparison a home-written software. The procedures are detailed in the Section 3.2.

Intensity-correlation function (ICF)

DNA-hydrogel samples were made by preparing **T**- and **T'**-DNA solutions separately both at a DNA concentration of 500 µM (see Section 3.2), already containing the tracer particles. The cuvettes were filled with the respective **T**- and **T'**-DNA solutions, which are liquid at room temperature (RT) in a layer-by-layer fashion at RT for better mixing. The total filling volume was $\sim$ 500 µl. Initially the interfaces between the layers gelled due to the rapid hybridisation at RT. To obtain well mixed samples we heated the cuvettes to 50 °C and incubated them for 20 minutes, which was sufficient to fully melt the sticky ends rendering the sample a well-mixed fluid of Y-shapes, but also cold enough to preserve the Y-shaped structure. Following this procedure we ensured that the final DNA concentration in the fluid phase remained 500 µM, corresponding to $\sim$20 mg/ml, containing 1 % w/v PS particles. No detectable depletion was observed in the sample through the measurement.

DWS measurements were done starting at 50 °C and slowly cooled down to 20 °C. We measured the scattering intensity in 1 °C intervals, and equilibrate the sample for 5 min prior to data acquisition, ensuring the full coverage of the melting transition of the sticky ends. The scattered intensities were then converted into ICFs and MSDs. We performed control experiments using 230 nm large PS particles testing both for a possible dependence of our results on particle size and for hysteresis in the gelation process by repeating the scattering measurements in a cooling and heating cycle following the same protocol as for the larger particles. The results, shown in the Appx. B, confirm that we only probe the viscoelastic properties of our DNA-hydrogel and that it is a thermally reversible equilibrium gel. The ICF data for the cooling ramp are shown in Fig. 3.5.

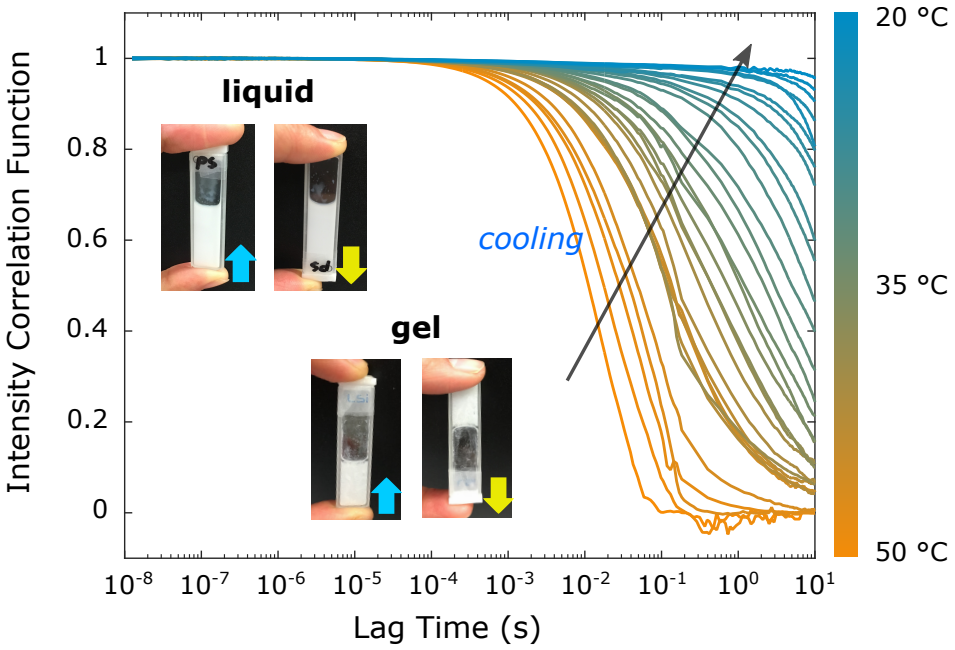

Fig. 3.5 Temperature-dependent intensity-correlation function (ICF) curves measured for the 500 µM DNA hydrogel, containing 1 v/v % 600 nm large, sterically stablised polystyrene tracer particles. The ICF curves were measured starting from 50 °C (orange lines) in 1 °C steps cooling down to 20 °C (blue lines). The photographs show the sample cuvette showing the samples liquid state at 50 °C *top left* and the gel state at 20 °C to *bottom rightt* .

Mean-square displacement (MSD)

Several simulation and experimental studies explored the phase diagram of DNA-hydrogels made of nano-stars with 2-, 3- and more bridging arms [81, 72, 193, 212]. These studies showed that the region where a phase-separation into a nano-star poor and nano-star rich region becomes increasingly more narrow, shifting to the lower DNA-concentration end for decreasing valencies [81]. Here we used a total DNA concentration of 500 µM ensuring that we are firmly in the one-phase region (Fig. 3.6) with the hydrogel spanning the entire sample. This entails that as we cool the sample from 50 °C to RT the entire sample is brought continuously from a fluid phase containing free Y-shapes to a percolating gel network. In order to obtain a clear signature of this network formation its melt temperature $T_{m2} \approx 35$ °C must be well below T_{m1} of the

individual Y-shapes. This melt-temperature separation was achieved by increasing the added salt concentration to 200 mM NaCl [23]. The melting temperature will also depend weakly on the DNA concentration shifting our systems' T_{m1} to $\sim$ 62 °C, but cannot be measured directly as such high DNA concentrations are adsorbing too strongly. Also T_{m2} cannot be measured by UV adsorption as its signal is small compared to that of the dsDNA in the Y-shape.

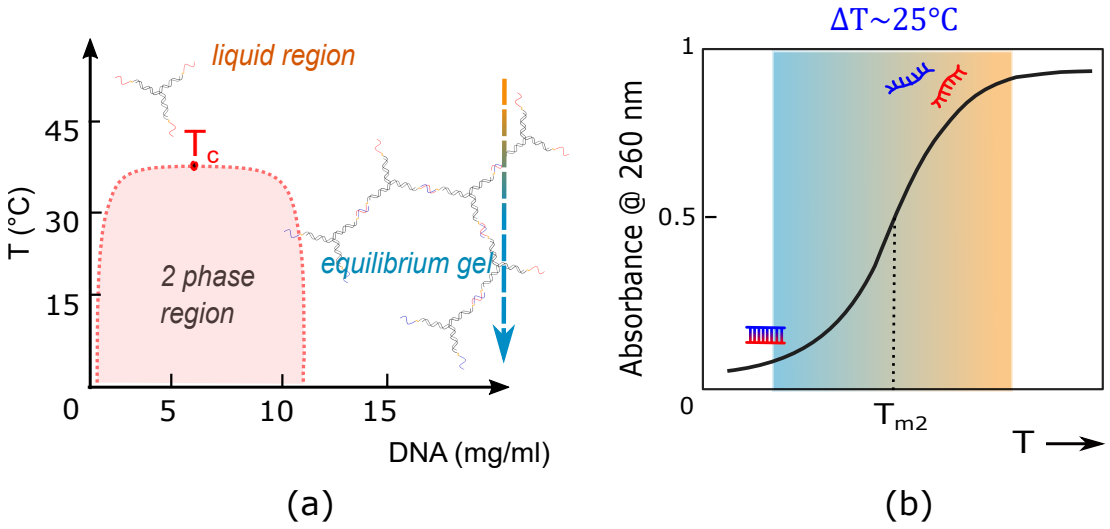

Fig. 3.6 (a) Schematic phase diagram of the Y-shaped DNA replotted from [81]. The arrow indicates the concentration and temperature range of the ICF measurements shown in Fig. 3.5. The red area represents the two-phase region, and T_c the critical point. The red area represents the two-phase region, and T_c the critical point. (b) Illustration of melting curves of the sticky ends. The blue-yellow area represents the melting transition.

The MSD results extracted from the ICF curves are shown in Fig. 3.7. At temperatures well above T_{m2} (orange lines), the MSD curves depend linearly on the lag time τ over the whole measured region, confirming the $\langle \Delta r(t)^2 \rangle \propto \tau$ relation for Newtonian fluids and thus proving that in the temperature window between about 55 °C and 45 °C, our system behaves like a fluid of disconnected Y-shapes dispersed in a buffer-colloid solution. However, compared with the calculated MDS for 600 nm PS particles dispersed in pure water with a diffusion constant D = 0.72 µm^2 s^{-1} at

50 °C our sample displays a diffusivity that is two orders of magnitude lower. A similar decrease is observed in the control measurements using 230-nm large PS particles. This decrease cannot be due to the presence of the colloids, which would lower the diffusion coefficient only by 2 % according to the Einstein relation for the viscosity of colloidal dispersions or the buffer conditions. Hence the observed increase in viscosity is purely due to the high DNA-concentration. Indeed, assuming that the Y-shapes take up an effective spherical volume due to rotational diffusion (assuming that each arm is $\sim$ 5 nm long) the approximate volume fraction occupied by the Y-shapes is some 40%, although the actual DNA content is only 2 weight %.

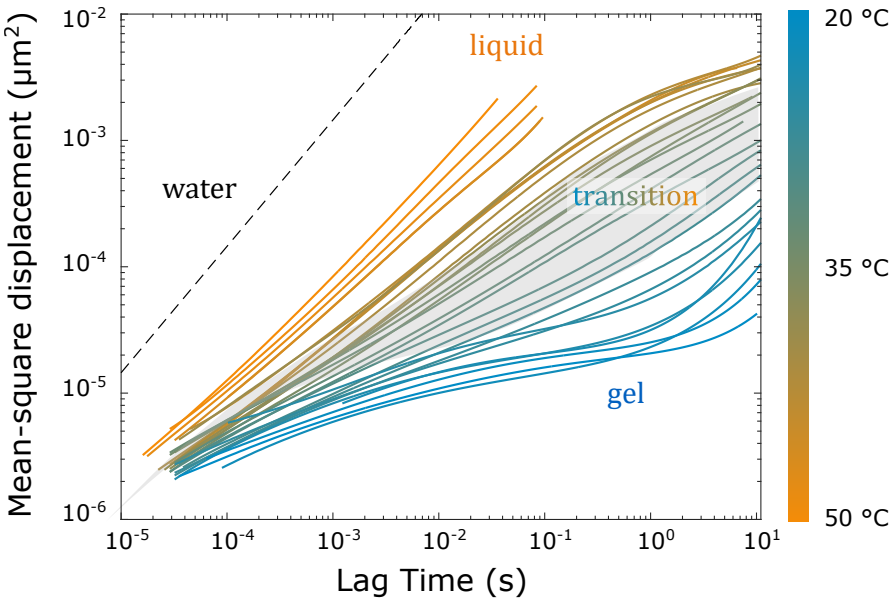

Fig. 3.7 Schematic phase diagram of the Y-shaped DNA. The arrow indicates the concentration and temperature range of the ICF measurements shown in Fig. 3.5.

At $T < 30$ °C and short lag times, the MSD curves are similar to the high-T measurements increasing with increasing ω, however with a slightly lower exponent indicating subdiffusive motion of the local bridges between crosslinks. At intermediate ω corresponding to longer relaxation times, for instance of the 'cages' formed by the crosslinks, the MSD curves reach a plateau. Holding the sample at this lower

temperature over 20 minutes and measuring the ICF in 5 minutes' intervals show that there is no further increase in the plateau value (see SI). This is also expressed in the flattening of the corresponding elastic moduli G' presented in Fig. 3.8. This means the tracer particles remain locally diffusive on short time scales (the diffusion coefficient of the particles in pure water is 1.65 $\mu m^2\, s^{-1}$ at 20 °C) , but are confined by the percolating DNA-network on long time scales. The transition region marked by the changing colors in Fig. 3.7 and Fig. 3.8 represents the melt-temperature region over which the fraction of hydrogen bonds formed between two Y-shapes with complementary sticky ends is gradually increasing as T decreases. Using refined Santalucia rules for hybridisation [23] we estimate the width of this transition region to be $\Delta T \sim 25$ °C (see Fig. 3.6(b)). With a $T_{m2} \sim 35$ °C this means we should reach a fully bonded state and thus a maximum network stiffness at around $T \sim 25$ °C. A detailed discussion of the value of the stiffness is given in the following.

Complex moduli: G' and G''

The elastic, $G'(\omega)$, and viscous moduli, $G''(\omega)$, measured in a cooling cycle are shown in Fig. 3.8. Again, similar results were obtained using the smaller tracer particles in a cooling and heating cycle (see SI), suggesting that the equilibrium gels display only very small hysteresis effects. As expected, the elastic modulus, $G'(\omega)$ undergoes a significant change as the temperature changes over the melting-temperature region, while $G''(\omega)$ retains the same linear trend until about 30 °C. At high temperatures (orange lines), G' is nearly zero at long time scales as the solution is in a fully fluid state of Y-shapes, but is non-zero at high frequencies reflecting the fact that the sample is a quasi-concentrated solution of elastic-shapes behaving like soft colloids. Indeed, above T_{m2} the loss modulus dominates (Fig. 3.9(c)). However, around the melting temperature (between 37-31 °C), $G'(\omega)$ and $G''(\omega)$ run parallel and on top of each other,

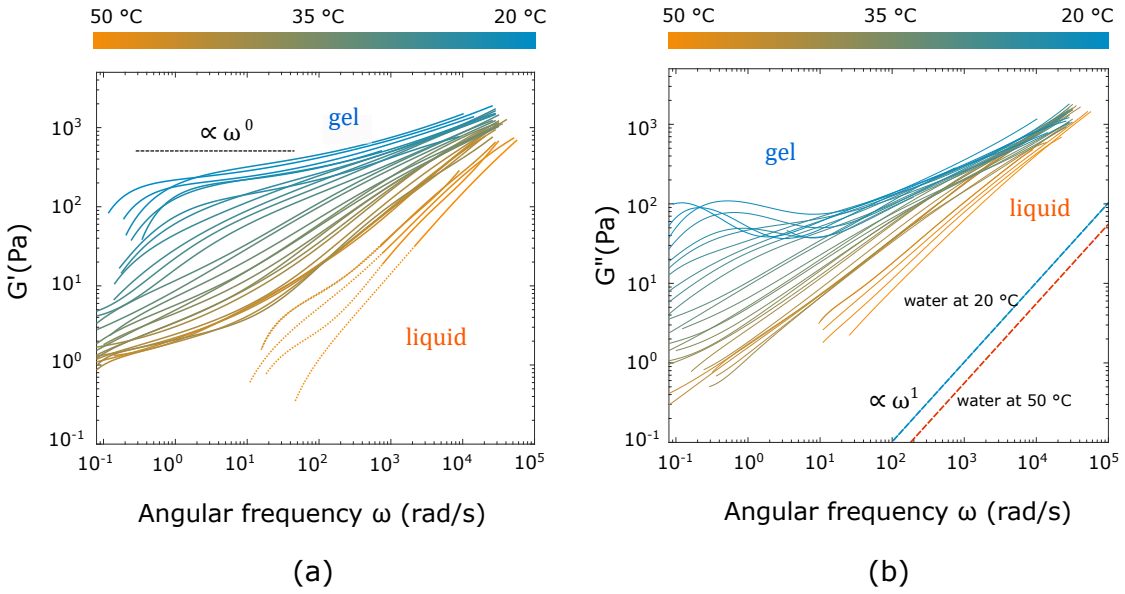

Fig. 3.8 Temperature-evolution of the complex moduli $G'(\omega)$ and $G''(\omega)$ as a function of frequency extracted from the MSDs in Fig. 3.7. (a) The elastic moduli $G'(\omega)$ measured in a cooling ramp. At temperatures above T_{m2}, G' drops down at a frequency below $10^2 \sim 10^4$ rad/s, showing close-to-zero elasticity; below T_{m2}, only th eonset of the decay in the ICF could be monitored. Hence the low-frequency region is plotted as dashed lines using extrapolations. (b) The viscous modulus $G''(\omega)$ in cooling (*top*) ramp.

which we identify as the point of full percolation. This percolation can be understood when looking at Fig. 3.6(b): in the melt-transition region increasingly more Y-shapes bind to each other forming many clusters that grow in size as the temperature decreases. At T_{m2} half of all possible hydrogen bonds or base pairs are bound, which does not mean that half of all Y-shape arms are bound at all times but that they continuously form and break partially and thus on average form a single cluster. Below T_{m2} the fraction of hybridized base pairs continues to increase until about 25 °C and also their life time becomes longer. At even lower temperatures (blue lines), the G' reaches a plateau value of $\sim$ 400 Pa in the intermediate time range, which corresponds to a mesh size $\xi \sim 21.5$ nm, assuming the scaling behaviour of the bulk modulus $G_{bulk} \propto k_B T/\xi^3$. This is in good agreement with the calculated mesh size from the design that suggests

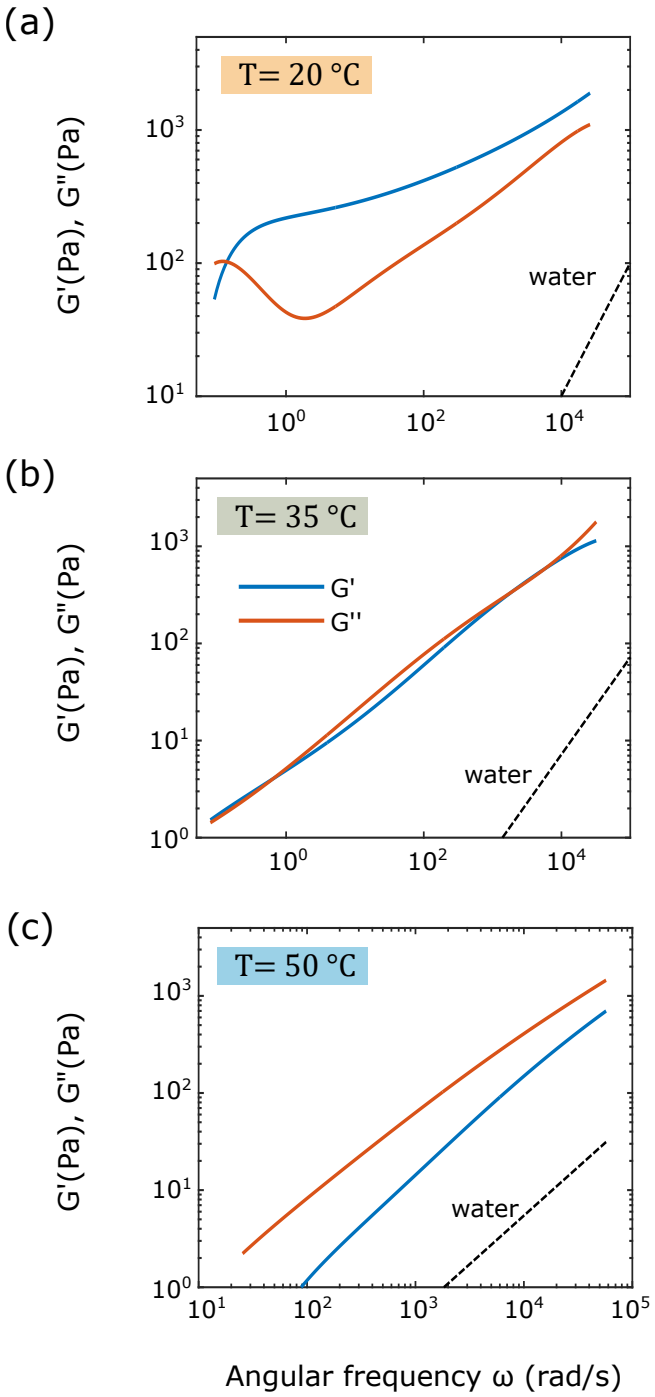

Fig. 3.9 Comparison of $G'(\omega)$ and $G''(\omega)$ at temperatures of 20 °C, 35 °C, and 50 °C, representing typical behavior at temperatures below, around, and above T_m. (a) At 20 °C, G'' is higher than G' at frequencies below the crossover frequency $\sim 10^4$ rad/s. (b) At 35 °C, G' and G'' are overlapping over almost the entire frequency range. (c) At 50 °C, G'' is higher than G' over the whole measurable frequency range, showing no crossover point at all.

an average distance between bonded Y-shape centres of $\xi \sim 20$ nm corresponding to a slightly higher elastic modulus.

Interestingly, below $T \sim 25$ °C our fully formed network is very similar to that of classical transient networks of flexible polymers held together by crosslinks through physical interactions that constantly form and break (Fig. 3.9) [196]. The frequency behaviour of such transient networks shows a typical Maxwellian $G''(\omega) \propto \omega$ increase at long times, reflecting the fact that the **TT'** bonds between the Y-shaps are not irreversibly formed. In fact, we see a crossover between the steeper increasing $G'(\omega)$ and $G''(\omega)$ at around 1 s^{-1}, which is know to correspond to the life time of the short double-stranded bond between two Y-shapes at RT, and can be explained by the reptation model for associative polymers [197, 195]. Note that we cannot determine the exact crossover as the errors in our DWS measurements start to diverge at smaller frequencies. However, as expected this crossover frequency increases slightly as the temperature rises, reflecting the decrease in the bond life-time (Fig. 3.9). A similar observation was made in dynamic light scattering experiments on gels of 4-armed nanostars [194]. This crossover is then followed by a plateau in $G'(\omega)$, while $G''(\omega)$ decreases slightly for some intermediate frequency range before both moduli start increasing again at higher frequencies. In our case this dip in $G''(\omega)$ might be ascribed to the fact that the elastic network dominates in this time regime before a sufficient number of bonds break and the tracer colloids can move. Consequently, this dip in $G''(\omega)$ disappears when the temperature reaches the melt-transition region when the life time of the bonds decreases further and the viscous contributions increase. At even higher frequencies $G''(\omega)$ gradually reaches the linear behaviour in ω as it reaches the fully liquid state by coming from a weakly sub-diffusive behaviour in the transition region, while $G'(\omega)$ reaches a power-law behaviour with a fractal exponent. In the gel phase this upturn in $G'(\omega)$ at high frequencies is simply due to the fact that the bond

life-time is now longer than the typical motion due to thermal fluctuations and thus the system shows the typical increase in elasticity as the system cannot relax fast enough. This is associated with its second crossover between the two moduli appears to occur at $\omega_c \approx 4 \times 10^4$ Hz at temperatures at $T \sim$ 35-50 °C (Fig. 3.7). At this high frequency, the main elastic contribution must come from the cluster phase, with clusters forming 'cages' of the Y-shapes. These completely disappear at even higher temperatures.

We made an exciting observation when performing low-frequency bulk-rheology measurements on the very same system, in which we removed the flexible linkers. The measured $G'(\omega)$ and $G''(\omega)$ curves showed an increase by a factor of up to 7, which was also observed when using the samples with and without flexible linkers but 12 instead of 9 bases (Section 3.3.3). This stiffening is particularly visible in the photograph shown in Fig. 3.1. Moreover, further DWS data (see Fig. 3.10) on the 12 bp sticky ends also confirm that the percolation transition coincides with the system's melting transition, only that now that transition occurs at $\sim$ 44 °C, the T_{m2} for the 12 bases.

Finally, at $T \gtrsim 35$ °C we can plot the half-time of the relaxation of the ICF as inverse function of temperature. The slope of the resulting Arrhenius plot provides us with the strength of the bonds between two Y-shapes, where the relaxation time $\tau = t_{1/2} = \tau_0 \exp(-\Delta H/\mathrm{k_B}T)$. Following the arguments by Nava et al. [90] this will happen when at least 2 bonds per Y-shape are broken, which corresponds to about 60 kcal/mol in our case.

3.3.3 Bulk rheology

Bulk-rheology measurements were performed to measure both the low temperature behaviour $G'(\omega)$ and $G''(\omega)$ and their change, when the flexible thymine-linker was removed. Finally, also differently long sticky overhangs were tested while keeping the centres of the Y-shapes unchanged.

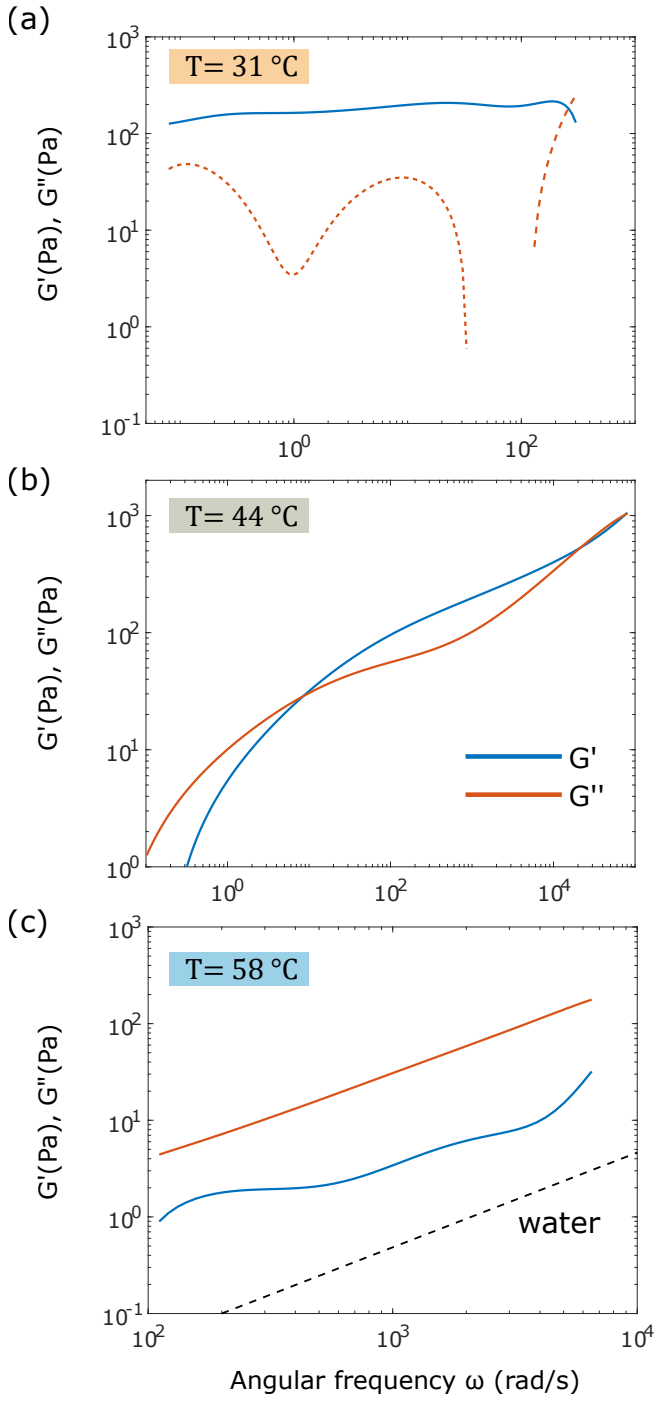

Fig. 3.10 Comparison of $G'(\omega)$ and $G''(\omega)$ of hydrogels with 12-bp sticky ends at temperatures of 31 °C, 44 °C, and 58 °C, representing typical behavior at temperatures below, around, and above T_m.

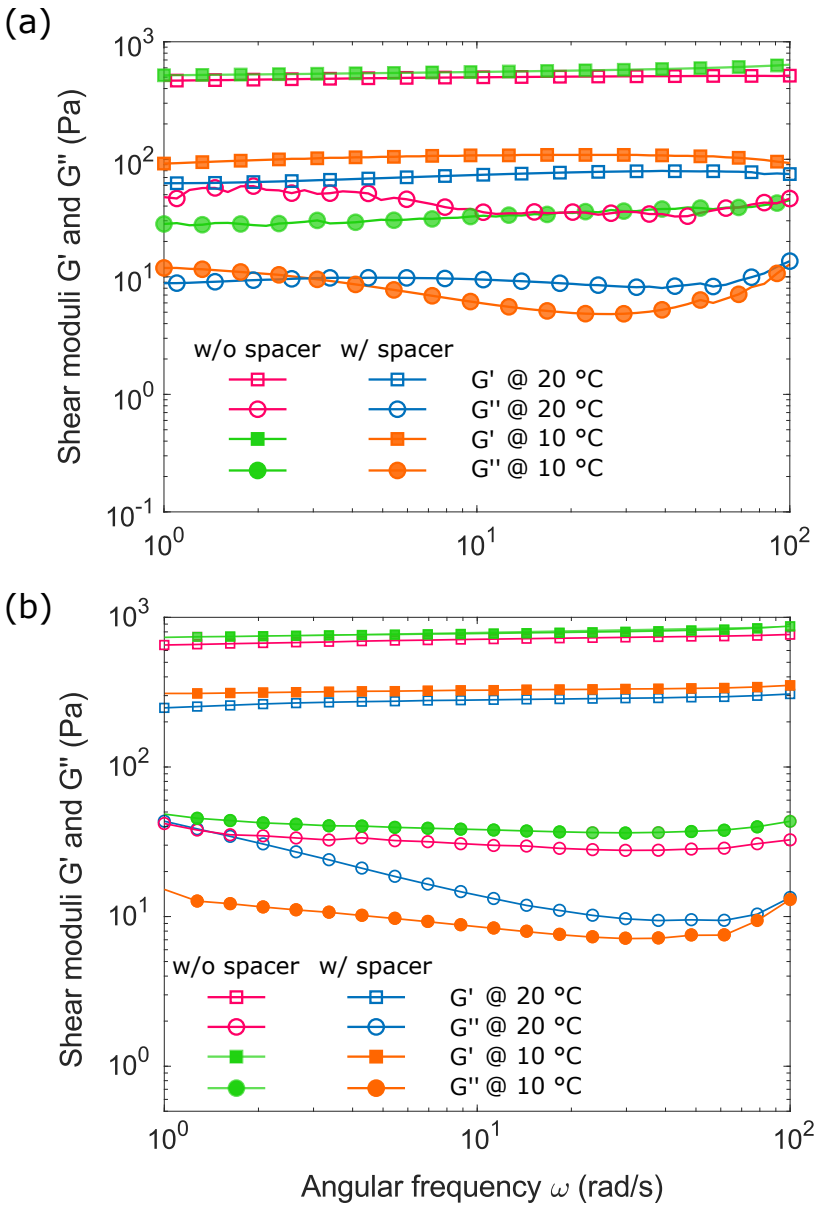

Fig. 3.11 Bulk-rheology measurements on 500 µM concentrations of **T** and **T'**-DNA nanostars (a) for sticky overhangs with 12-bases and (b) the same 9 bp overhangs used in all microrheology measurements presented. Also the same buffer and salt conditions were used.

To demonstrate the effect of the flexible linkers, we performed bulk-rheology measurements on the **T** and **T'**-DNA system with the 9 bp long sticky overhangs, both with and without flexible linker. We compared these with the very same system (same concentration) but with 12 bp overhangs - again with and without flexible linkers (Fig. 3.11). In order to avoid too much evaporation during the measurements we preheated the lower plate of the rheometer to 30 °C with the cone in close proximity, then lifted the cone to quickly place the gel and immediately afterwards lowered the cone to measuring position. The geometry was then enclosed with a vapour trap. After a 10-minute equilibration time we lowered the system's temperature to 20 °C. This procedure does not allow for careful equilibrium hybridization of the sticky overhangs and as we loaded the samples in the gel state they had been strongly sheared, but slow cooling form 50 to 20 °C would compromise our samples. Nevertheless, the bulk-rheology results closely match the results obtained with DWS at low frequencies for the 9 bp overhang system with flexible linker, showing a bulk-elasticity plateau at around 200 Pa. And also G"(ω) dips down slightly at higher frequencies, as was observed in the DWS measurements. When further cooling the sample to 10 °C both moduli do not change much. In fact the plateau value of G'(ω) only increases by a few percent, which illustrates that although we loaded the sample in a crude way, we control the systems elasticity purely by the *known* number of crosslinks we add to the system, which are all connected to each other at 20 °C. The exciting only change we achieve is by removing the flexible linkers leading to the increase of the elasticity plateau to about 500 Pa. As explained in the main text, this is due to the fact that by the removal of the flexibility in the system we transfer the system from a transient network of flexible linkers dominated by entropy to a more rigid energy driven network.

Comparison with the same system, in which we replaced the sticky overhangs with 12 bases (5'- TGT CAC TCA CAG and 5'- CTG TGA GTG ACA for the **T** and

T'-DNA shapes) respectively showed a very similar behaviour. As for the system with 9 bases overhangs we measure a similar bulk elasticity of about 90 Pa when incorporating the flexible linkers, which increased now by a factor of 7 when the flexible linker is removed. Note that although the systems transition to a gel occurs now at even higher temperatures (for details see below) while keeping the concentration of the linkers the same we still obtain a very similar bulk elasticity. The small variations value at 20 °C is simply due to the loading procedure and the fact that in bulk-rheology each loading can lead to variations of about 10% because every time a slightly different amount may be used. The striking result is the increase in G'(ω), which is purely due to the absence of the flexible linkers.

3.4 Conclusions

To summarise, our micro-rheological measurements demonstrate how a transient cross-linked hydrogel is formed as it is brought from the high temperature range, where the Y-shaped building-blocks form a viscous fluid, into an equilibrium gel-phase. Remarkably, once all possible bonds are formed below the melt-transition region the DNA-hydrogel shows a frequency behaviour very similar to that of transient networks of flexible polymers, although the connection between two Y-shape centres is not a fully flexible polymer but rather two semi-stiff dsDNA strands connected via two short, flexible ssDNA linker and another rigid dsDNA (**TT'**) bond.

Interestingly, when the flexible ssDNA linkers are removed while keeping the same Y-shape density, the elasticity of such a network increases 7-fold, indicating that the network goes from a flexible, entropy-driven to a more elastic system that is dominated by the energy of the semi-stiff connectors between the Y-shape centres. Testing two differently long sticky bonds, we also show their melt-temperature T_{m2} could be identified as the percolation transition. It should be noted that the results

presented here cannot be obtained by regular bulk-rheology because for evaporation problems, but also single-bead microrheology would lead to ambiguous results due to local heating around the laser-trapped probe particles.

Our findings show that we can develop a new class of hydrogels with more ordered, local structure, or if 'cooling in' a cascade of hybridisation temperatures hierarchical structures. These could be achieved by introducing locally more rigid DNA building blocks. Such networks could be envisaged as builders of thermo-responsive materials that could provide controlled drug released, or as micron-sized actuators with well-defined elastic modulus.

3.5 Acknowledgement

I would like to thank Tianyang Cao for synthesising the ssDNAs, and for conducting the bulk rheology measurements together with Iliya Stoev, Nick Hawkins for providing technical assistance in DWS measurements, Alessio Caciagli for DWS algorithms and useful discussion in MR data analysis, Mykolas Zupkauskas for providing the functionalised particles.

Chapter 4

A Coarse-grained simulation of DNA hydrogels

Massive computational models of DNA at a wide range of coarse-graining levels have been proposed in recent years, each focusing on different aspects of DNA nature. My interest lies on the simulation of large-scaled DNA hydrogel systems, which could represent the experimental model introduced in the previous chapter, or its variations. Therefore, in this chapter I will introduce a coarse-grained simulation model of DNA hydrogels consisting of Y-shaped DNA as building blocks. In this model, each building block comprises of three dsDNA arms with ssDNA sticky overhangs, mimicked by chains of beads and patchy particles respectively. Melting curves are sketched to demonstrate the validity of the model, and the radial distribution function and linear elasticity are later calculated to extract informations on the structural and mechanical properties of the system in bulk. Our model offers a computationally cheap approach to explore the bulk properties of a percolating DNA hydrogel system and provides guidance for future design of DNA hydrogels with different building blocks.

4.1 Introduction

As discussed in previous chapters, DNA hydrogels belong to a class of semi-flexible polymeric network that consist of synthetic nucleotide strands whose binding is governed by the strict rules of base pair complementarity [56, 68, 71, 81]. The ability to precisely synthesize base sequences, and thus to specify the binding rules *a priori*, makes DNA-based systems superior to conventional polymeric networks with non-specific interactions [213, 55]. Thanks to this uniquely programmable behaviour, DNA hydrogels have found applications in areas such as drug delivery [56], 3D cell cultures [176], and bio-printing [62]. In recent works, the phase diagram and some aspects of the rheological behaviour of DNA hydrogels have been revealed [84, 81, 72, 193, 214, 215], but robust links between base complementarity and structural and mechanical properties of the resulting hydrogel at the bulk level are missing. Here we establish a simulation model for DNA hydrogels that offers predictions of the structural and mechanical properties of the sample in bulk. Our model can serve as a supplement to ongoing experiments and could provide instructive guidance for future material design.

Computational models of DNA at a wide range of coarse-graining levels have been proposed, each focusing on different aspects of DNA nature. For instance, atomistic models [134, 138, 139] that provide detailed dynamics of nucleotides have advantages in investigating DNA folding and protein-nucleic acid interactions, while bead-spring polymer models with up to 3000 base-pairs represented by one single bead offer a means of obtaining bulk material properties at considerably lower computational expense [135, 140]. Models adopting an intermediate level of coarse-graining have also appeared, most notably the OxDNA model [156], which has been utilised in simulating several DNA nanotechnological systems [153, 126, 128, 216]. The model represents ssDNA as a chain of rigid nucleotide beads with effective interacting sites that can

reproduce the thermodynamics and structural properties of single strands and duplexes with DNA specificity.

The sequence specificity is, however, not always required for simulating self-assembled DNA systems, especially when all the possible ssDNA interactions are well known. In these cases, the whole interacting ssDNA sequence can be treated as a single 'patch' with its potential matching the physical rules [217–222] from the viewpoint of thermodynamics and statistics. This approach maintains the function of ssDNA as selective bridges and at the same time accelerates the simulation process allowing for large numbers of repeating units that assemble into large, geometrically-accurate, topological structures.

With regard to DNA hydrogels, our interest lies in the structure and mechanics of large-scale systems (e.g. a DNA polymeric network assembled by at least hundreds of Y-shaped DNA units), hence base-pair models [156, 131–133] are too detailed. Computational models on DNA gels self-assembled from branched DNA complexes have been proposed to mimic the bulk behaviour of the system, particularly focusing on the assembly and gelation processes [84, 223]. In those models, structural disorder of such systems has been demonstrated and further discussed, but deeper studies on the possible microstructures of the network, which may facilitate future design of the system, is still absent. Furthermore, the bulk mechanical properties of DNA gels have not been mentioned in any of the present models, but these parameters are actually key in testing some of the functions of the materials. These are limited by the design of the models. In F. Starr and F. Sciortino's model [223], the basic geometry of the DNA building blocks is not retained, and thus the microscopic structures cannot be accurately represented. While in other cases where oxDNA model or its equivalences were used [193, 84], the calculation is too heavy to apply due to the consideration of the specific sequences in building blocks. Therefore, a computational model of DNA

hydrogels that both retains the DNA binding rules and is light enough for calculating the bulk properties, is in great need.

Here, we discuss one class of DNA hydrogels that is self-assembled from tri-valent building blocks, which are known in the literature as DNA nanostars or Y-shapes in the case of nanostars with three arms. The system is constructed of three arms made of semi-soft beads, where the terminal beads have attractive patchs that represent the ssDNA sticky ends [224]. All Y-shapes in the system have the same core structure; for illustrative purposes half of them have only one type of sticky ssDNA on all three arms, while the other half carries the complementary ssDNA, which is represented as a complementary sticky patch. We first give a detailed account of the numerical model, and then go on to explore the system's melting behaviours, structural properties and linear bulk elasticity.

4.2 The model

4.2.1 Y-shaped building blocks

The geometric and interaction parameters in our model were chosen to best represent the structure of Y-shaped DNA units, motivated by the experimental work conducted by Xing et al [215]. Our simulation uses a *bead-spring* model to represent the dsDNA arms (see Fig. 4.1), with attractive *patches* to mimic the ssDNA sticky ends (Fig. 4.2(a)). Each of the Y-shaped repeating units comprises ten beads: one central bead; six structural beads arranged in three arms; three patch beads, with one at the end of each arm. The neighbouring beads in each arm are connected by harmonic bonds that are kept approximately linear by an angular potential with minimum at 180°; the three arms are equally distributed around the central-bead with minima at 120° (see below and Fig. 4.1). The three patch beads provide attractive sites on the outer surface of

the terminal bead of each arm. For simplicity, we define two patch types, symbolised as *patch A* and *patch B*, which represent two complementary DNA sequences. The attraction is only enabled for patches in different types (A-B); for patches in the same type (A-A or B-B), they repel each other.

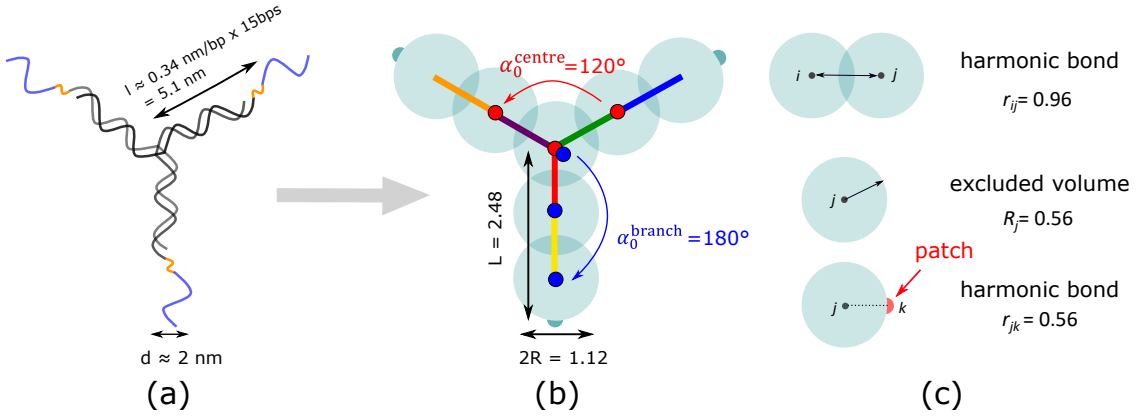

Fig. 4.1 Schematic of the bead-spring representation of Y-shaped units.

The model is implemented in LAMMPS [225], in which we take, for generality, the fundamental units as mass m_{LJ}, distance σ_{LJ}, energy ϵ_{LJ} and the Boltzmann constant k_b. Neighbouring beads (and the patches with their host beads) are bonded with a harmonic potential given by

$$V_{\mathrm{bond}} = K_{\mathrm{bond}}(r - r_0)^2, \tag{4.1}$$

where r_0 is the equilibrium bond distance and K_{bond} is the stiffness of the harmonic bond. We set K_{bond} as $300\,\epsilon_{\mathrm{LJ}}/\sigma_{\mathrm{LJ}}^2$ throughout, only allowing for small disturbances around the equilibrium distance. We set r_0 to $0.96\,\sigma_{\mathrm{LJ}}$ for bead-bead bonds and $0.56\,\sigma_{\mathrm{LJ}}$ for the bead-patch bonds so that the patch stays on the surface of its host . The angle constraint is set similarly by a harmonic potential

$$V_{\mathrm{angle}} = K_{\mathrm{angle}}(\alpha - \alpha_0)^2, \tag{4.2}$$

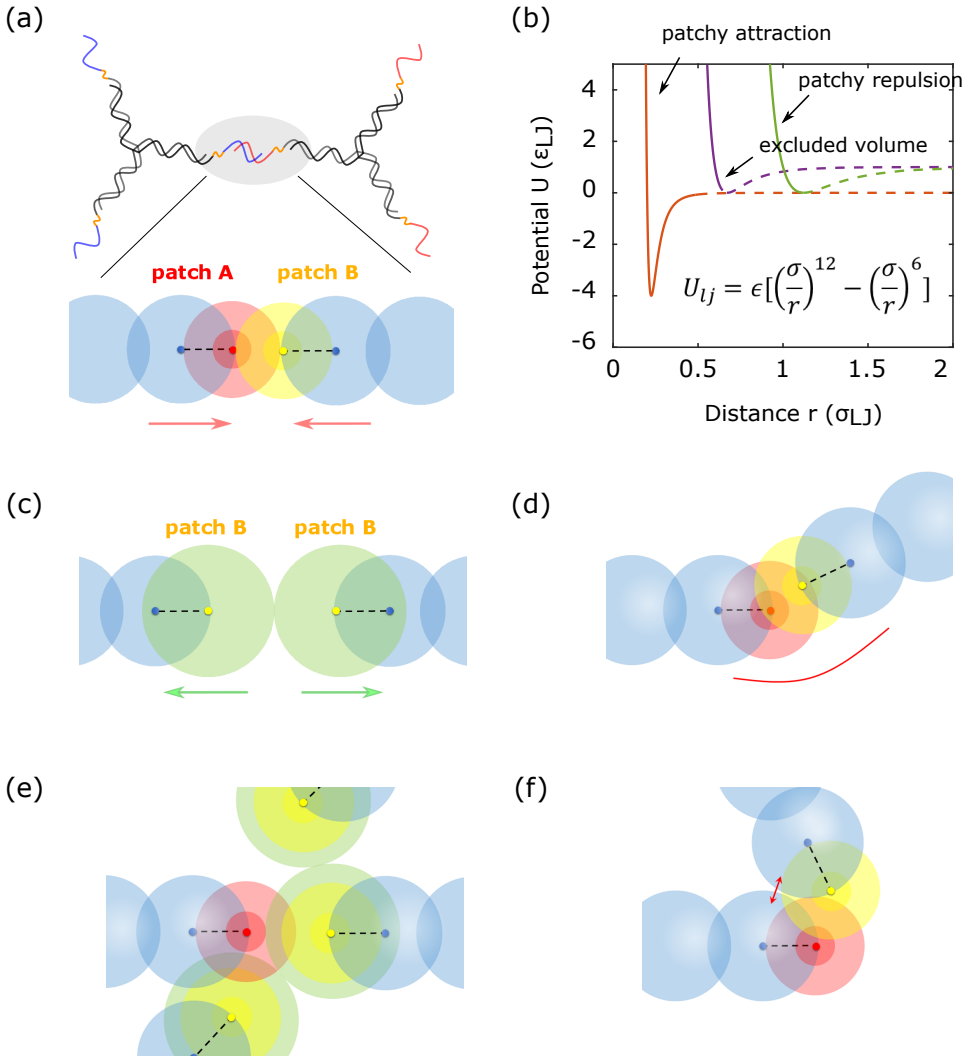

Fig. 4.2 (a) Visual description of the designed patchy interactions between patch A and patch B. (b) Pairwise potentials used in the model. (c)-(f) Illustrations of other typical cases for patch-patch interactions. (c) patch B-B attraction. (d) Bending situation. (e) A third-body repulsion. (f) A bent-angle restriction from an attractive patchy pair.

where α_0 is the equilibrium angle and K_{angle} sets the bead/patch chain rigidity. We set $\alpha_0^{\text{branch}} = 180°$ and $\alpha_0^{\text{centre}} = 120°$ to ensure the basic geometric configuration of the Y-shape, and $K_{\text{angle}} = 300\,\epsilon_{\text{LJ}}/\text{rad}^2$ to constrain the bending of the chains.

The excluded volume of the beads is defined by a Weeks-Chandler-Andersen (WCA) pair potential:

$$V_{\text{WCA}}(r,\epsilon,\sigma) = \begin{cases} 4\epsilon\left(\left(\frac{\sigma}{r}\right)^{12} - \left(\frac{\sigma}{r}\right)^{6}\right) + V' & r \leq 1.12\,\sigma \\ 0 & r > 1.12\,\sigma \end{cases} \tag{4.3}$$

where $\epsilon = \epsilon_{\text{LJ}}$ and $\sigma = \sigma_{\text{LJ}}$, and V' is set such that $V_{\text{WCA}}(r = 1.12\sigma) = 0$. The WCA potential is also used for patches of the same type to avoid attractions between non-complementary sequences and to inhibit three-patch attachment. For this purpose, the energy and distance parameters are chosen to be $\epsilon = \epsilon_{\text{LJ}}$ and $\sigma = 0.67\,\sigma_{\text{LJ}}$, and therefore the cut-off distance in Eq. 4.3 becomes $1.12\,\sigma = 0.67\,\sigma_{\text{LJ}}$ and we reset V' accordingly. The patch-patch attraction between complementary patches (i.e. the A-B interaction) is set by a Lennard-Jones (LJ) potential:

$$V_{\text{LJ}}(r,\epsilon,\sigma) = 4\epsilon\left(\left(\frac{\sigma}{r}\right)^{12} - \left(\frac{\sigma}{r}\right)^{6}\right) + V'', r \leq r_{\text{cutoff}} \tag{4.4}$$

where $\epsilon = 4\,\epsilon_{\text{LJ}}$ and $\sigma = 0.2\,\sigma_{\text{LJ}}$ and V'' is set so that $V_{\text{LJ}}(r = r_{\text{cutoff}}) = 0$. Here $r_{\text{cutoff}} = 5\,\sigma_{\text{LJ}}$, giving a long-range attraction that can mimic the ssDNA attractions between complementary sequences. The combination of WCA and LJ potentials employed in representing the patchy ends of the building block arms effectively prevents pairwise additivity of the attractions, giving each arm a strict valency of 1, Fig. 4.2(b). All the parameters were chosen empirically and tested to ensure they satisfy the geometry of the experimental model and the physical interactions.

4.2.2 Initial configurations

We first prepare initial configurations by randomly placing non-overlapping Y-shaped units into a cubic, periodic simulation box. We used a Monte Carlo algorithm: *i.* a seed Y-shape is placed in the centre of the box; *ii.* a duplicate Y-shape is generated, given a random rotation and tranlation, and is labelled as type A or B (with equal probability); *iii.* if the duplication fits in the simulation box and does not overlap with the existing units (evaluated by a cut-off distance), it is retained, otherwise, the duplication is abandoned; *iv.* run until the number of valid Y-shapes meets the pre-set number. The resulting configuration is then used as the configurational input for the following simulation. Fig. 4.3 shows examples of initial configurations. The data presented hereafter represents ensemble averages of 10 realisations.

We set the side length of the box as $30\,\sigma_{\mathrm{LJ}}$, with periodic boundary conditions. The number density is set by varying the number of the Y-shaped units between 50 and 400. The volume per Y-shaped unit is estimated as $7.3\,\sigma_{\mathrm{LJ}}^3$, calculated by the formula $V_{\mathrm{Y}} \approx (\pi r^2 \times l) \times 3$, where $r = 0.56\,\sigma_{\mathrm{LJ}}$, and $l = 2.48\,\sigma_{\mathrm{LJ}}$. We characterise the concentration based on the number density ρ as well as the approximate volume density ϕ_{vol}.

4.2.3 Simulation details

To represent the solvent environment, we perform all coarse-grained molecular dynamics simulations using Langevin dynamics, in which the trajectories of each bead are computed according to

$$m\frac{d^2\mathbf{x}}{dt^2} = -\nabla U(\mathbf{x}) - \lambda\frac{\mathbf{dx}}{\mathbf{dt}} + \eta(\mathbf{t}), \tag{4.5}$$

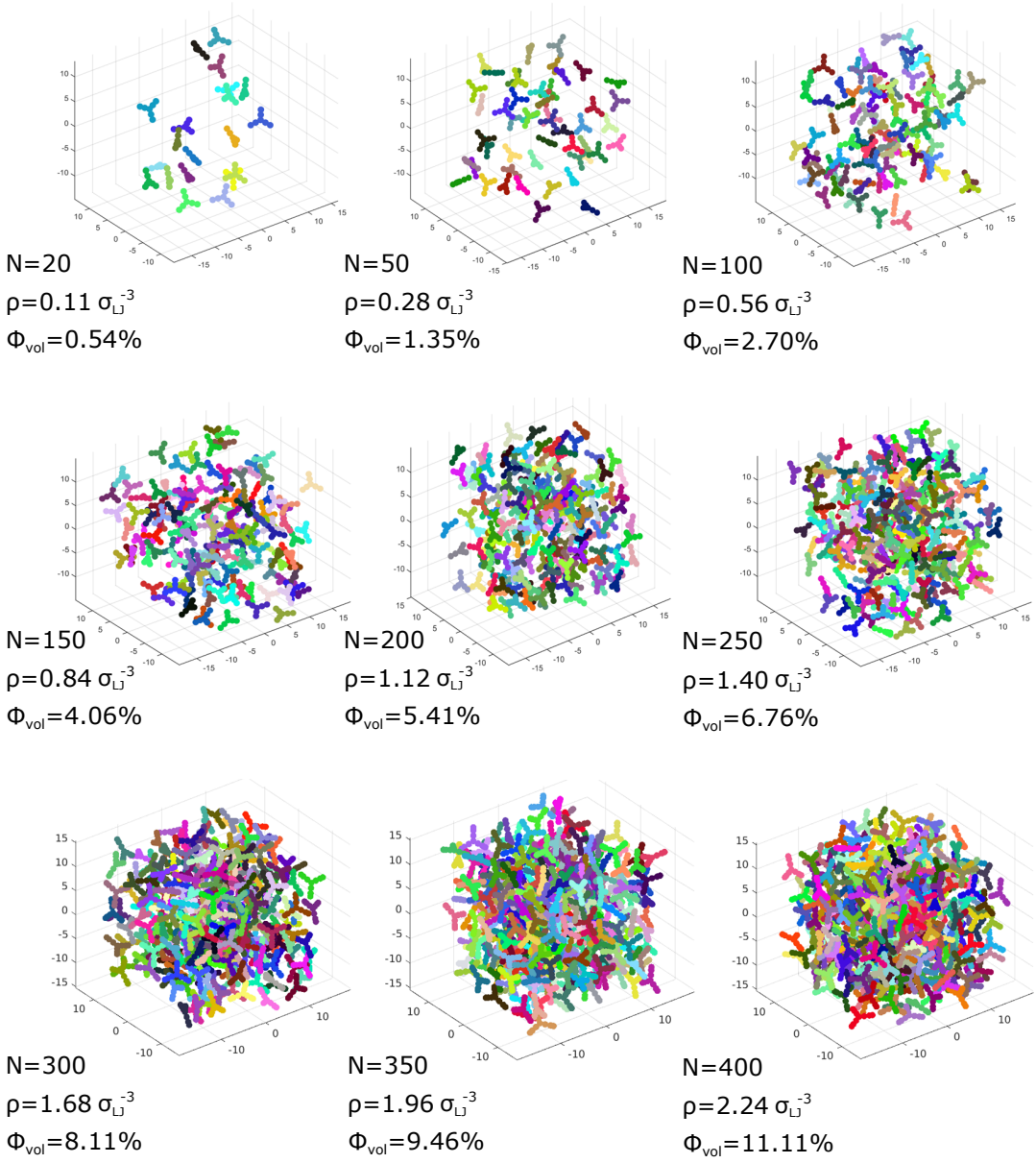

Fig. 4.3 Plots of randomly generated non-overlapping initial configurations at increasing concentrations in a $30 \times 30 \times 30\,\sigma_{\mathrm{LJ}}^3$ cubic simulation box. The corresponding 'per Y-unit' number densities and representative volume fractions are labelled on the bottom left of each panel.

where $\mathbf{x}$ and m (in units m_{LJ} as above) are the position and mass of the bead respectively. U($\mathbf{x}$) is the particle interaction potentials introduced in Section 4.2.1, and therefore $-\nabla U(\mathbf{x})$ is the applied forces correspondingly. The damping parameter λ that represents the viscosity of the solvent was set to $10\,\tau_{\mathrm{LJ}}$, where $\tau_{\mathrm{LJ}} = (m_{\mathrm{LJ}}\sigma_{\mathrm{LJ}}^2/\epsilon_{\mathrm{LJ}})^{1/2}$ is the reduced time unit. $\eta(t)$ is a noise term from interactions with a stochastic heat bath via random forces and dissipative forces. It can be written as $\eta(t) = \sqrt{2\gamma k_B T}R(t)$, where k_B is Boltzmann constant, T is the temperature (ranging from $0.05\,\epsilon_{\mathrm{LJ}}/k_b$ to $0.7\,\epsilon_{\mathrm{LJ}}/k_b$ for all the simulations), and $R(t)$ is a delta-correlated stationary Gaussian process with zero-mean. We first perform the equilibrating simulation at a fixed temperature T_{i} ($0.05\,\epsilon_{\mathrm{LJ}}/k_b \leq T_{\mathrm{i}} \leq 0.7\,\epsilon_{\mathrm{LJ}}/k_b$), starting from the initial configurations aforementioned. The numerical time step was set to 0.005 τ_{LJ}, and each of the simulations runs for $5 \times 10^4 \tau_{\mathrm{LJ}}$ to ensure that the steady state is reached. We use the number of connected patchy pairs to characterize the connectivity of the network, shown in Fig. 4.4(a). This quantity increases with time, reaching a steady state plateau whose value depends on T and the number density ρ. We define the degree of association θ to evaluate the connectivity of the network, which we define here as:

$$\theta = \frac{M}{(Q_{\mathrm{valence}} \times N)/2} \tag{4.6}$$

where M is the number of connected patchy pairs (which was evaluated by a cut-off distance between any two patches), N is the total number of Y-shaped units and Q_{valence} is the building block valency, which is 3 in our model. The denominator represents the maximum number of connected patchy pairs for a system of N units, and therefore $\theta = 0 \rightarrow 1$.

As shown in Fig. 4.4(a), we compute values of M time-averaged over the steady state period. Fig. 4.4(b) plots θ against temperature T, which we refer to hereafter as the *melting curve*. A hysteresis test is run to confirm that the systems stay in

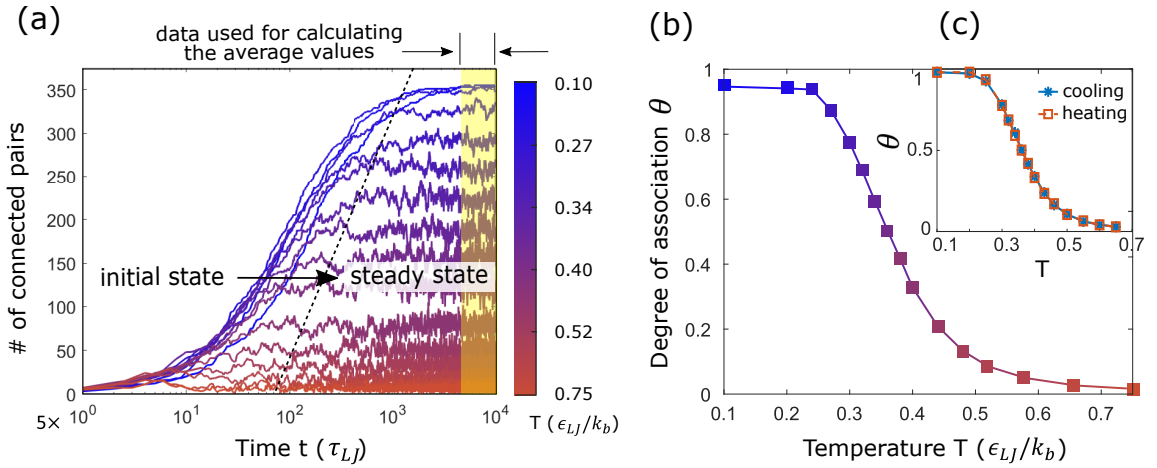

Fig. 4.4 (a) Illustration of equilibration process quantified by the number of connected pairs at temperatures from 0.1 $\rightarrow$ 0.75 $\epsilon_{\mathrm{LJ}}/k_b$. The system starts at a randomly generated non-overlapping initial state (Fig.4.3) and eventually reaches its steady state, where the number of connected pairs reaches a plateau. (b) Degree of association θ(T) calculated from the averaged number of connected pairs in Fig. 4.4(a) (masked in yellow). (c) Hysteresis test for cooling-down and heating-up ramps. All the data are taken on a system with $\rho = 1.39\,\sigma_{\mathrm{LJ}}^{-3}$ in the simulation box $= 30 \times 30 \times 30\,\sigma_{\mathrm{LJ}}^{3}$.

equilibrium after the aforesaid approach. We first take the equilibrated system at temperature T $= 0.65\,\epsilon_{\mathrm{LJ}}/k_b$ as the input configuration, and then cool it down to T $= 0.6\,\epsilon_{\mathrm{LJ}}/k_b$ until another steady state is reached. Likewise, the final steady state of the (*i-1*)-th step was chosen to be the starting point of the *i*-th step, whose steady state serves as the starting state for the step *i+1*, and so forth. Fig. 4.4(c) shows cooling and heating ramps for temperatures between $0.1\,\epsilon_{\mathrm{LJ}}/k_b$ and $0.65\,\epsilon_{\mathrm{LJ}}/k_b$. No hysteresis is observed, demonstrating the equilibrium nature of the steady state.

4.3 Results and discussions

4.3.1 DNA thermodynamics

Thermodynamic hybridization for short-stranded DNA can be described by a two-state model. We first assume that the equal-numbers of complementary ssDNA mixture

(molecules are noted as A and B) can hybridize into dsDNA (molecules noted as AB). The equilibrium constant K_a for this reaction can be written as

$$K_a = \frac{[AB]/[\varnothing]}{([A]/[\varnothing])([B]/[\varnothing])} = \exp(-\beta \Delta G^{\varnothing}), \tag{4.7}$$

where [A], [B] and [AB] refer to the concentration of ssDNA A, ssDNA B and dsDNA AB respectively. $[\varnothing]$ refers to the standard state concentration, which is 1 Molar. $\beta = 1/k_B T$, where $k_B = 1.38 \times 10^{-23} \mathrm{m^2\,kg\,s^{-2}\,K^{-1}}$ is the Boltzmann constant, and T is the temperature in Kelvin. $\Delta G^{\varnothing}$ is the standard Gibbs energy for DNA hybridization, which can be estimated using the SantaLucia thermodynamic model [24].

To transfer these values into simulation parameters, we furthermore write the DNA concentration in number density, and therefore the concentrations of A, B and AB are denoted as ρ_{A}, ρ_{B}, and ρ_{AB}, respectively. Starting with the fully disassociated state $\theta = 0$, and with an equal (by number) mixture of A and B, we write down the initial number densities as

$$\rho_{\mathrm{A}}^{\circ} = \rho_{\mathrm{B}}^{\circ} = \rho, \tag{4.8}$$

so that at a given temperature T where $\theta = \theta(\mathrm{T})$, the number densities of AB, A and B are

$$\begin{aligned} \rho_{\mathrm{AB}} &= \rho\theta \\ \rho_{\mathrm{A}} &= \rho_{\mathrm{B}} = \rho(1-\theta). \end{aligned} \tag{4.9}$$

The left-hand term in Eq. 4.7 becomes

$$K_a = \frac{\rho_{\mathrm{AB}} \rho^{\varnothing}}{\rho_{\mathrm{A}} \rho_{\mathrm{B}}} = \frac{\theta \rho^{\varnothing}}{\rho(1-\theta)^2} \tag{4.10}$$

where $\rho^{\varnothing} = 6.022 \times 10^{26} m^{-3}$ is the standard number density. With the total volume fixed at V and N the number of building blocks, the number density can be written as

$\rho = N/V$. Hence Eq. 4.10 can be written as

$$K_a = \frac{\theta}{N(1-\theta)^2} \times \rho^{\varnothing} V. \tag{4.11}$$

Substituting K_a with Eq. 4.11, Eq. 4.7 can be written as

$$\frac{\theta}{N(1-\theta)^2} \times \rho^{\varnothing} V = \exp(-\beta \Delta G^{\varnothing}), \tag{4.12}$$

where the left-hand purely relates to the number density and degrees of association, and the right-hand term is associated with the energy.Defining a new parameter

$$K_a^* = \frac{\theta}{N(1-\theta)^2}, \tag{4.13}$$

we write Eq. 4.12 as

$$K_a^* = \exp(-\beta \Delta G^{\varnothing})/\rho^{\varnothing} V. \tag{4.14}$$

For a certain ssDNA sequence, $\Delta G^{\varnothing}$ is constant [24]. At fixed temperature T and volume V, therefore, K_a^* should remain the same value at equilibrium regardless of the initial state. This allows us to test the feasibility of the simulation model by calculating Eq. 4.13 with N and θ varying.

Fig. 4.5(a) shows melting curves for systems with number densities ρ varying from 0.28 to 2.22 $\sigma_{\mathrm{LJ}}^{-3}$. Each data point $\theta(\rho, T)$ is averaged from 10 independent realisations following the equilibrating strategy described above. At low temperature $\theta \to 1$, indicating a percolating network, which we call the *gel phase*. At high temperature $\theta \to 0$, meaning all patchy pairs are disassociated, indicating a gaseous phase. A transition is shown at intermediate temperatures. It is understandable that the melting curve shifs rightwards as N increases, because $\Delta G^{\varnothing}$ includes the concentration of ssDNA and therefore influences the value of $\theta(N, T = T_i)$. According to Figs. 4.4 and 4.5(a),

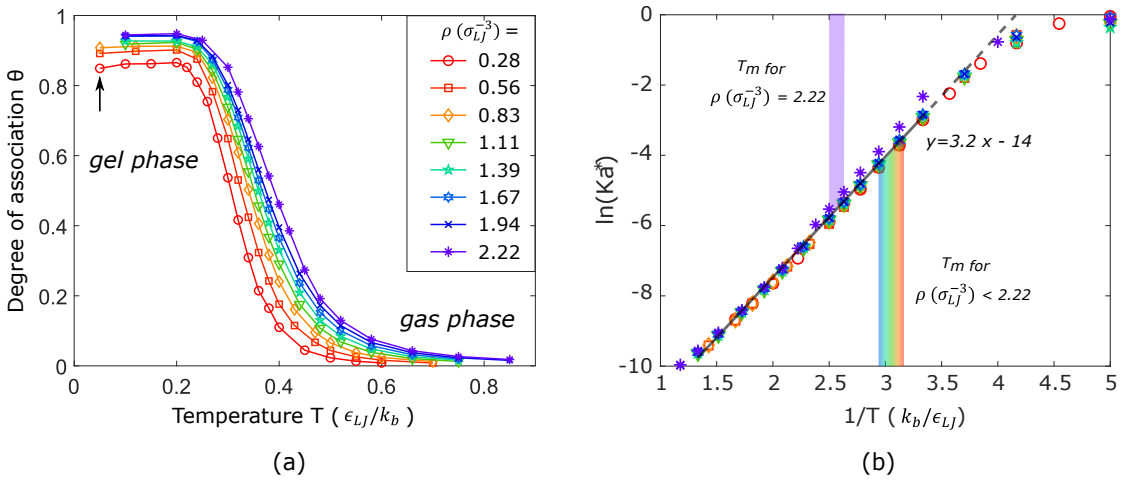

Fig. 4.5 (a) The simulation-determined melting curves for samples at number density $\rho = 0.28 \rightarrow 2.22\,\sigma_{\mathrm{LJ}}^{-3}$. (b): Arrhenius plot obtained from $\theta(T)$ as described by Eq.4.15.

θ is still slightly smaller than 1 even at $T \rightarrow 0$, meaning that not all the patches are bonded. This could be mainly due to two reasons: (i) the geometric restriction from the angular potentials and (ii) the kinetic arrest in local energy minimum region. The former can explain why the upper plateau of $\theta(T)$ increases as the total number of molecule increases: because the number of geometrically restricted pairs is more or less the same, while the total number is rising up, the effect is less significant as it is averaged by the whole system. The latter explains the dropping-down part at $T = 0.1$ in the $\rho = 0.28\,\sigma_{\mathrm{LJ}}^{-3}$ curve. As the temperature is so low, patchy pairs may form before the equilibrium state reaches. Once connected, such pairs are so strong that they require more thermal energy to break them up. When the temperature slightly goes up, the thermal energy increases so the misplaced pairs disassociate and may eventually form new pairs in their equilibrium state.

We can write Eq. 4.12 explicitly as

$$K_a^* = \exp(-\beta \Delta G^{\varnothing})/\rho^{\varnothing} V = \exp(-\frac{\Delta H}{k_B T} + \Delta S)/\rho^{\varnothing} V, \tag{4.15}$$

where $\Delta H < 0$. Neglecting small changes in ΔH and ΔS that result from varying the DNA concentration [24], we expect that $\ln(K_a^*) \sim 1/T$, Fig. 4.5(b). We find this relationship holds at high temperatures ($\theta < 0.5$), but breaks down as the percolating network is achieved ($\theta \to 1$). This is expected as Santalucia's theory only applies for free ssDNA models. In particular, for our model with three ssDNA sites geometrically constrained onto one Y-shaped body, additional structural energies and entropies should be considered. In the gas phase, the extra term from the configuration is not influential so SantaLucia's model still applies. When approaching the gel phase, though, the two-state DNA thermodynamic model should be modified. Nevertheless, our proposed simulation model fits satisfactorily with the simplified DNA thermodynamic theory and predicts melting curves consistent with expectation.

4.3.2 Structural properties

Our structural analysis of the DNA hydrogel model is guided by the radial distribution function $g(r)$ of the central beads of the Y-shaped units. The mathematical expression is described by Eq. 4.16

$$g(r) = \frac{1}{4\pi r^2 \rho N} \sum_{i=1}^{N} \sum_{j \neq i}^{N} \langle \delta(|r_{ij} - r|) \rangle, \tag{4.16}$$

where N is the total number of the central beads, and ρ is the averaged number density of the central beads across the whole system. The sum counts the total number of the central bead pairs at the distance r. We average this quantity over equilibrium configurations.

Fig. 4.6 shows a schematic of the geometry of four Y-shaped units connected in a chain. They are marked in two different colours (green and blue) indicating units with different patch types (patch A and patch B). We define the centre points of the

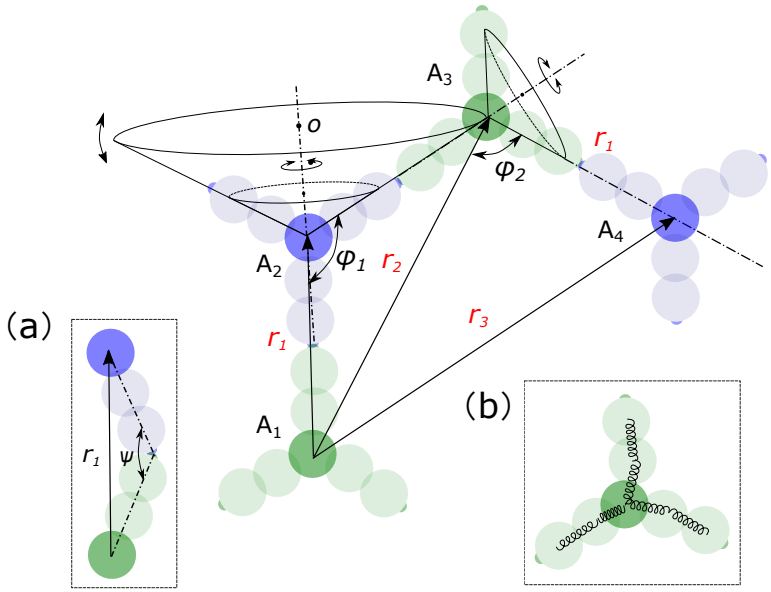

Fig. 4.6 Schematic of the typical configuration of four Y-shaped units associated in a row, drawn in blue and green respectively to indicate different patchy types. A_1, A_2, A_3 and A_4 denote the centre point of the centre beads (darker color).

central beads (darker green or darker blue) in a row as points A_1, A_2, A_3 and A_4, and the planes where the corresponding Y-shaped units stay on as planes P_1, P_2, P_3 and P_4. The sketch follows the assumptions below:

1. All the beads in one Y-shaped unit are on the same plane.

2. The arms of two connected patches are aligned along their principle axis. Fig. 4.6(a) shows the case that they are not aligned.

3. The three beads in sequence in the same arm are properly aligned. Fig. 4.6(b) shows the case where they are unaligned.

4. The plane P_{i+1} can rotate freely around the $\overline{A_iA_{i+1}}$ axis. We assume the rotation, or *dihedral* angle of plane P_i and P_{i+1}, follows a uniform distribution.

Our choice of K_{bond} and K_{angle} ensure that assumptions 1-3 are satisfied to a good approximation.

According to these assumptions, we estimate the three typical lengths marked as r_1, r_2 and r_3, which represent the distance of $\overline{A_1A_2}$, $\overline{A_2A_3}$ and $\overline{A_3A_4}$ respectively, as well as angles φ_1 and φ_2 that represent $\angle A_1A_2A_3$ and $\angle A_1A_3A_4$ (see Fig. 4.6). We calculate that $r_1 = 4.96\,\sigma_{\mathrm{LJ}}$, and $r_2 = 8.59\,\sigma_{\mathrm{LJ}}$ with φ_1 at a fixed value of 120°. Though φ_2 is unknown, if we take the uniform distribution for the rotation angle, the expectation value of r_3 can be calculated as $\approx 2.37\,r_2$, which is then $11.5\,\sigma_{\mathrm{LJ}}$. Details of the calculation are given in Appx. D.

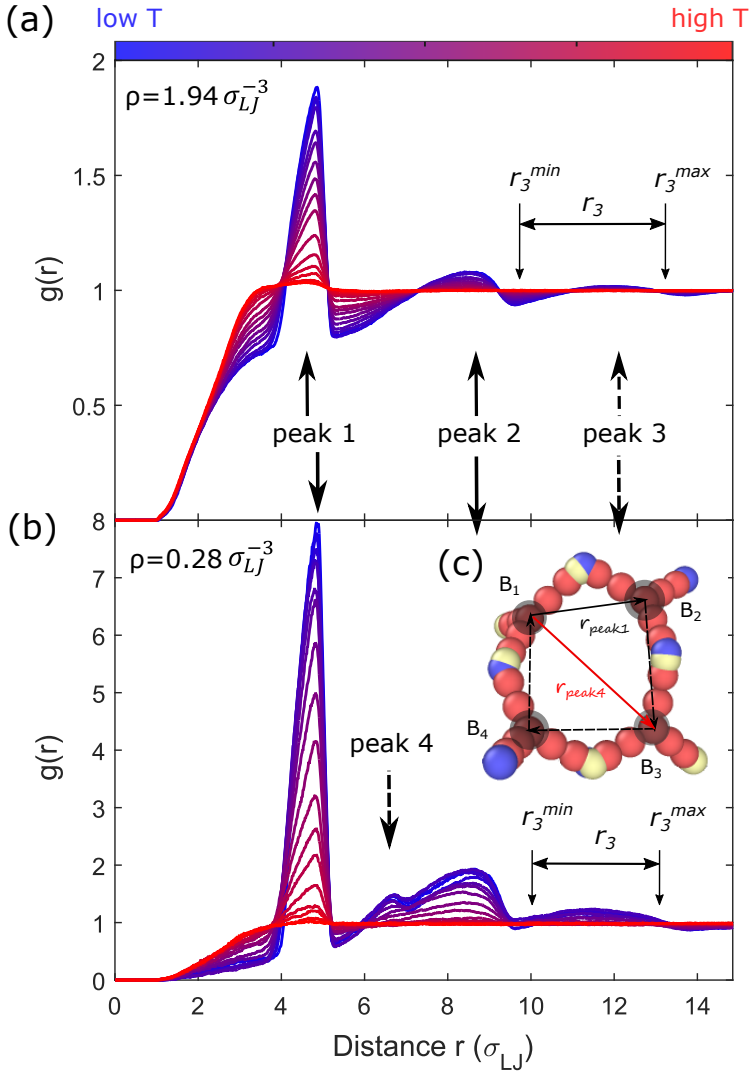

Fig. 4.7 Central-bead radial distribution function g(r) for ρ = 0.56, 0.83, 1.11, 1.39, 1.67 and $2.22\,\sigma_{\mathrm{LJ}}^{-3}$ systems at various temperatures.

We measured the radial distribution function g(r) of the central beads of the systems at various concentrations and temperatures, at the equilibrium states acquired before. All measurements were time-averaged over 10^6 configurations from the time series and then over 10 independent realisations at given (N, T), with T chosen to cover the full melting region. Fig. 4.7(a) shows the radial distribution function at $\rho = 1.94\,\sigma_{\mathrm{LJ}}^{-3}$ for across a range of T. For all the measurements, $g(r) = 0$ at $r < 1.12\,\sigma_{\mathrm{LJ}}$, which is the cut-off distance of the WCA potential applied to the central beads. At high temperature, $g(r)$ is approximately flat thereafter, showing a gaseous phase consistent with the melting temperature results. At low temperature, we obtain three peaks at distance $r_{p1} = 4.85\,\sigma_{\mathrm{LJ}}$, $r_{p2} = 8.60\,\sigma_{\mathrm{LJ}}$ and $r_{p3} = 11.84\,\sigma_{\mathrm{LJ}}$. This is in good agreement with our theoretical prediction where $\langle r_1 \rangle = 4.96\,\sigma_{\mathrm{LJ}}$, $\langle r_2 \rangle = 8.59\,\sigma_{\mathrm{LJ}}$ and $\langle r_3 \rangle = 11.76\,\sigma_{\mathrm{LJ}}$, demonstrating that in the bulk structure, the distribution of dihedral angles is roughly uniform. The minor off-set in each of the peaks is mainly due to misalignments that violate our above assumptions, as shown in Fig. 4.6(a) and (b). Accordingly, the corresponding value of φ_2 is calculated as 120.6° for $r_3 = 11.76\,\sigma_{\mathrm{LJ}}$ as above (see Eq. D.3). This shows that the basic configuration of Y-shaped units in a chain is simply not in a plane ($\varphi_2 = 90°$ or 150°), which furthermore illustrates that the system prefer to form a 3D network instead of a 2D sheet.

The results of the system at low concentration ($\rho = 0.28\,\sigma_{\mathrm{LJ}}^{-3}$, Fig. 4.7(b)) show an unexpected 4th peak between r_1 and r_2. As discussed in detail in Appx. D, r_1 is the shortest characteristic length in the system, and, assuming the planar arrangement in Fig. 4.6, r_2 is the second shortest. Why does it happen? We find that at low concentrations there is a closed ring structure formed by 4 Y-shaped units (Fig. 4.7(c)) rather than an open linear structure (Fig. 4.6). The diagonal distance $\overline{B_1 B_3}$ in the ring structure indeed matches the value of r_{p4}. The ring structure results from considerable bending from the patchy connection point between to associated arms, and is only

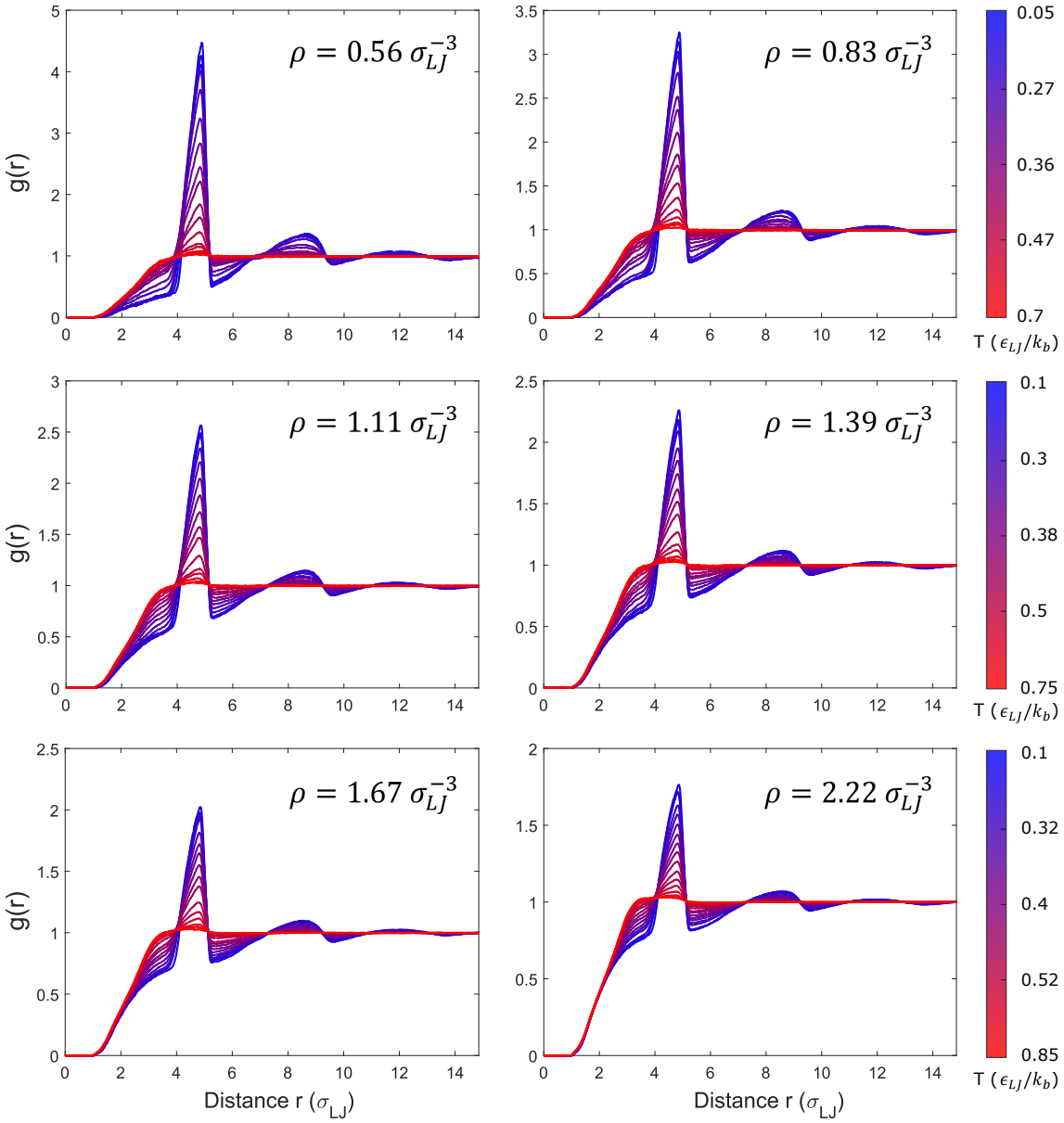

Fig. 4.8 Central-bead radial distribution function g(r) for ρ = 0.56, 0.83, 1.11, 1.39, 1.67 and 2.22 $\sigma_{\mathrm{LJ}}^{-3}$ systems at various temperatures.

observed for the very dilute case, where it is widespread. In order to form a 4-membered ring, l_1 is deviated from its most probable length, which costs extra energy; but the extra connected patchy pairs from the ring structure compensates the energy penalty.

Fig. 4.8 presents the radial distribution functions of the systems at the rest concentrations, and we can clearly see that the peak 4 is only present for $\rho = 0.28$ and $0.56\,\sigma_{\mathrm{LJ}}^{-3}$, and at higher concentration we can only observe 3 typical peaks. This indicates that at high concentrations equal to and above $\rho = 0.83\,\sigma_{\mathrm{LJ}}^{-3}$, the system is densely packed, which frustrates ring formation; and at low concentrations, there is still some empty space, so some free patches automatically detected their counterparts, and form an attractive patchy pair to reach the global energy minimum. The structural information from our model can provide as the reference for more complicated design on the building block or the patch pair connecting rules in the future.

4.3.3 Response to oscillatory shear

We explored the rheological properties of the hydrogel networks by applying shear flow (with flow in x and gradient in y) to the systems after equilibration (see Fig. 4.9) and subsequent cooling to $T = 10^{-7}\,\epsilon_{\mathrm{LJ}}/k_b$, such that thermal motion may be considered negligible. This approach gives a simplified prediction of how the overall structure responds elastically to mechanical perturbations.

A Nose-Hoover temperature thermostat accompanied with the SLLOD equation of motion [226] is employed, ensuring that the simulation is carried out in canonical ensemble at volume V and temperature T. By using the SLLOD equation of motion, we can subtract the streaming velocity of the particles caused by the re-shaping of the simulation box while shearing (Eq. 4.17) [227, 226].

$$\dot{p}_{xl} = F_{xl} - \gamma p_{yl} \tag{4.17}$$

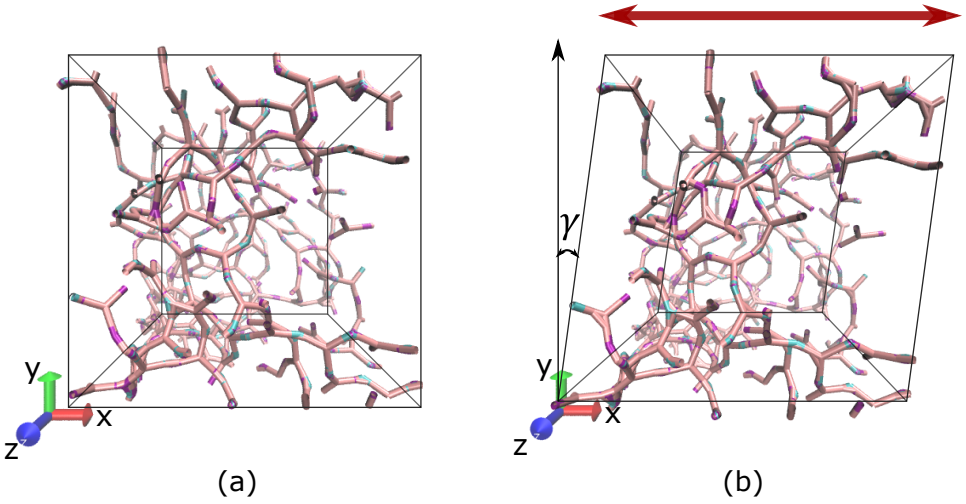

Fig. 4.9 Snapshots of fully associated system ($\theta \to 1$) (a) in the unsheared state and (b) in the sheared state.

The positions and velocities of the particles are re-mapped every $0.001\,\tau_{\mathrm{LJ}}$ for transient shear, and $0.0002\,\tau_{\mathrm{LJ}}$ for oscillatory flow to eliminate the integration errors in the latter case (Fig. E.2). To achieve oscillatory shear, we impose a time-dependent strain and rate of the strain given by Eq. 4.18

$$\begin{aligned} \gamma(t) &= \gamma_0 \sin(\omega t), \\ \dot{\gamma}(t) &= \gamma_0\, \omega \cos(\omega t), \end{aligned} \tag{4.18}$$

where γ_0 is the amplitude of the shear deformation, and ω is the shearing frequency. Assuming that we remain in the linear viscoelastic regime, the resulting shear stress (in the xy direction) can be written as:

$$\sigma(t) = \sigma_0 \sin(\omega t + \delta) \tag{4.19}$$

where σ_0 is the amplitude of the shear stress, and δ is the phase shift of the stress response due to the different contributions from elasticity and viscosity of the material

at various frequencies. The storage G'(ω) modulus can be obtained according to Eq. 4.20:

$$G' = \frac{\sigma_0}{\gamma_0} \sin(\delta) \tag{4.20}$$

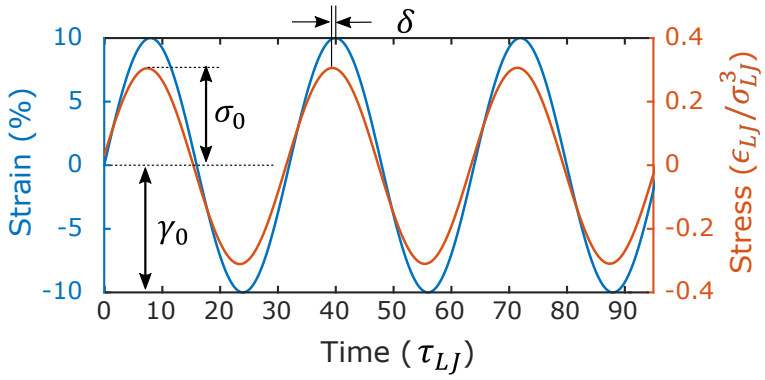

Fig. 4.10 Illustration of strain and stress time series for three cycles.

We first apply an oscillatory shear deformation with amplitude γ_0 at a fixed angular frequency ω. This deformation amplitude has been verified by running transient shear flow simulations at various shear rates (that is, $\gamma(t) = \dot{\gamma}t$, see Fig. E.1 in Appx. E.1), to ensure that the response is expected to stay linear throughout the entire shearing cycle. Then we acquire the time-series of the output shear stress $\sigma(t)$ from the simulation. The output shear stress $\sigma(t)$ shows a sinusoidal shape with a phase shift from the input shear strain as expected. The fact that δ remains very small further confirms the linearity of the shearing process taken. The example stress response is illustrated in Fig. 4.10. We average $\sigma(t)$ for every 3 cycles and then compute σ_0 and δ (Eq. 4.19), before using Eq. 4.20 to obtain G'. By changing the value of the driving oscillatory frequency ω we can plot the curves for $G'(\omega)$.

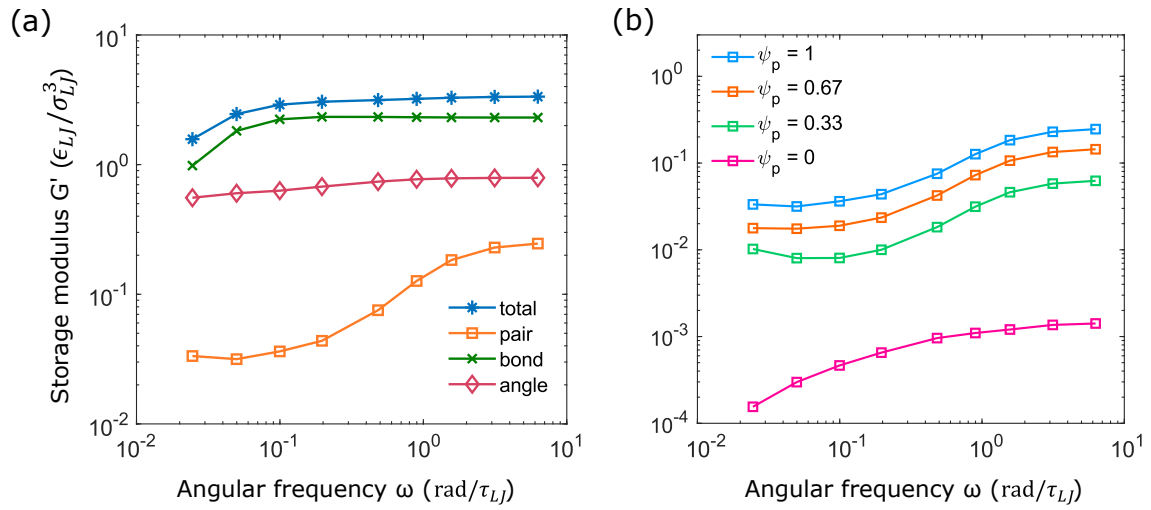

Fig. 4.11 (a) Separated pair, bond and angle contributions and the overall stress to the storage modulus $G'(\omega)$. (b) Storage modulus $G'(\omega)$ with active patches at 1, 0.67, 0.33 and 0.

Fig. 4.11(a) shows shear modulus calculated based on different potential contributions (pair, bond and angle) separately. The G'_{angle} and G'_{bond} is nearly independent to frequency ω, but the G'_{pair} is increasing with frequency ω increasing.

We also demonstrate that the pair contribution to $\sigma(t)$ is sensitive to how we design the complementarity. For example, if we change the binding rules a bit, we can achieve good control over the pair contribution to $\sigma(t)$. This shows that the chemistry of DNA hydrogels allows us to manipulate their rheology in a way that is not possible (or at least more difficult) with conventional polymeric materials (Fig. 4.11(b)).

Fig. 4.12 presents the zero-temperature storage modulus G'(ω) results taken from systems with number density of Y-shapes $\rho = 0.28$ to $2.22\,\sigma_{\text{LJ}}^{-3}$. All the data are averaged from 10 independent realisations. This shows that G' increases along with the increase of the system density, which is not surprising because the elasticity is related to the harmonic bonds in the system, and the more Y-shapes are present in the system, the higher is the elasticity. We can clearly see that at fixed angular frequency ω, the shear modulus G' increasing roughly linearly with the density of the system. The most

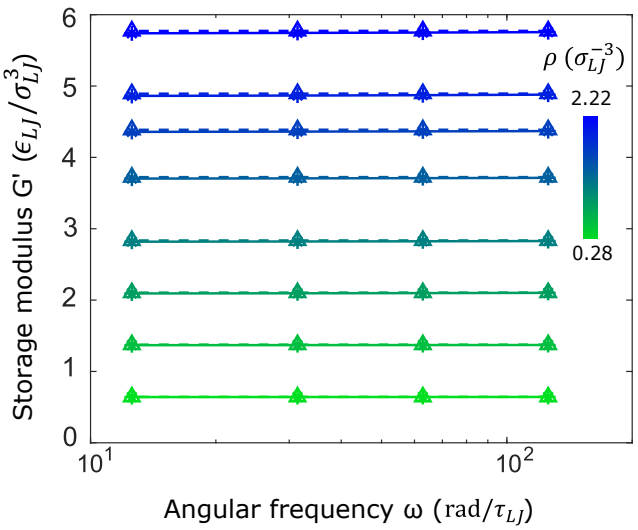

Fig. 4.12 Plot of storage modulus $G'(\omega)$ on strain amplitudes at 10% (solid lines with star markers) and 1% (dashed lines with triangle markers) respectively. Colorscale represents the number density of the system. The grey mask indicate the region where 1% strain simulations do not produce sinusoidal-shape stress response.

concentrated case where $\rho = 2.22\,\sigma_{\mathrm{LJ}}^{-3}$ is basically a scale-up of the most diluted case where $\rho = 0.28\,\sigma_{\mathrm{LJ}}^{-3}$. If we take a single spectrum into consideration, it is clear that the G' goes up as we increase the angular frequencies, but they increase more and more slowly. In low concentration systems, the G' reaches a plateau eventually, but this flattening is not so obvious for high concentration systems, as the value of G' only stays steady at angular frequencies higher than $1\,\mathrm{rad}/\tau_{\mathrm{LJ}}$. It is curious to think where the dissipation of the system comes from as the temperature is almost switched off, and there is supposed to be no energy lost in a pure harmonic system.

4.4 Conclusion

We have introduced a coarse-grained model for a binary DNA hydrogel system, whose building block is a rigid double-stranded Y-shape body patchy ends. We demonstrated that the melting behaviour of the model matches a simplified DNA thermodynamic

theory well, in particular before percolation. We also studied the structural properties predicted by the model at various concentration and temperature, proving that the three dimensional structure of the system largely conforms to a uniform distribution of dihedral angles. Last, we conducted a rheological study by applying oscillatory shear flow to the system. The storage modulus results show the elasticity of the system when fully connected, but due to the zero-temperature condition, all the frictional interactions are switched off and the loss modulus is actually not reliable (so we didn't show). This is the limitation of the model, which we hope to resolve in the future. For example, we could calculate the centre-of-mass stress instead of per-atom stress, and the former should be able to screen out the intra-molecular interactions and therefore amplify the inter-molecular interactions mainly caused by the ssDNA sticky end (which is patchy interaction here in the simulation). The results presented so far are quite expected (not sure good or bad), which demonstrated the validity of the model.

Furthermore, our model is computationally efficient compared to current DNA simulation models [131–133] as we neglect the base-wise specificity and take the whole sticky end as an interacting element with a generic, yet highly tunable. This is preferable for predicting the structural and dynamics properties of larger scale DNA self-assembly systems with repeating units/building blocks, which is normally very costly if the per-nucleotide interaction is considered. The key parameters for the building blocks (i.e. angles, bonds, geometry, etc.) can be optimized by matching with lower-level coarse-grain simulations such as OxDNA model provide quantitative predicts for real materials. Hence, this model can be used in the design of DNA networks with more interesting viscoelastic properties in the future.

4.5 Acknowledgement

I would like to thank Dr. Christopher Ness for helping with implementing the simulation, and further discussions throughout the whole work; Jiangbin Zhang for writing the Matlab script of randomly generated initial configurations; Clara Wanjura for making the uniform distribution calculation; and Dr. Aleks Reinhardt for useful discussion on patchy particles and DNA melting; Prof. Daan Frenkel and Dr. Erika Eiser for supervising.

Chapter 5

A numerical study on three-armed DNA structures

We have applied three-armed DNA nano-stars to construct large-scaled DNA complexes or hydrogels in previous chapters. As the simplest branched DNA molecule, the three-armed DNA is relatively easy to design and understand. We know *a priori* that the rigidity and configuration of the building block would affect the mechanical and structural properties of the overall system, so a careful study on the physical behaviours and 3D structures of individual building blocks is needed. Current experimental techniques cannot resolve the motion of such DNA structures on base-pair level; therefore, numerical tools emerge as the preferable optional. In this chapter, we employ the oxDNA model - a coarse-grained DNA model originated from Oxford to study the detailed structural behaviours of three-armed DNA building block individually. We aim at gaining deeper physical insight on these systems and accumulate the dataset describing their topological features, which may contribute to the refinement of the DNA computational model at higher coarse-graining levels, and eventually facilitate the design of functional DNA hydrogels.

5.1 Introduction

In the last chapter, we have established a coarse-grained model on DNA hydrogels formed by Y-shaped DNA building blocks with adhesive overhangs (i.e. ssDNA sticky ends), with particular focus on the structural and mechanical properties of the network system in bulk. However, the design of each individual building block is rather idealised and the parameters are simplified. For example, we assume that the Y-shaped DNA stays in a flat plane, which may not be the case in reality. Moreover, we did not define the twist angle between two connected Y-shapes, which means they can twist around the principal axis freely. This assumption can represent the case where a 'flexible joint' is present between the dsDNA arm and ssDNA sticky end, but may not apply for the situations when arms are directly connected. A *direct connection* here means the sticky ends are directly connected to the dsDNA arms without the inert flexible joint in between. In this case, two complementary sticky ends forming a dsDNA will lead to a twist angle that depend on the length of the sticky ends (normally ~ 10 bps for a full turn). Fig. 5.1 presents the simplified version and other possibilities for the topological features of individual Y-shapes and two associated Y-shapes. But there are far more possible structures than that of a single design of a Y-shape.

Though coarse-grained in the bulk model, these topological features are relevant for capturing the physical properties of the large scale assembly. Taking the twist angle as an example, whether it is defined matters for the randomness of the network structure. As a demonstration, Fig. 5.3 shows three typical resulting larger-scale structures assembled by the laser-cut plastic Y-shaped units that are connected via yellow rubber tubes (Fig. 5.2). It has also been demonstrated in Chapter 3 that building blocks without flexible joints form a stiffer gel comparing to the ones with flexible linkers.

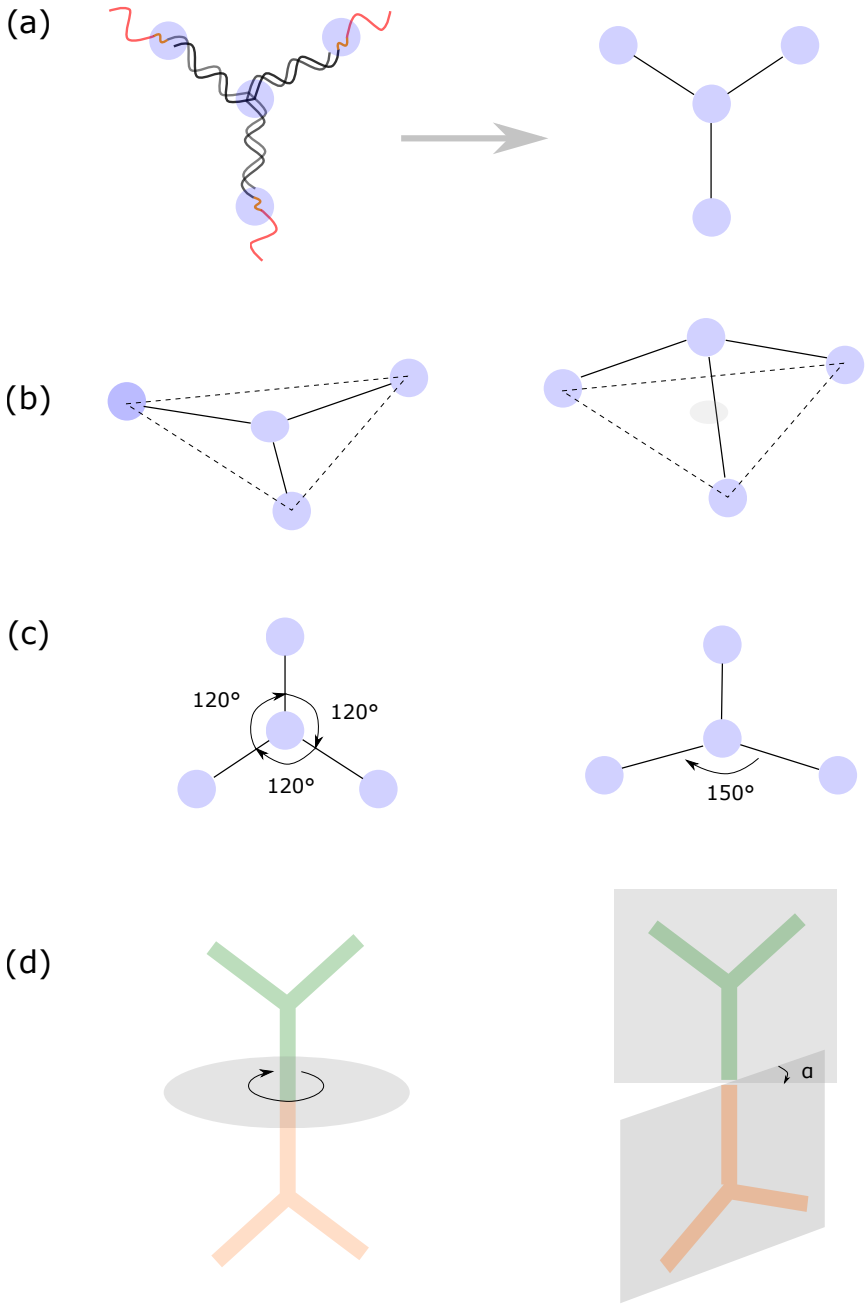

Fig. 5.1 Schematic illustrations of the idealised topological behaviours of the Y-shaped DNA (left column) and the possible other situations (right column). **(a)** The simplified representation of an individual Y-shape. **(b)** The comparison of the Y-shape in a plane and not-in-the-plane. **(c)** The comparison of the Y-shape with equal angles between neighbouring arms and unequal angles. **(d)** Two Y-shapes connected with a free twist and a fixed twist angle at α.

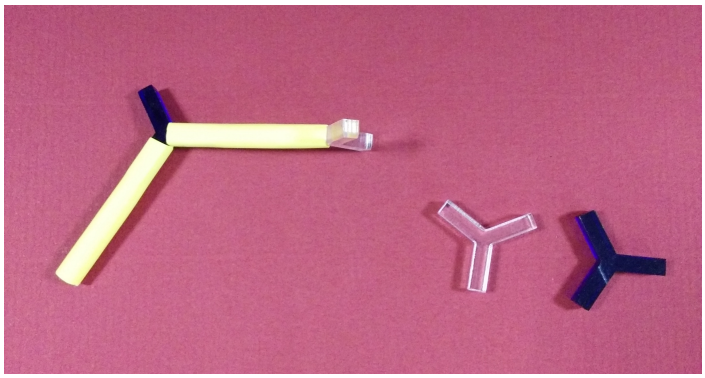

Fig. 5.2 Snapshot of the macroscopic Y-shaped units. The blue and white ones represent the Y-shaped DNA with complementary sticky ends. The yellow rubber tube represents the hybridised sticky-end connection. The connected blue and transparent Y-shaped units show a twist angle at 90°.

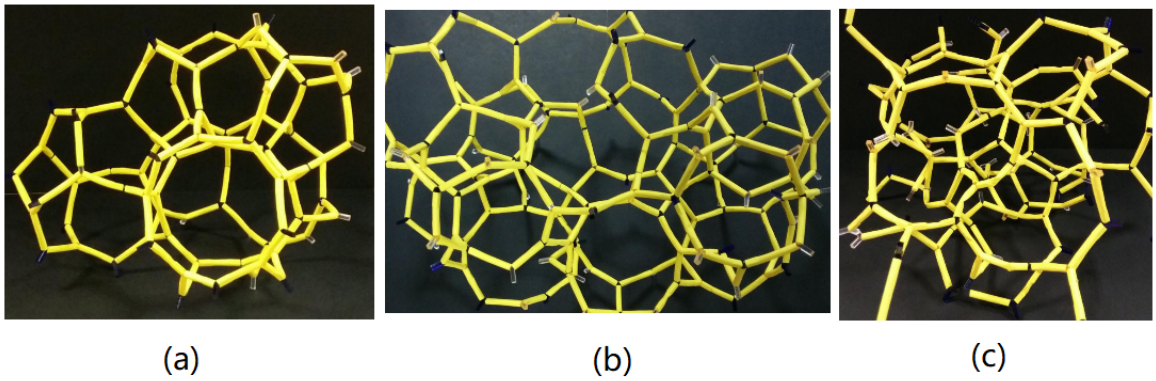

Fig. 5.3 Macroscopic models of DNA hydrogels. **(a)** Highly-ordered 3D structure with strictly-defined twist angle at 90°. **(b)** Less ordered 3D structure with the twist angle roughly at 90°. **(c)** Random 3D structure with the twist angle undefined.

The topological features of an individual DNA building block rely on the design of the ssDNAs and the specific nucleotides placed in the sequence. Therefore, a simulation model with details down to the per-base level is preferable. Here we choose a well-established DNA computional model, oxDNA2, to conduct such a simulation. Modified based on the previous two generations (oxDNA1 and oxDNA1.5), the third generation of oxDNA model (oxDNA2) has taken the sequence specificity and various stacking interactions into consideration, resulting in a spontaneous sequence-specified hybridization process and a double-helical structure with minor and major grooves

presented. This level of details allows us to mimic the topological behaviour of an individual DNA nano-star as close as possible to the reality, and gain a deeper physical insight into the sequence-dependent effects.

In this chapter, we first introduce the three-armed DNA system and the simulation details of oxDNA2, followed by the data analysis strategy. Then we compare the melting curves of these three-armed systems taken from experiments and simulations to verify the validity of the simulation model. Structural behaviour of an individual building block is studied, mainly focusing on the planarity and angle orientation, which play a significant role on the orderliness and rigidity of the constructed larger systems. We also try to tune the structural and mechanical properties of the building block by adding inert bases in the centre core, which may introduce extra flexibility for the three correlated arms. Furthermore, we looked at the two three-armed DNA connected through the hybridisation of the complementary sticky ends, and measured the bending angle and the twist angle of the two Y-shapes and modified sticky ends accordingly. We conclude that the parameters obtained from this simulation may provide the database for further details of the physical models of DNA hydrogel systems.

5.2 Models and methods

5.2.1 The original system

We choose the Y-shaped DNA building blocks taken from the DNA hydrogel system in Ref. [224] as the starting point, with slight modifications applied later in this simulation. This DNA hydrogel is a binary system with only two types of Y-shaped DNA nano-stars, whose sticky ends are complementary so that different types can bind together via DNA hybridisation. But the dsDNA arms of all the nano-stars are formed by the same sequences. Fig. 5.4 shows the DNA sequences of these two Y-shaped DNA

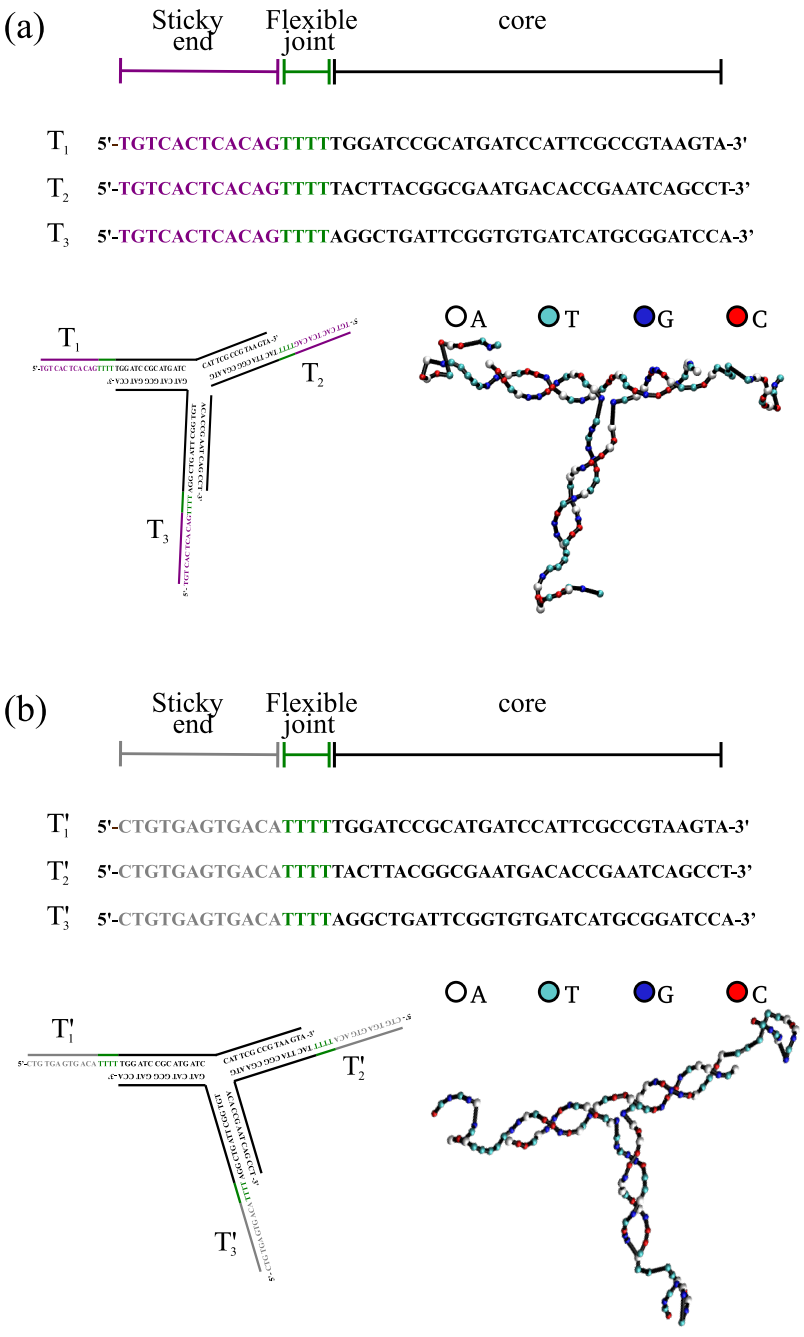

Fig. 5.4 Sequences and simulation snapshots for **(a)** *T-DNA* and **(b)** *T'-DNA*.

nano-stars (called *T-DNA* and *T'-DNA* respectively), each of which is constructed by three partially complementary single-stranded (ss) oligonucleotides (named as T_1, T_2, and T_3 for *T-DNA* and T'_1, T'_2, and T'_3 for *T'-DNA*). A single oligonucleotide is 46 bases long, with three main functional sections: (i) the main core (30 bases long) that forms the dsDNA arms (15-bases for each arm); (ii) the sticky ends (12 bases long) that is used for crosslinking other Y-shapes; (ii) the free joint (4 bases long) that bridges the main core and the sticky end, providing flexibility between two building blocks in conjunction.

5.2.2 Simulation model

We apply oxDNA 2 implemented in LAMMPS [118] to characterise basic thermodynamics, structural and mechanical properties of T-DNA and T'-DNA systems and their variants. In this model, a DNA strand is described as a polymer chain consisting of a sequence of oligonucleotide beads with three interaction sites on each bead to represent the effective interactions between the nucleotides. The potential of the model is given in Ref. [155] as follows:

$$V_{\mathrm{oxDNA2}} = \sum_{\text{nearest neighbours}} (V^*_{\mathrm{backbone}} + V^*_{\mathrm{stack}} + V'_{\mathrm{exc}}) + \sum_{\text{other pairs}} (V_{\mathrm{HB}} + V_{\text{cross stack}} + V_{\mathrm{exc}} + V^*_{\text{coax stack}} + V^*_{\mathrm{DH}}). \tag{5.1}$$

The first summation term on the right-hand-side considers only the interactions between nearest neighbouring nucleotides, i.e. two adjacent beads in a chain, while the second term represents potentials between other surrounding pairs, which are not connected through covalent bonds. In the nearest-neighbour term, V^*_{backbone} is the connectivity potential, V^*_{stack} are the favourable stacking interactions, and V'_{exc} is the excluded volume term between two consecutive nucleotides in a chain. In the second term

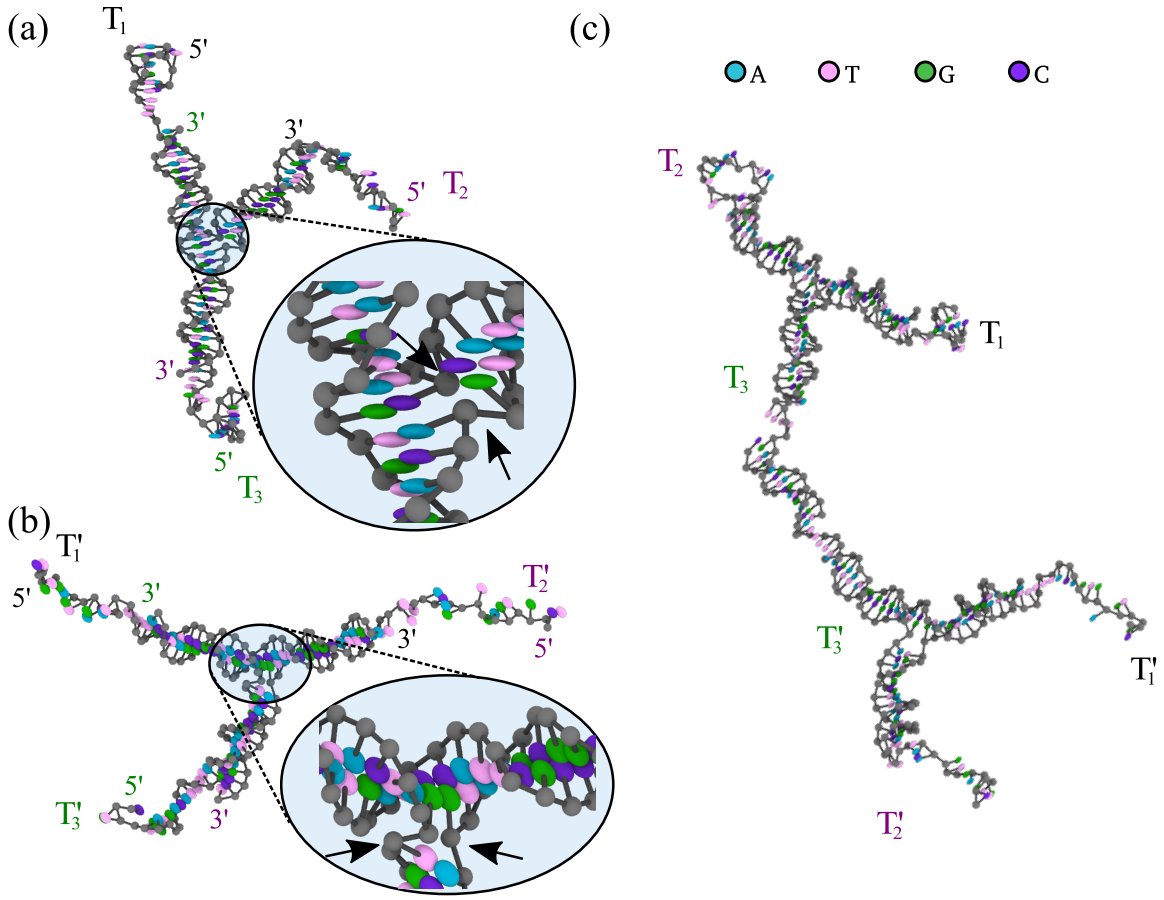

Fig. 5.5 Snapshots from the equilibrated simulations displaying the fully hybridised **(a)** *T-DNA*, **(b)** *T'-DNA* and **(c)** *T-T'-DNA* conjunction. The grey beads are representing the phosphate sites and the colourful ellipsoids representing bases following a colour scheme that blue corresponds to A, pink to T, green to G and purple to C.

with non-adjacent potentials, V_{HB} and V_{DH} stand for hydrogen bonding between the complementary bases and the Debye-Hückel form for screened electrostatic interactions, respectively; other terms are $V_{\mathrm{cross\ stack}}$, V_{exc}, and $V^{*}_{\mathrm{coax\ stack}}$, corresponding to cross-stacking, excluded volume and coaxial stacking between two non-nearest neighbours. In oxDNA 2, the hydrogen bonding and stacking parameters have been modified compared to its previous version, ensuring a closer agreement to experimental duplex melting temperatures and molecular structures. We refer to Ref. [155, 156] for all the detailed discussions on the potential formulas and the parameter settings applied to the model.

Using the current version of oxDNA model, we are able to investigate the salt-dependent flexibility of single strands and DNA thermodynamics accurately. This perfectly fits our goal of studying the sequence-related microscopic behaviours of *T-DNA* and *T'-DNA* in salt conditions, and to capture the topological features that might occur experimentally. Fig. 5.5 (a) - (b) present the snapshots of fully hybridized *T-DNA* and *T'-DNA* individuals respectively, and Fig. 5.5 (c) shows the schematic of a *T-DNA* and a *T'-DNA* connected through sticky-end hybridisation.

5.2.3 Systems with modifications

In the current *T-DNA* and *T'-DNA* systems, the centre point is tightly twisted by three oligonucleotides, against their preferable double-helical structure. Therefore, a *kink* caused by the central stress sometimes occurs in the centre core, as is shown in Fig. 5.5**(a)-(b)**. Here we would like to investigate how the system is affected when additional nucleotides are added in the central core of the molecules taking *T'-DNA* as an example. These nucleotides in the centre are designed to be *inert*, which means they are not responsible for any hydrogen bindings. The inert bases are added in the middle of the core segment (see Fig. 5.4) of different oligonucletides in *T'-DNA* (i.e.

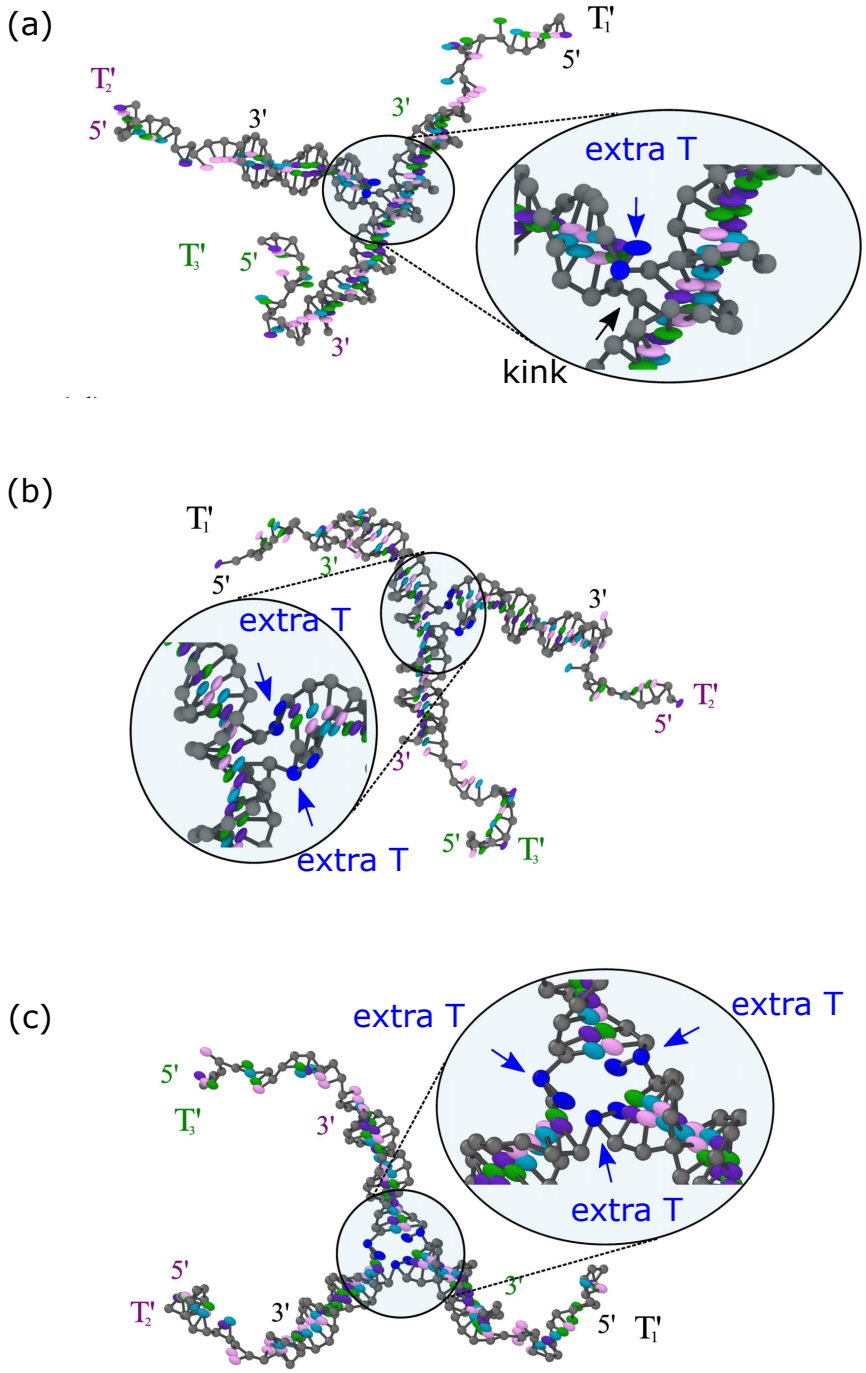

Fig. 5.6 Simulation snapshots of the molecules with inert bases added in the centre core illustrated in *T'-DNA*. **(a)** *T'$_{1T}$-DNA*: one inert thymine base in T'_1. **(b)** *T'$_{2T}$-DNA*: two thymine bases in T'_1 and T'_2 each. **(b)** *T'$_{3T}$-DNA*: three thymine bases in T'_1, T'_2 and T'_3 each. Blue arrows point at the additional thymine bases. Black arrow points at the kink structure in the twisting core.

T'_1, T'_2 and T'_3), as is shown in Fig. 5.6, and they are named as *T'$_{1T}$-DNA*, *T'$_{2T}$-DNA* and *T'$_{3T}$-DNA*.

5.2.4 Simulation details

We perform molecular dynamic (MD) simulations employing the LAMMPS implementation of oxDNA2 model [118]. All the simulations were conducted in dimensionless *lj* units, i.e. all quantities are unitless, but they can be later converted into physical units according to the relationship listed in Ref. [228]. In the following texts, all symbols with footnote 'LJ' stand for simulation units. To obtain the assembled *T-DNA* (or *T'-DNA*) structure, we first generate the input data file of three separate oligonucleotides (e.g. *T'*$_1$, *T'*$_2$ and *T'*$_3$; Fig. 5.7) using Python scripts, and then conduct the MD simulation to equilibrate them at the temperature $T = 0.1$ (simulation unit). The numerical time step was set to 0.01 τ_{LJ}, and the equilibration process runs for 5×10^8 steps long to ensure the equilibrium state is reached.

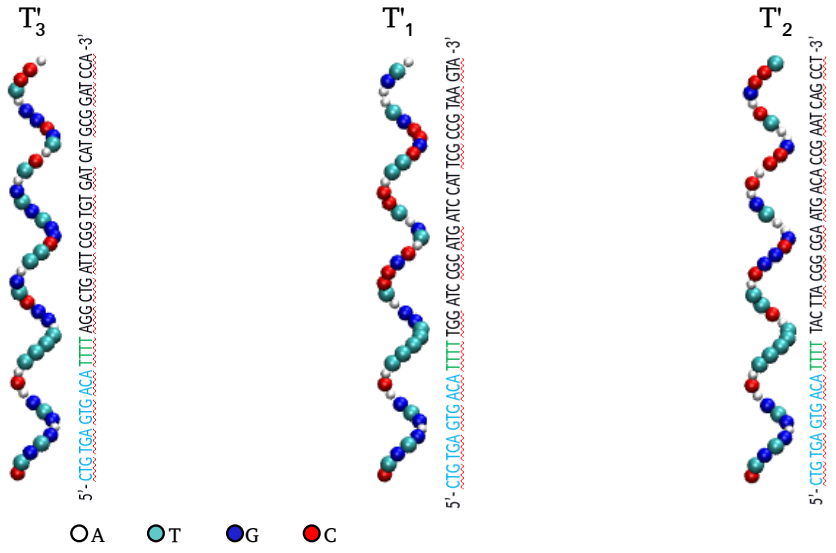

Fig. 5.7 Schematics of three oligonucleotides T'_1, T'_2 and T'_3 before equilibration.

To obtain the melting curves, we run the equilibration simulation at a fixed temperature, T_i, until the fraction of denatured base pairs, $\Phi(T_i)$, does not evolve with time after a long period. Then we generate the plot of $\Phi(T_i)$ against temperature T_i, which is the so-called *melting curve*. All the data presented hereafter were averaged from 10 independent realizations.

5.2.5 Data analysis

We take the configurations of the fully assembled Y-shaped DNA at equilibrium for further analysis to study the geometric features of the system, with the emphasis on the angle profile between two neighbouring dsDNA arms and the planarity of a single Y-shape.

To acquire the angle profile, we first need to define the vector that represent each dsDNA arm (called 'arm vector' in the later context). Ideally, we would like to take the centre of mass (COM) of the whole Y-shape as the starting point of each arm vector, and the centre of the last base-pair on each branch as the ending point correspondingly (Fig. 5.8(a)). However, due to the fluctuation of the ssDNA overhangs and occasional occurrence of denaturation of the central core, it is difficult to extract an unambiguous COM as it always deviates from the geometric centre of the core with time. Therefore, for the sake of simplicity and accuracy, we re-define the starting point of the arm vector and choose the centre of mass of the most inner non-denatured base-pairs on each arm instead. We call this version of COM as 'COM3'. Note that there is always an offset between COM3 and the COM of the Y-shape at a given time, unless the Y-shaped structure is fully hybridised and the arms and overhangs are nicely stretched. Fig. 5.8(a) shows the schematic of the three arm vectors ($\mathbf{a}_1$, $\mathbf{a}_2$ and $\mathbf{a}_3$) in one Y-shaped DNA.

To characterise the planarity of the individual Y-shape, we introduce a parameter d_p ($d_p \in [0, 1]$), which is the normalised distance from COM3 to the plane defined

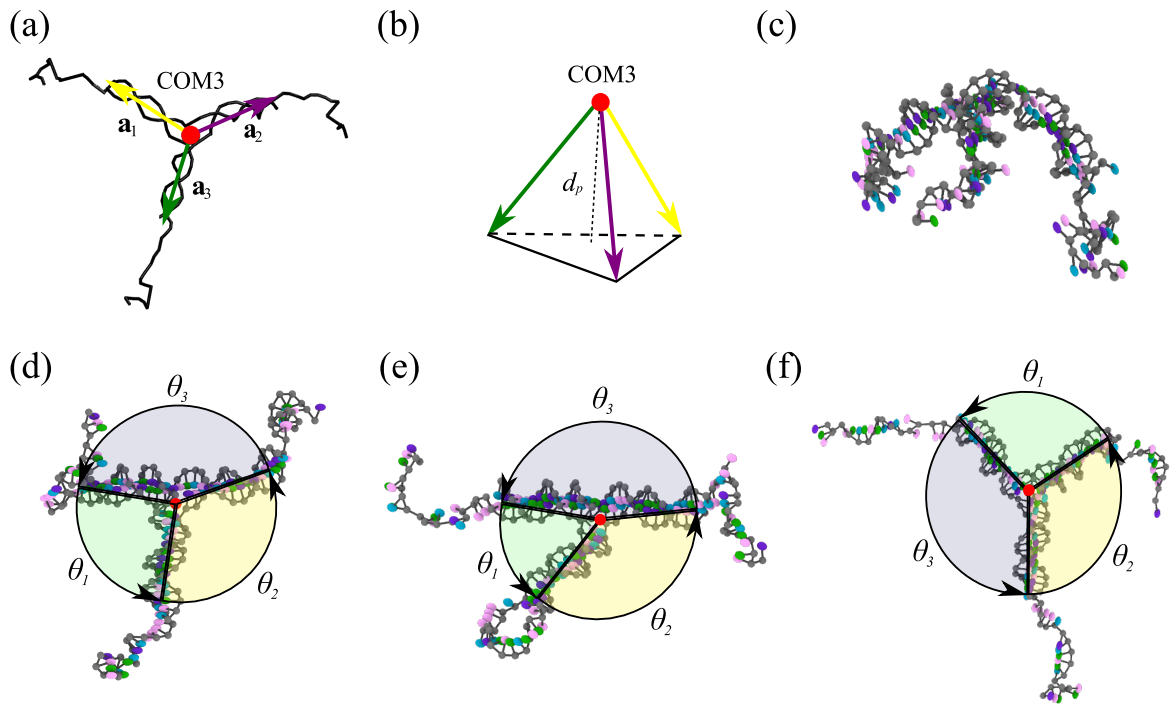

Fig. 5.8 (a) Schematic representation of the arm vector $\mathbf{a}_i$ in a single molecule. **(b)** Sketch of the planarity parameter d_p. d_p represents the distance between COM3 and the plane touching the ends of the arms. (**c**) Example of a non-planar molecule with $d_p = 0.5$. **(d)-(f)** Illustrations of planar molecules with different shapes: T-shape, T-like-shape and Y-shape respectively. The angles between two different vectors $\mathbf{a}_i$: θ_1, θ_2 and θ_3 are also shown. They are labelled according to their magnitude, with $\theta_3 > \theta_2 > \theta_1$.

by the ending points of $\mathbf{a}_1$, $\mathbf{a}_2$ and $\mathbf{a}_3$ (see Fig. 5.8**(b)**). When $d_p = 0$, the Y-shaped structure is perfectly planar. As the value of d_p increases, the planarity level of the structure is lowered accordingly, but still retains the planar features within a certain range. In the following text, we will refer to a Y-shape structure whose $d_p \leq 0.175$ as a *planar system* and otherwise a *non-planar system*. For the sake of relevance to our work, we shall only discuss the planar systems here.

We classify the molecules into three categories by the relative orientation of their arms, which is characterised by the angles between dsDNA arms θ_k (k = 1, 2, 3). The

value of θ_i is computed using Eq. 5.2:

$$\theta_k = \cos(\mathbf{a}_i \cdot \mathbf{a}_j), \quad i \neq j, \tag{5.2}$$

where i, j = 1, 2, or 3. We sort θ_k in ascending order of the values as θ_1, θ_2 and θ_3. Fig. 5.8**(d)** - **(f)** illustrate three typical behaviours of the molecule with the angle analysis performed. In Fig. 5.8**(d)**, the structure exhibits the relative orientations with $\theta_3 \approx 180^\circ$, and $\theta_1 \approx \theta_2 \approx 90^\circ$, which we categorise as *Type-I*. We allow fluctuations of the angles so $\theta_3 \in [160^\circ, 220^\circ]$, while θ_2 and $\theta_1 \in [60^\circ, 120^\circ]$ for *Type-I*. The structure in Fig. 5.8**(e)** presents the angular parameters that $\theta_3 \approx 180^\circ$, $\theta_2 > 120^\circ$ and $\theta_1 < 60^\circ$, which goes into the second category called *Type-II*. Finally, the most common structure is *Type-III*, which is characterised by $\theta_3 < 160^\circ$ as is shown in fig.5.8**(f)**.

5.3 Results and discussion

5.3.1 Melting curves

First, we measured the melting curves of *T-DNA*, *T'-DNA* and the modified *T'-DNA* systems at the NaCl concentration of 200 mM taken by the simulation (Fig. 5.9**(a)**). From Fig. 5.9**(a)**, we see that there is no significant change between the melting curves of different variants, which indicates that the melting behaviour is mainly dominated by the hybridised base pairs only, and the energy penalty introduced by the unfavourable twist does little influence. The computationally estimated melting transition is 45 $\sim$ 54°C, and the melting temperature calculated from simulation $T_m^{sim} \approx 50$°C.

Fig. 5.9**(b)** presents the experimentally acquired melting curves of *T'-DNA*, *T'$_{1T}$-DNA* and *T'$_{3T}$-DNA* at [NaCl] = 200 mM. The melting curves are merged together showing that there is no observable difference in DNA thermodynamics due to the

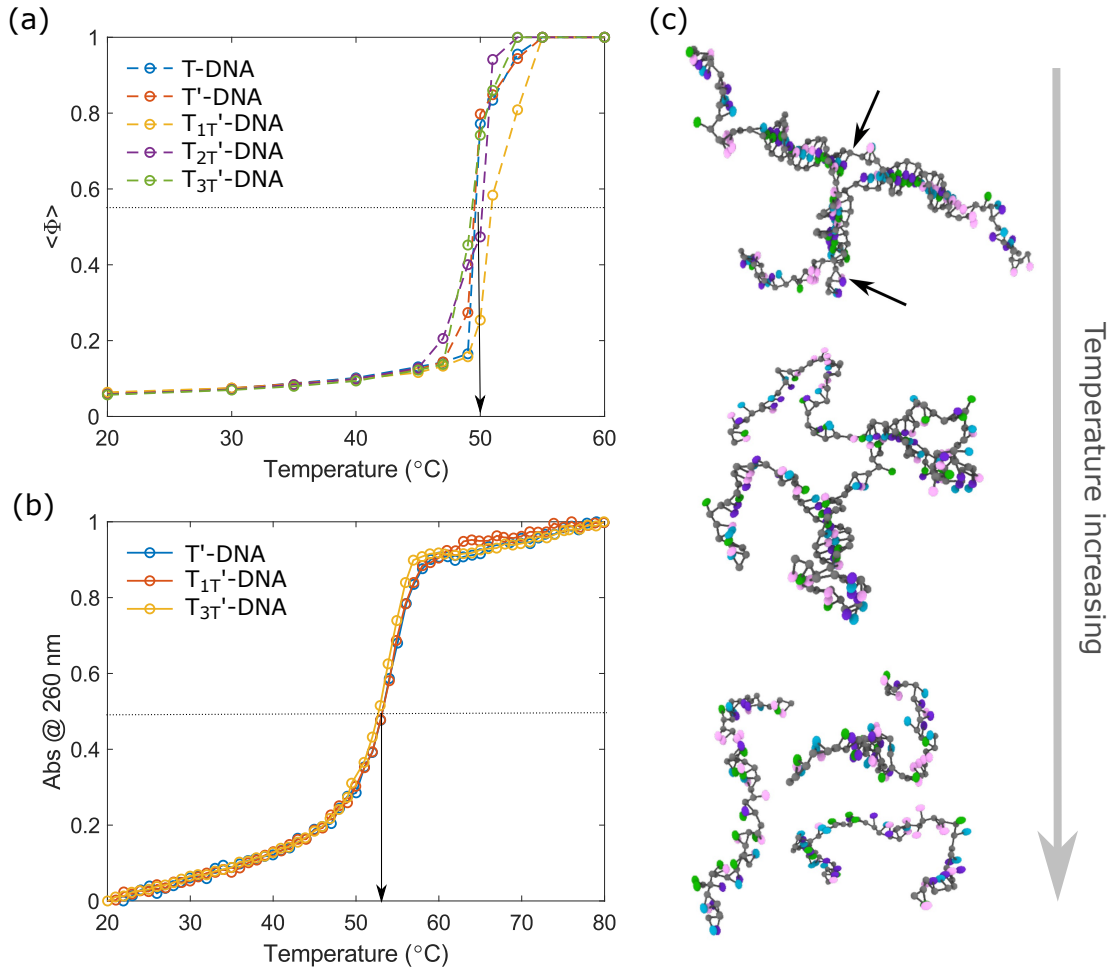

Fig. 5.9 (a) The melting curves (fraction of denaturated bp ϕ, as a function of the temperature) obtained via BD simulations of the same molecules (averaged over 10 replicas and $10^5\tau_{LJ}$). (**b**) The melting curves (absorbance at 260 nm as a function of the temperature) of *T'-DNA*, *T'$_{1T}$-DNA* and *T'$_{3T}$-DNA* obtained from experiments. **(c)** Snapshots of typical configurations at $T = 40$, 50 and 60° respectively. The arrows show the denaturation regions starting at the core of the molecule and at the end of one arm.

introduction of inert bases in the middle core. Also, the experimentally acquired melting transition is 48 $\sim$ 58°C, and $T_m^{exp} \approx 52$°C, which is quantitative close to the simulation prediction. However, in the lower temperature region ($T_m \leqslant 48$°C), the simulation curves are flattened down while the experimental curves are still decaying. This might be due to the effect of the ssDNA overhangs that do not contribute to

form the dsDNA cores, whose effect have not been considered by oxDNA2 but were demonstrated to affect the melting transition of it [23].

The good agreement of melting curves of *T-DNA*, *T'-DNA* and its variants between simulations and experiments successfully demonstrated the reliability of the simulation model for the systems of our interest. Fig. 5.9**(c)** shows the simulation snapshots of a Y-shaped molecule denature as the temperature increases.

5.3.2 Structural behaviors

We also studied the structural behaviour of *T-DNA* characterised by the planarity and shape categories below its melting temperature T_m. Since the core-structures of *T-DNA* and *T'-DNA* are the same, here we only take a close look at *T-DNA*, but the observations can be extended to *T'-DNA* or its variants. Table 5.1 shows the level of planarity and the shape categories of *T-DNA* while equilibrated at temperatures of 20°C, 30°C, 40°C, 45°C and 49°C using the analysis method introduced in Sec. 5.2.5. Note that the temperatures taken here are all below the melting temperature, to ensure the core-structure is not fully loosen up; the arm vector is not defined for high temperatures above T_m. Data obtained was averaged over time for one realization, and then ensemble averaged over 10 realizations.

Table 5.1 Structural behaviours of *T-DNA* below T_m

Temperature [°C]	Time spent in a configuration[%]			
	Planar	*Type-I*	*Type-II*	*Type-III*
20	83	55	25	3
30	80	54	22	4
40	77	53	20	4
45	73	53	17	3
49	70	53	14	3

In Table 5.1, at 20°C, 83% of the T molecule is planar. When this happens, the most frequent array is the Y-shape (55% of the time). As the temperature of the

system increases, the fluctuations of the arms causes the T-molecule to spend less time in a planar configurations. However, it is interesting to see that these fluctuations do not affect the Y-shape. For example, the T molecule remains 53% of the time in this configuration at $T = 49$°C. Finally, the same behaviour was observed for the T′ molecules.

The average value of the angles between arms for the Y-shape configuration at 20° C is: $\theta_1 = 90°$, $\theta_2 = 118.5°$ and $\theta_3 = 147.5°$. Since the three arms are not exactly coplanar (define strictly as $d_p = 0$), therefore is not necessarily true that the sum of them is 360°, in this case it is slightly larger. When the temperature of the system is increased to 49°C, the first two angles increase to $\theta_1 = 92°$ and $\theta_2 = 120°$, while the angle $\theta_3 = 145°$ decreases.

5.3.3 Effect of middle inert bases

In Fig. 5.10, we clearly observe that $< d_p >$ changes with both temperature and the number of inert bases in the core. $< ... >$ stands for the time average of the value. First, $< d_p >$ increases with the increase of temperature, indicating an increase of the flexibility of the three-armed structure. But surprisingly, there is no clear trend for the inert bases effect, as the planarity at high temperatures increases when only one inert base is inserted, but all the curves are shifting-up (getting less planar) while inserting two or three additional thymine bases in the middle. This might be explained by the following reasons: while introducing only one extra inert nucleotide, the stress in the centre core of the molecule is relaxed (Fig. 5.6**(a)**); further inserting inert nucleotide will only add additional degrees of freedom, making the core more flexible and thus the configurations less planar (Fig. 5.6**(b)**-**(c)**).

We also compared the planarity and the angular orientations of *T'-DNA* and its variants at $T = 20$°C using the method described in Sec. 5.2.5. Results are listed

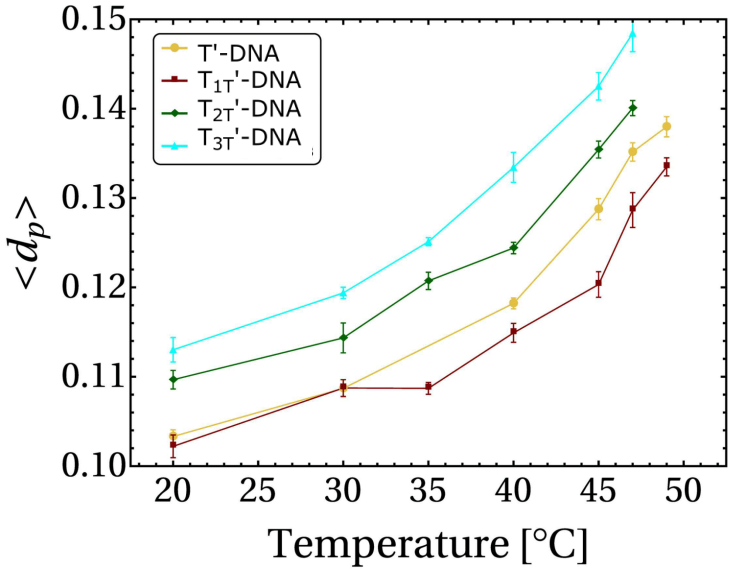

Fig. 5.10 The average distance d_p as function of the temperature for the systems *T'-DNA*, *T'$_{1T}$-DNA*, *T'$_{2T}$-DNA* and *T'$_{3T}$-DNA*.

in Table 5.2. In planar state, the averaged angles of *T'-DNA* is θ_1=90.5°, θ_2=118.2° and θ_3=147.5°, in comparable with that of *T'-DNA* with one extra nucleotide, whose angular information is θ_1=90.2°, θ_2=120.0° and θ_3=145.5°. However, we barely see the changes in the structural behaviours of the three-armed molecules after adding extra inert bases.

Table 5.2 Structural behaviours of *T'-DNA* and its variants with additional inert bases at the core at T = 20°C

Molecule	Time spent in a configuration[%]			
	Planar	*Type-I*	*Type-II*	*Type-III*
T'-DNA	83	55	25	3
T'$_{1T}$-DNA	83	54	23	6
T'$_{2T}$-DNA	80	56	20	4
T'$_{3T}$-DNA	79	57	17	5

5.3.4 Effects of flexible joints

We studied the topological features of two fully assembled three-armed structures connected through sticky-end hybridisation. We characterise the topological feature by two key parameters: the bending angle α and the twist angle β (illustrated in Fig. 5.11). Both α and β are determined by the length of the flexible joint l between the dsDNA arm and the sticky overhang. Given a threshold l_c, when $l > l_c$, the connection is floppy and α and β are independent of the sticky ends; when $l < l_c$, α and β would rely on the length and probably the bases the dsDNA hybridised by sticky ends. We would expect that when $l = 0$, i.e. there is no flexible joint, $\alpha = 180°$ and β is strictly dominated by the number of bases in the sticky ends' binding.

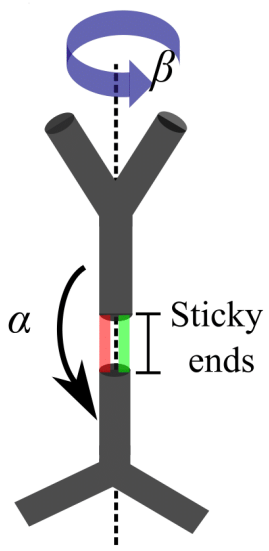

Fig. 5.11 Schematic of two three-armed structures in connection. Red and green lines represent the sticky overhangs from each molecule. α is the bending angle, and β is the twist angle.

We have conducted simulations with $l = 4$, 3, 2, 1, and 0 inert bases by inserting thymine base between the sticky end and the dsDNA arm. To our surprise, none of these systems show a tendency towards the expected $\alpha = 180°$, and two nicks between the unbound backbones always introduce extra degree of freedom for this structure.

Our simulations show (right side of Fig.5.12**(a)**) that in the nicks the DNA exists in the form of equilibrium between two states: the closed state, where the system behaves as if there is no nick, and the open state, where the nick produces a kink, changing drastically the relative orientation of the molecules. Furthermore, we found that the average distance between consecutive phosphates where the nicks are located, $< d_1 >= 1.36$ nm and $< d_2 >= 2.35$ nm respectively, are larger than the equilibrium backbone distance in dsDNA, which is 0.6 nm. In this sense, reducing the stacking distance to 0.6 nm can be seen as a way to produce the structure wanted with α=180°.

Since the DNA stability depends mainly on two types of interactions, stacking between adjacent base pairs and base-pairing, we relate the weakness of these interactions in the nick to the induction of the kink in the backbone. Moreover, it is well known that the stacking interaction is sequence dependent, which could explain why the distance $< d_2 >$ between the bases T-T (with low stacking energy) is larger than $< d_1 >$ between the bases A-C (with a larger stacking energy) in Fig. 5.12**(a)**.

To test this hypothesis, we replace the appropriate bases to produce configurations with the largest possible stacking in the nicks (G-C), the selected bases are shown in red in the 2D-sketch of Fig. 5.12**(b)**. This change resulted in the decreasing of both distances to their new values, $< d_1 >= 1.14$ nm and $< d_2 >= 0.52$ nm, which confirms that the stacking interaction in the nicked region is important to control the relative orientation of the molecules, but also makes it clear that this is not the only relevant information, since the distances although smaller are still different from each other.

In order to see if the sequence in the dsDNA arms was important to reduce the distances previously found, we simulated the same pair of molecules as in Fig. 5.13**(a)** but this time attached by the arms with the same sequence, T_3 and T'_3. This is shown in Fig. 5.13**(b)**, for which $< d_1 >= 1$ nm and $< d_2 >= 0.54$ nm, a relative improvement with respect to the previous case but not enough to achieve the alignment of the

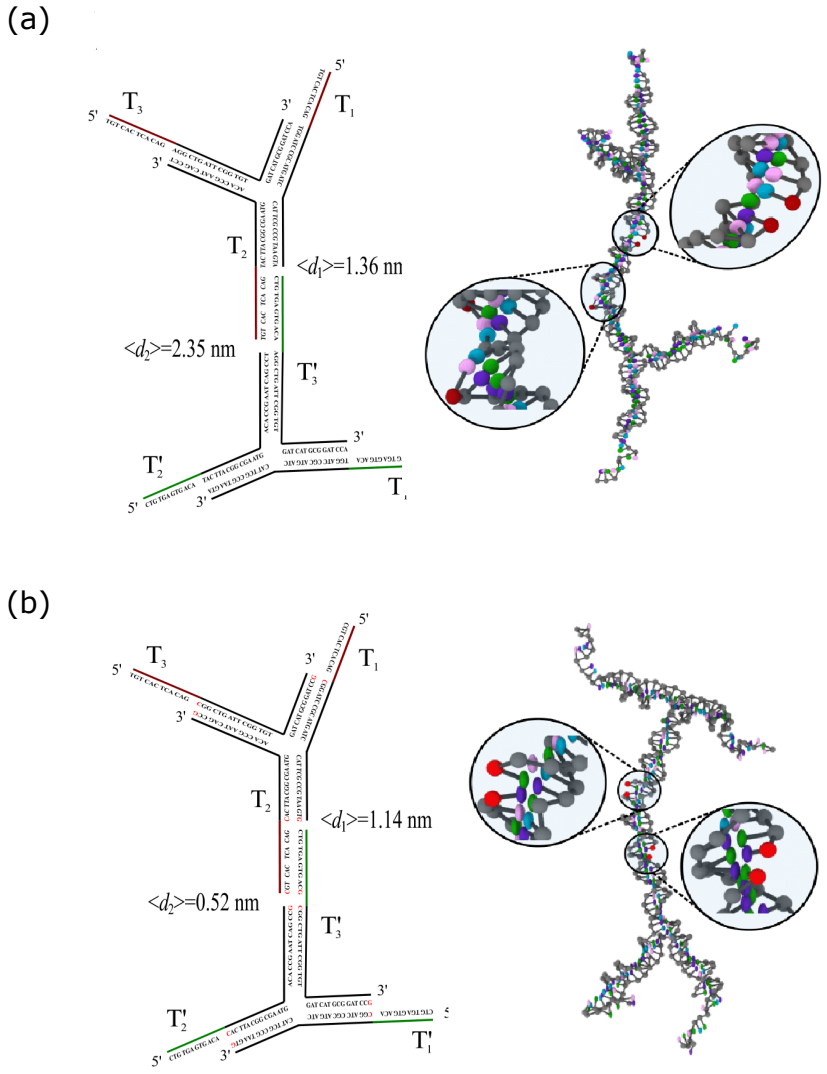

Fig. 5.12 (a) Illustration of original sequences of *T'-DNA* without flexible joints. **(b)** Illustration of modified *T'-DNA* with extra C and G bases added at the end of dsDNA arms. Sequences presented on the left and 3D simulation snapshots on the right. Red beads strand for the nick of the backbones, where two bases are not covalently bound. Assembled structures in the snapshots were equilibrated at $T = 20°C$.

hybridized arms. Therefore the discrepancy in these distances could only possibly come from the sequence in the sticky ends. We tried the case where the base-pair sequence was exactly the same from the middle of the sticky ends to the beginning of each arm (T_3 and T_3'), we found in this case that $< d_1 >=< d_2 >= 0.53$ nm.

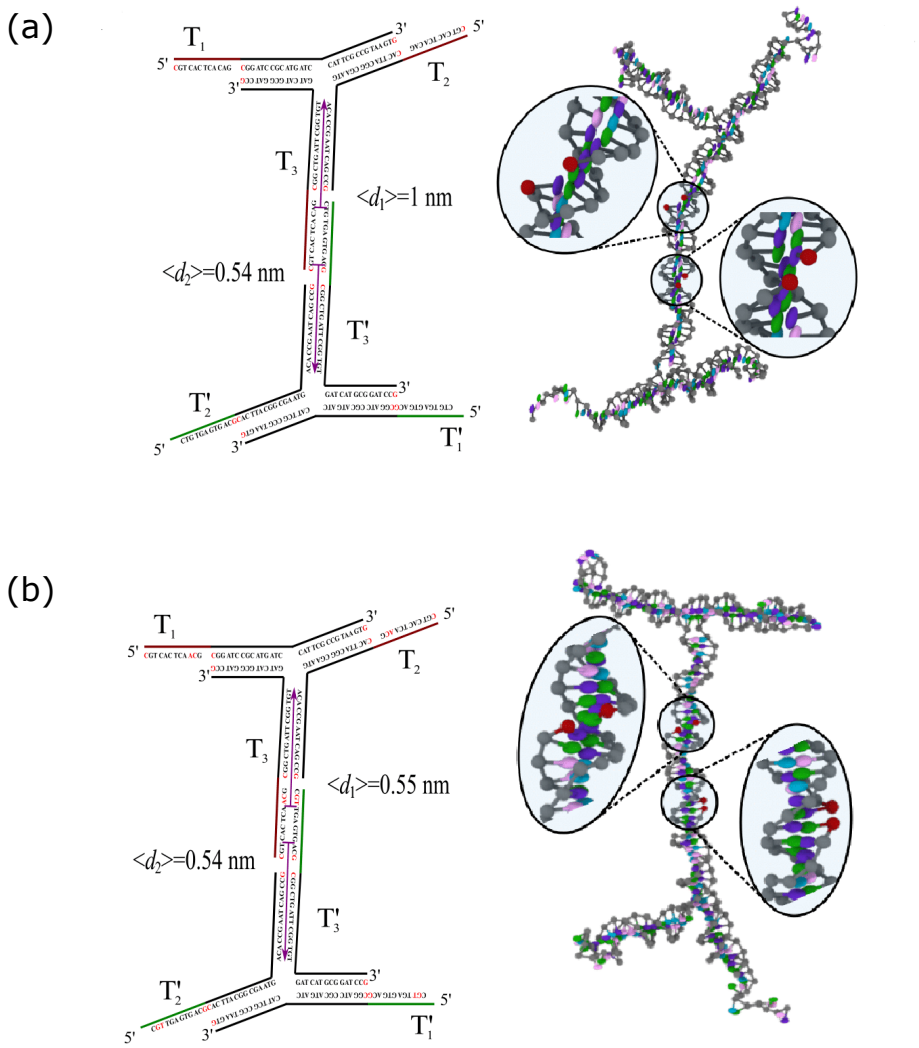

Fig. 5.13 (a) Illustration of modified *T'-DNA* with extra C and G bases added at the end of dsDNA arms and sticky ends (marked in red on the left figure). **(b)** Illustration of modified *T'-DNA* with extra C and G bases added at the end of dsDNA arms and the replacement in the sticky ends' region. Sequences presented on the left and 3D simulation snapshots on the right. Red beads strand for the nick of the backbones, where two bases are not covalently bound. Assembled structures in the snapshots were equilibrated at $T = 20°C$. The purple arrows in the middle of **(a)** and **(b)** show the section which have the same base-pair sequence in the hybridised molecules.

So far we demonstrated that the stacking interaction in the nicks and the sequence in the sticky ends (and arms) are important in the characterization of the system. Now

we would like to find the minimum number of base-pairs we have to replace in the sticky ends to produce the same distance between phosphates in the nicked section. Thus, we changed the base-pair sequence of the sticky end near to one of the nicks, to match the sequence at the sticky end close to the other nick. We did this replacing one base-pair at the time, until we found the sequence shown in Fig.5.13**(a)**. More simulations need to be been done to improve the statistics.

5.4 Conclusions

The overall aim of this chapter is to demonstrate that the coarse-grained model of oxDNA2 can be a helpful guide in the design of a multi-armed DNA structure by providing significant insight into its sequence-dependent topological features. In particular, we studied the three-armed DNA building blocks that were used to construct DNA hydrogel systems described in Chapter 3 and 4 and applied minor modifications on these building blocks by adding inert bases in the original design. We first looked at the individual three-armed structure, and proposed the planarity (defined by d_p) and arm orientations (θ_1, θ_2 and θ_3) as key parameters to characterise the topological features of the structure. By conducting the simulation, we found that the previous assumptions of the three-armed system being 'flat' and dsDNA arms being equally separated is far too ideal. Furthermore, we observed a 'kink' in the twisted central core, which may be responsible for the uneven fluctuation of these three arms. Therefore, we proposed to add inert base in the central core to release the distortion stress and energy penalty caused by the unfavourable twist. The structural behaviours of these modified systems were recorded and further studied. Also, the melting curves measured by simulations are in accordance with the experimental ones, verifying the feasibility of this model applying to the multi-valanced DNA systems.

We also studied the layout of two three-armed DNA structures associated by complimentary sticky ends. Due to the inert flexible joints between the functional sticky ends and dsDNA arms, the two junctions fluctuated with time around the connected region. We used two parameters, the bending angle α and the twist angle β, to define the straightness and rotation of this linking system. We observed that even for systems without a flexible joint, the bending angle α is still not equal to 180° as expected, which is mainly due to flexibility caused by the nicks between the unconnected phosphate backbones. This inspired us to introduce DNA ligase that can seal these open nicks in the future if needed. In addition, we found the straightness of the connected region also depends on the sequence symmetry of the sticky ends and the arms with the connected sticky ends. By smartly placing extra bases inside of the sequences, one may be able to balance up the stress or strain between two building blocks, ending up with a straightened system. Only when the connected region is straight enough can we proceed the analysis of the twist angle β. According to the knowledge of the base stacking, we know *a priori* that β is strictly dominated by the length of the sticky ends (e.g. 10 bp leads to $\beta = 360°$), but more detailed study needs to be conducted in the future.

Though the case we studied here is only a small portion of the multi-valanced systems, the examining routines we have developed and observations we have obtained can be easily extended to more complicated systems. Moreover, by extracting topological features and the key structural parameters acquired from this detailed model, we can design and parameterise the less coarse-grained model (e.g. the one described in Chapter 4) more precisely and accurately. We are not using the oxDNA model for large systems directly because the calculation is too expensive as it considers too many unnecessary details. However, this model is ideal to create a database of all the possible topological layouts of the multi-valanced DNA structures with appropriate

designs, which will be used for creating machine-learning based algorithms that can develop novel DNA hydrogels effectively and efficiently.

5.5 Acknowledgement

I would like to thank Peian Li for constructing the macroscopic gel models; Yair Augusto Gutiérrez Fosado (University of Edinburgh) for writing the simulation scripts and creating the simulation snapshots; Dr. Oliver Henrich (University of Strathclyde) for useful discussions.

Chapter 6

Closing remarks

In this thesis we have experimentally and computationally investigated the self-assembled DNA hydrogel systems made by DNA nano-stars, particularly focusing on the three-armed DNA scaffolds. We have shown that the structural and mechanical properties of DNA hydrogels can be smartly tuned by the specific sequence design of the three-armed scaffolds, which can facilitate the future development of DNA functional hydrogels.

We firstly presented the experimental attempts of making multi-branched DNA complex structures by taking dendrimer-liked DNA complexes as an example. In this exploring work, we have successfully developed a routine of designing, fabricating and characterising the self-assembled DNA scaffolds as we want, which provides a solid experimental platforms for understanding and assembling DNA hydrogels.

Secondly, we have fabricated DNA hydrogels self-assembled by three-armed DNA nano-stars and investigated their mechanical properties employing diffusing wave spectroscopy (DWS) microrheology as well as conventional bulk rheology. The DWS microrheology results have shown a clear liquid-to-gel transition when the temperature cycles up and down across the melting-temperature region of nano-star crosslinkers. Moreover, a crossover between the elastic and loss moduli as a function of frequencies

occurs around the melting temperature T_m of the sticky ends (i.e. cross linkers), coinciding with the systems percolation transition. On the other hand, the bulk rheology results have demonstrated that by reducing the flexibility between three-armed building blocks' bonds, we can go from a semiflexible transient network to a more energy-driven hydrogels with higher elasticity while keeping the microstructure the same. This level of understanding of the mechanical properties of such materials can help us design the systems in turn.

Thirdly, we have established a coarse-grained model of DNA hydrogels to study the thermodynamic, structural and elastic properties of the bulk system. This model has successfully reproduced the thermo-reversible assembly of DNA hydrogel networks and demonstrated the melting behaviours governed by DNA themodynamics. Furthermore, the structural and elastic properties have been studies at various concentrations of the networks, providing physical insights on the microscropic structure of the macroscopic systems. The key aim of this model is to serve as the prediction of the 3D self-assembly of DNA hydrogels.

Last, we also conducted computationally work on analysing the topological behaviours of individual building blocks of the DNA hydrogel system using the oxDNA model. The sequence-dependent layouts of the individual three-armed DNA have been investigated and modifications have been applied by inserting inert bases on the twisted core to tune flexibility of the structure. In addition, the simulation has proved that other than changing the length of the flexible joints, one can also alter the rigidity of the structures of two building blocks in conjunction by playing with the sequence symmetry of the individual building blocks and sticky ends. The crucial topological parameters extracted from this model can be adapted to parameterise the ascribed DNA hydrogel model. More importantly, it can create a database for developing a machine learning algorithm to further understanding underlying physics of such network systems.

In summary, we have mainly focused on the physical aspects of DNA scaffolds and their assembly to DNA hydrogels in this thesis. Various projects have been carried out to design, synthesise, and understand the system, with each project separated but yet correlated to each other. Throughout this work, we have only discussed the three-armed DNA scaffold in detail, because this is the simplest multi-branched DNA structure that can form 3D networks and other systems assembled by DNA nano-stars with 4-, 5-, and n- dsDNA arms are only extensions of this fundamental one. Hence, the routines and conclusions can be easily adapted to various DNA hydrogels networks.

The future work of this project is to achieve highly selective and sensitive molecular sensors using DNA hydrogels as the framework. The selectivity can be based on both the DNA recognition and the microscopic structure of the network (e.g. pore-size, cavity). The sensitivity might be affected by the rigidity of the framework [229]. Baring these in mind, we first need to design such materials and test the feasibility of the desgin using computational models. Only the designs approved by the simulation will be passed for the experimental tests with regards to their performance as molecular sensors, which could incredibly reduce the experimental costs. In this regard, a comprehensive computational model of DNA hydrogels with datasets including vast parameters is greatly needed. However, to my knowledge, no DNA simulation model has currently achieved this goal, not even the models we proposed in chapter 3 and 4. Therefore, further modifications and extensions of these computational models are required, towards characterising DNA hydrogel networks and making accurate predictions of their selectivity and sensibility.

References

[1] James D Watson, Francis HC Crick, et al. A structure for deoxyribose nucleic acid. *Nature*, 171(4356):737–738, 1953.

[2] Young Hoon Roh, Roanna CH Ruiz, Songming Peng, Jong Bum Lee, and Dan Luo. Engineering DNA-based functional materials. *Chemical Society Reviews*, 40(12):5730–5744, 2011.

[3] Nadrian C Seeman. DNA in a material world. *Nature*, 421(6921):427, 2003.

[4] Nadrian C Seeman. Nanomaterials based on DNA. *Annual review of biochemistry*, 79:65–87, 2010.

[5] OpenStax. 9.1: The Structure of DNA. https://bio.libretexts.org/TextMaps/Map%3A_Concepts_in_Biology_(OpenStax)/9%3A_Molecular_Biology/9.1%3A_The_Structure_of_DNA, 2018.

[6] Peter Yakovchuk, Ekaterina Protozanova, and Maxim D Frank-Kamenetskii. Base-stacking and base-pairing contributions into thermal stability of the DNA double helix. *Nucleic acids research*, 34(2):564–574, 2006.

[7] Wikipedia contributors. Hydrogen bond — Wikipedia, The Free Encyclopedia. https://en.wikipedia.org/wiki/Hydrogen_bond, 2018.

[8] Wikipedia contributors. Nucleic acid double helix — Wikipedia, The Free Encyclopedia. https://en.wikipedia.org/wiki/Nucleic_acid_double_helix, 2018.

[9] Stephen Neidle. *Oxford handbook of nucleic acid structure*. Oxford University Press on Demand, 1999.

[10] Anirban Ghosh and Manju Bansal. A glossary of dna structures from a to z. *Acta Crystallographica Section D: Biological Crystallography*, 59(4):620–626, 2003.

[11] Alexander Rich, Alfred Nordheim, and Andrew H-J Wang. The chemistry and biology of left-handed z-dna. *Annual review of biochemistry*, 53(1):791–846, 1984.

[12] Helmut Schiessel. *Biophysics for beginners: a journey through the cell nucleus*. CRC Press, 2013.

[13] Paul WK Rothemund. Folding DNA to create nanoscale shapes and patterns. *Nature*, 440(7082):297, 2006.

[14] Luvena L Ong, Nikita Hanikel, Omar K Yaghi, Casey Grun, Maximilian T Strauss, Patrick Bron, Josephine Lai-Kee-Him, Florian Schueder, Bei Wang, Pengfei Wang, et al. Programmable self-assembly of three-dimensional nanostructures from 10,000 unique components. *Nature*, 552(7683):72, 2017.

[15] Tomas Simonsson. G-quadruplex DNA structures variations on a theme. *Biological chemistry*, 382(4):621–628, 2001.

[16] John SantaLucia Jr and Donald Hicks. The thermodynamics of DNA structural motifs. *Annu. Rev. Biophys. Biomol. Struct.*, 33:415–440, 2004.

[17] Nienke Geerts and Erika Eiser. DNA-functionalized colloids: Physical properties and applications. *Soft Matter*, 6(19):4647–4660, 2010.

[18] Wikipedia contributors. Hoogsteen base pair — Wikipedia, The Free Encyclopedia. https://en.wikipedia.org/wiki/Hoogsteen_base_pair, 2018.

[19] Nienke Geerts et al. *DNA-driven assembly of micron-sized colloids*. Universiteit van Amsterdam [Host], 2009. ISBN: 978-90-6464-359-0.

[20] Yuanchen Dong, Zhongqiang Yang, and Dongsheng Liu. DNA nanotechnology based on i-motif structures. *Accounts of chemical research*, 47(6):1853–1860, 2014.

[21] A Kuzuya and S Tanaka. Hydrogels utilizing g-quadruplexes. *MOJ Poly Sci*, 1(6):00033, 2017.

[22] Yuanchen Dong, Zhongqiang Yang, and Dongsheng Liu. DNA nanotechnology based on i-motif structures. *Accounts of chemical research*, 47(6):1853–1860, 2014.

[23] Lorenzo Di Michele, Bortolo M Mognetti, Taiki Yanagishima, Patrick Varilly, Zachary Ruff, Daan Frenkel, and Erika Eiser. Effect of inert tails on the thermodynamics of DNA hybridization. *Journal of the American Chemical Society*, 136(18):6538–6541, 2014.

[24] John SantaLucia. A unified view of polymer, dumbbell, and oligonucleotide DNA nearest-neighbor thermodynamics. *Proceedings of the National Academy of Sciences*, 95(4):1460–1465, 1998.

[25] Hatim T Allawi and John SantaLucia. Thermodynamics and NMR of internal GT mismatches in DNA. *Biochemistry*, 36(34):10581–10594, 1997.

[26] Chad A Mirkin, Robert L Letsinger, Robert C Mucic, and James J Storhoff. A DNA-based method for rationally assembling nanoparticles into macroscopic materials. *Nature*, 382(6592):607, 1996.

[27] A Paul Alivisatos, Kai P Johnsson, Xiaogang Peng, Troy E Wilson, Colin J Loweth, Marcel P Bruchez Jr, and Peter G Schultz. Organization of'nanocrystal molecules' using DNA. *Nature*, 382(6592):609, 1996.

[28] Sung Yong Park, Abigail KR Lytton-Jean, Byeongdu Lee, Steven Weigand, George C Schatz, and Chad A Mirkin. DNA-programmable nanoparticle crystallization. *Nature*, 451(7178):553, 2008.

[29] Evelyn Auyeung, Ting ING Li, Andrew J Senesi, Abrin L Schmucker, Bridget C Pals, Monica Olvera de La Cruz, and Chad A Mirkin. DNA-mediated nanoparticle crystallization into wulff polyhedra. *Nature*, 505(7481):73, 2014.

[30] Anthony J Kim, Paul L Biancaniello, and John C Crocker. Engineering DNA-mediated colloidal crystallization. *Langmuir*, 22(5):1991–2001, 2006.

[31] Robert J Macfarlane, Byeongdu Lee, Matthew R Jones, Nadine Harris, George C Schatz, and Chad A Mirkin. Nanoparticle superlattice engineering with DNA. *science*, 334(6053):204–208, 2011.

[32] Lorenzo Di Michele, Francesco Varrato, Jurij Kotar, Simon H Nathan, Giuseppe Foffi, and Erika Eiser. Multistep kinetic self-assembly of DNA-coated colloids. *Nature communications*, 4:2007, 2013.

[33] Francesco Varrato, Lorenzo Di Michele, Maxim Belushkin, Nicolas Dorsaz, Simon H Nathan, Erika Eiser, and Giuseppe Foffi. Arrested demixing opens route to bigels. *Proceedings of the National Academy of Sciences*, 109(47):19155–19160, 2012.

[34] Lorenzo Di Michele, D Fiocco, F Varrato, Srikanth Sastry, Erika Eiser, and Giuseppe Foffi. Aggregation dynamics, structure, and mechanical properties of bigels. *Soft Matter*, 10(20):3633–3648, 2014.

[35] Z Ruff, P Cloetens, T O'Neill, Clare Philomena Grey, and E Eiser. Thermally reversible nanoparticle gels with tuneable porosity showing structural colour. *Physical Chemistry Chemical Physics*, 20(1):467–477, 2018.

[36] Mykolas Zupkauskas, Yang Lan, Darshana Joshi, Z Ruff, and E Eiser. Optically transparent dense colloidal gels. *Chemical science*, 8(8):5559–5566, 2017.

[37] Vivek V Thacker, Lars O Herrmann, Daniel O Sigle, Tao Zhang, Tim Liedl, Jeremy J Baumberg, and Ulrich F Keyser. DNA origami based assembly of gold nanoparticle dimers for surface-enhanced raman scattering. *Nature communications*, 5:3448, 2014.

[38] Haley D Hill and Chad A Mirkin. The bio-barcode assay for the detection of protein and nucleic acid targets using dtt-induced ligand exchange. *Nature Protocols*, 1(1):324, 2006.

[39] Darshana Joshi, Dylan Bargteil, Alessio Caciagli, Jerome Burelbach, Zhongyang Xing, André S Nunes, Diogo EP Pinto, Nuno AM Araújo, Jasna Brujic, and Erika Eiser. Kinetic control of the coverage of oil droplets by DNA-functionalized colloids. *Science advances*, 2(8):e1600881, 2016.

[40] Alessio Caciagli, Mykolas Zupkauskas, Aviad Levin, Tuomas PJ Knowles, Clément Mugemana, Nico Bruns, Thomas O'Neill, William J Frith, and Erika Eiser. DNA-coated functional oil droplets. *arXiv preprint arXiv:1710.07820*, 2017.

[41] Yin Zhang, Angus McMullen, Lea-Laetitia Pontani, Xiaojin He, Ruojie Sha, Nadrian C Seeman, Jasna Brujic, and Paul M Chaikin. Sequential self-assembly of DNA functionalized droplets. *Nature Communications*, 8(1):21, 2017.

[42] Maik Hadorn, Eva Boenzli, Kristian T Sørensen, Harold Fellermann, Peter Eggenberger Hotz, and Martin M Hanczyc. Specific and reversible DNA-directed self-assembly of oil-in-water emulsion droplets. *Proceedings of the National Academy of Sciences*, 109(50):20320–20325, 2012.

[43] Lang Feng, Lea-Laetitia Pontani, Rémi Dreyfus, Paul Chaikin, and Jasna Brujic. Specificity, flexibility and valence of DNA bonds guide emulsion architecture. *Soft Matter*, 9(41):9816–9823, 2013.

[44] Dongran Han, Suchetan Pal, Jeanette Nangreave, Zhengtao Deng, Yan Liu, and Hao Yan. DNA origami with complex curvatures in three-dimensional space. *Science*, 332(6027):342–346, 2011.

[45] Grigory Tikhomirov, Philip Petersen, and Lulu Qian. Fractal assembly of micrometre-scale DNA origami arrays with arbitrary patterns. *Nature*, 552(7683):67, 2017.

[46] Florian Praetorius, Benjamin Kick, Karl L Behler, Maximilian N Honemann, Dirk Weuster-Botz, and Hendrik Dietz. Biotechnological mass production of DNA origami. *Nature*, 552(7683):84, 2017.

[47] Fan Hong, Fei Zhang, Yan Liu, and Hao Yan. DNA origami: scaffolds for creating higher order structures. *Chemical reviews*, 117(20):12584–12640, 2017.

[48] Yonggang Ke, Luvena L Ong, William M Shih, and Peng Yin. Three-dimensional structures self-assembled from DNA bricks. *science*, 338(6111):1177–1183, 2012.

[49] Dongran Han, Xiaodong Qi, Cameron Myhrvold, Bei Wang, Mingjie Dai, Shuoxing Jiang, Maxwell Bates, Yan Liu, Byoungkwon An, Fei Zhang, et al. Single-stranded DNA and rna origami. *Science*, 358(6369):eaao2648, 2017.

[50] Anupama J Thubagere, Wei Li, Robert F Johnson, Zibo Chen, Shayan Doroudi, Yae Lim Lee, Gregory Izatt, Sarah Wittman, Niranjan Srinivas, Damien Woods, et al. A cargo-sorting DNA robot. *Science*, 357(6356):eaan6558, 2017.

[51] Jong-Shik Shin and Niles A Pierce. A synthetic DNA walker for molecular transport. *Journal of the American Chemical Society*, 126(35):10834–10835, 2004.

[52] Minghui Liu, Jinglin Fu, Christian Hejesen, Yuhe Yang, Neal W Woodbury, Kurt Gothelf, Yan Liu, and Hao Yan. A DNA tweezer-actuated enzyme nanoreactor. *Nature communications*, 4:2127, 2013.

[53] Haley D Hill and Chad A Mirkin. The bio-barcode assay for the detection of protein and nucleic acid targets using dtt-induced ligand exchange. *Nature Protocols*, 1(1):324, 2006.

[54] Hao Yan, Sung Ha Park, Gleb Finkelstein, John H Reif, and Thomas H LaBean. DNA-templated self-assembly of protein arrays and highly conductive nanowires. *science*, 301(5641):1882–1884, 2003.

[55] Dong Wang, Yue Hu, Peifeng Liu, and Dan Luo. Bioresponsive DNA hydrogels: Beyond the conventional stimuli responsiveness. *Accounts of chemical research*, 50(4):733–739, 2017.

[56] Soong Ho Um, Jong Bum Lee, Nokyoung Park, Sang Yeon Kwon, Christopher C Umbach, and Dan Luo. Enzyme-catalysed assembly of DNA hydrogel. *Nature materials*, 5(10):797–801, 2006.

[57] Libing Zhang, Sae Rin Jean, Sharif Ahmed, Peter M Aldridge, Xiyan Li, Fengjia Fan, Edward H Sargent, and Shana O Kelley. Multifunctional quantum dot DNA hydrogels. *Nature communications*, 8(1):381, 2017.

[58] Juan Li, Cheng Zheng, Sena Cansiz, Cuichen Wu, Jiehua Xu, Cheng Cui, Yuan Liu, Weijia Hou, Yanyue Wang, Liqin Zhang, et al. Self-assembly of DNA nanohydrogels with controllable size and stimuli-responsive property for targeted gene regulation therapy. *Journal of the American Chemical Society*, 137(4):1412–1415, 2015.

[59] Yijie Wang, Yu Shao, Xiaozhou Ma, Bini Zhou, Alan Faulkner-Jones, Wenmiao Shu, and Dongsheng Liu. Constructing tissuelike complex structures using cell-laden DNA hydrogel bricks. *ACS applied materials & interfaces*, 9(14):12311–12315, 2017.

[60] Yanli Ma, Yu Mao, Yuan An, Tian Tian, Huimin Zhang, Jinmao Yan, Zhi Zhu, and Chaoyong James Yang. Target-responsive DNA hydrogel for non-enzymatic and visual detection of glucose. *Analyst*, 143(7):1679–1684, 2018.

[61] Chuang Li, Ping Chen, Yu Shao, Xu Zhou, Yuzhou Wu, Zhongqiang Yang, Zhibo Li, Tanja Weil, and Dongsheng Liu. A writable polypeptide–DNA hydrogel with rationally designed multi-modification sites. *Small*, 11(9-10):1138–1143, 2015.

[62] Chuang Li, Alan Faulkner-Jones, Alison R Dun, Juan Jin, Ping Chen, Yongzheng Xing, Zhongqiang Yang, Zhibo Li, Wenmiao Shu, Dongsheng Liu, et al. Rapid formation of a supramolecular polypeptide–DNA hydrogel for in situ three-dimensional multilayer bioprinting. *Angewandte Chemie International Edition*, 54(13):3957–3961, 2015.

[63] Yongzheng Xing, Enjun Cheng, Yang Yang, Ping Chen, Tao Zhang, Yawei Sun, Zhongqiang Yang, and Dongsheng Liu. Self-assembled DNA hydrogels with designable thermal and enzymatic responsiveness. *Advanced Materials*, 23(9):1117–1121, 2011.

[64] Hao Qi, Majid Ghodousi, Yanan Du, Casey Grun, Hojae Bae, Peng Yin, and Ali Khademhosseini. DNA-directed self-assembly of shape-controlled hydrogels. *Nature communications*, 4:2275, 2013.

[65] Chuang Li, Matthew J Rowland, Yu Shao, Tianyang Cao, Chun Chen, Haoyang Jia, Xu Zhou, Zhongqiang Yang, Oren A Scherman, and Dongsheng Liu. Responsive double network hydrogels of interpenetrating DNA and cb [8] host–guest supramolecular systems. *Advanced Materials*, 27(21):3298–3304, 2015.

[66] Yishun Huang, Wanlin Xu, Guoyuan Liu, and Leilei Tian. A pure DNA hydrogel with stable catalytic ability produced by one-step rolling circle amplification. *Chemical Communications*, 53(21):3038–3041, 2017.

[67] Xiangling Xiong, Cuichen Wu, Cuisong Zhou, Guizhi Zhu, Zhuo Chen, and Weihong Tan. Responsive DNA-based hydrogels and their applications. *Macromolecular rapid communications*, 34(16):1271–1283, 2013.

[68] Jong Bum Lee, Songming Peng, Dayong Yang, Young Hoon Roh, Hisakage Funabashi, Nokyoung Park, Edward J Rice, Liwei Chen, Rong Long, Mingming Wu, et al. A mechanical metamaterial made from a DNA hydrogel. *Nature Nanotechnology*, 7(12):816, 2012.

[69] Fuat Topuz and Oguz Okay. Rheological behavior of responsive DNA hydrogels. *Macromolecules*, 41(22):8847–8854, 2008.

[70] Fuat Topuz and Oguz Okay. Formation of hydrogels by simultaneous denaturation and cross-linking of DNA. *Biomacromolecules*, 10(9):2652–2661, 2009.

[71] Enjun Cheng, Yongzheng Xing, Ping Chen, Yang Yang, Yawei Sun, Dejian Zhou, Lijin Xu, Qinghua Fan, and Dongsheng Liu. A ph-triggered, fast-responding DNA hydrogel. *Angewandte Chemie*, 121(41):7796–7799, 2009.

[72] Silvia Biffi, Roberto Cerbino, Giovanni Nava, Francesca Bomboi, Francesco Sciortino, and Tommaso Bellini. Equilibrium gels of low-valence DNA nanostars: a colloidal model for strong glass formers. *Soft Matter*, 11(16):3132–3138, 2015.

[73] Enjun Cheng, Yulin Li, Zhongqiang Yang, Zhaoxiang Deng, and Dongsheng Liu. DNA-swnt hybrid hydrogel. *Chemical Communications*, 47(19):5545–5547, 2011.

[74] Chun-Hua Lu and Itamar Willner. Stimuli-responsive DNA-functionalized nano-/microcontainers for switchable and controlled release. *Angewandte Chemie International Edition*, 54(42):12212–12235, 2015.

[75] Weiwei Guo, Chun-Hua Lu, Xiu-Juan Qi, Ron Orbach, Michael Fadeev, Huang-Hao Yang, and Itamar Willner. Switchable bifunctional stimuli-triggered poly-n-isopropylacrylamide/DNA hydrogels. *Angewandte Chemie International Edition*, 53(38):10134–10138, 2014.

[76] Weiwei Guo, Chun-Hua Lu, Ron Orbach, Fuan Wang, Xiu-Juan Qi, Alessandro Cecconello, Dror Seliktar, and Itamar Willner. ph-stimulated DNA hydrogels exhibiting shape-memory properties. *Advanced Materials*, 27(1):73–78, 2015.

[77] Chun-Hua Lu, Weiwei Guo, Yuwei Hu, Xiu-Juan Qi, and Itamar Willner. Multi-triggered shape-memory acrylamide–DNA hydrogels. *Journal of the American Chemical Society*, 137(50):15723–15731, 2015.

[78] Yuwei Hu, Chun-Hua Lu, Weiwei Guo, Miguel Angel Aleman-Garcia, Jiangtao Ren, and Itamar Willner. A shape memory acrylamide/DNA hydrogel exhibiting switchable dual ph-responsiveness. *Advanced Functional Materials*, 25(44):6867–6874, 2015.

[79] Xu Yu, Yuwei Hu, Jason S Kahn, Alessandro Cecconello, and Itamar Willner. Orthogonal dual-triggered shape-memory DNA-based hydrogels. *Chemistry-A European Journal*, 22(41):14504–14507, 2016.

[80] Wanlin Xu, Yishun Huang, Haoran Zhao, Pan Li, Guoyuan Liu, Jing Li, Chengshen Zhu, and Leilei Tian. DNA hydrogel with tunable ph-responsive properties produced by rolling circle amplification. *Chemistry-A European Journal*, 23(72):18276–18281, 2017.

[81] Silvia Biffi, Roberto Cerbino, Francesca Bomboi, Elvezia Maria Paraboschi, Rosanna Asselta, Francesco Sciortino, and Tommaso Bellini. Phase behavior and critical activated dynamics of limited-valence DNA nanostars. *Proceedings of the National Academy of Sciences*, 110(39):15633–15637, 2013.

[82] Emanuele Locatelli, Philip H Handle, Christos N Likos, Francesco Sciortino, and Lorenzo Rovigatti. Condensation and demixing in solutions of DNA nanostars and their mixtures. *ACS nano*, 11(2):2094–2102, 2017.

[83] Sándalo Roldán-Vargas, Frank Smallenburg, Walter Kob, and Francesco Sciortino. Gelling by heating. *Scientific reports*, 3:2451, 2013.

[84] Lorenzo Rovigatti, Frank Smallenburg, Flavio Romano, and Francesco Sciortino. Gels of DNA nanostars never crystallize. *ACS nano*, 8(4):3567–3574, 2014.

[85] Francesca Bomboi, Silvia Biffi, Roberto Cerbino, Tommaso Bellini, Federico Bordi, and Francesco Sciortino. Equilibrium gels of trivalent DNA-nanostars: effect of the ionic strength on the dynamics. *The European Physical Journal E*, 38(6):64, 2015.

[86] Silvia Biffi, Roberto Cerbino, Giovanni Nava, Francesca Bomboi, Francesco Sciortino, and Tommaso Bellini. Equilibrium gels of low-valence DNA nanostars: a colloidal model for strong glass formers. *Soft Matter*, 11(16):3132–3138, 2015.

[87] Flavio Romano and Francesco Sciortino. Switching bonds in a DNA gel: An all-DNA vitrimer. *Physical review letters*, 114(7):078104, 2015.

[88] Francesca Bomboi, Flavio Romano, Manuela Leo, Javier Fernandez-Castanon, Roberto Cerbino, Tommaso Bellini, Federico Bordi, Patrizia Filetici, and Francesco Sciortino. Re-entrant DNA gels. *Nature communications*, 7:13191, 2016.

[89] Javier Fernandez-Castanon, Francesca Bomboi, Lorenzo Rovigatti, Marco Zanatta, Alessandro Paciaroni, Lucia Comez, Lionel Porcar, Charl J Jafta, Giulia C Fadda, Tommaso Bellini, et al. Small-angle neutron scattering and molecular dynamics structural study of gelling DNA nanostars. *The Journal of chemical physics*, 145(8):084910, 2016.

[90] Giovanni Nava, Marina Rossi, Silvia Biffi, Francesco Sciortino, and Tommaso Bellini. Fluctuating elasticity mode in transient molecular networks. *Physical review letters*, 119(7):078002, 2017.

[91] Ronald G Larson. *The structure and rheology of complex fluids*, volume 150. Oxford university press New York, 1999.

[92] Daniel TN Chen, Qi Wen, Paul A Janmey, John C Crocker, and Arjun G Yodh. Rheology of soft materials. 2010.

[93] Pietro Cicuta and Athene M Donald. Microrheology: a review of the method and applications. *Soft Matter*, 3(12):1449–1455, 2007.

[94] Todd M Squires and Thomas G Mason. Fluid mechanics of microrheology. *Annual review of fluid mechanics*, 42, 2010.

[95] Bradley W Mansel, Stephen Keen, Philipus J Patty, Yacine Hemar, and Martin AK Williams. A practical review of microrheological techniques. In *Rheology-New Concepts, Applications and Methods*. InTech, 2013.

[96] LA Hough and HD Ou-Yang. Viscoelasticity of aqueous telechelic poly (ethylene oxide) solutions: Relaxation and structure. *Physical Review E*, 73(3):031802, 2006.

[97] Daniel TN Chen, AWC Lau, Lawrence A Hough, Mohammad F Islam, Mark Goulian, Thomas C Lubensky, and Arjun G Yodh. Fluctuations and rheology in active bacterial suspensions. *Physical Review Letters*, 99(14):148302, 2007.

[98] D Mizuno, DA Head, FC MacKintosh, and CF Schmidt. Active and passive microrheology in equilibrium and nonequilibrium systems. *Macromolecules*, 41(19):7194–7202, 2008.

[99] Marina Puig-De-Morales, Mireia Grabulosa, Jordi Alcaraz, Joaquim Mullol, Geoffrey N Maksym, Jeffrey J Fredberg, and Daniel Navajas. Measurement of cell microrheology by magnetic twisting cytometry with frequency domain demodulation. *Journal of Applied Physiology*, 91(3):1152–1159, 2001.

[100] Ben Fabry, Geoffrey N Maksym, James P Butler, Michael Glogauer, Daniel Navajas, and Jeffrey J Fredberg. Scaling the microrheology of living cells. *Physical review letters*, 87(14):148102, 2001.

[101] F Ziemann, J Rädler, and E Sackmann. Local measurements of viscoelastic moduli of entangled actin networks using an oscillating magnetic bead micro-rheometer. *Biophysical Journal*, 66(6):2210–2216, 1994.

[102] RE Mahaffy, CK Shih, FC MacKintosh, and J Käs. Scanning probe-based frequency-dependent microrheology of polymer gels and biological cells. *Physical review letters*, 85(4):880, 2000.

[103] Ovijit Chaudhuri, Sapun H Parekh, and Daniel A Fletcher. Reversible stress softening of actin networks. *Nature*, 445(7125):295, 2007.

[104] Taiki Yanagishima. *DNA-colloid systems and micro-rheology*. PhD thesis, University of Cambridge, 2013.

[105] DJ Pine, DA Weitz, PM Chaikin, and E Herbolzheimer. Diffusing wave spectroscopy. *Physical review letters*, 60(12):1134, 1988.

[106] Thomas G Mason and DA Weitz. Optical measurements of frequency-dependent linear viscoelastic moduli of complex fluids. *Physical review letters*, 74(7):1250, 1995.

[107] Thomas G Mason, Hu Gang, and David A Weitz. Diffusing-wave-spectroscopy measurements of viscoelasticity of complex fluids. *JOSA A*, 14(1):139–149, 1997.

[108] Thomas A Waigh. Microrheology of complex fluids. *Reports on progress in physics*, 68(3):685, 2005.

[109] Todd M Squires and Thomas G Mason. Fluid mechanics of microrheology. *Annual review of fluid mechanics*, 42, 2010.

[110] J Galvan-Miyoshi, J Delgado, and R Castillo. Diffusing wave spectroscopy in maxwellian fluids. *The European Physical Journal E: Soft Matter and Biological Physics*, 26(4):369–377, 2008.

[111] Bruce Tidor, Karl K Irikura, Bernard R Brooks, and Martin Karplus. Dynamics of dna oligomers. *Journal of Biomolecular Structure and Dynamics*, 1(1):231–252, 1983.

[112] M Levitt. Computer simulation of dna double-helix dynamics. In *Cold Spring Harbor symposia on quantitative biology*, volume 47, pages 251–262. Cold Spring Harbor Laboratory Press, 1983.

[113] Charles A Laughton and Sarah A Harris. The atomistic simulation of DNA. *Wiley Interdisciplinary Reviews: Computational Molecular Science*, 1(4):590–600, 2011.

[114] Juan J de Pablo. Coarse-grained simulations of macromolecules: from DNA to nanocomposites. *Annual review of physical chemistry*, 62:555–574, 2011.

[115] Alberto Pérez, F Javier Luque, and Modesto Orozco. Frontiers in molecular dynamics simulations of DNA. *Accounts of chemical research*, 45(2):196–205, 2011.

[116] Davit A Potoyan, Alexey Savelyev, and Garegin A Papoian. Recent successes in coarse-grained modeling of DNA. *Wiley Interdisciplinary Reviews: Computational Molecular Science*, 3(1):69–83, 2013.

[117] Pablo D Dans, Jürgen Walther, Hansel Gómez, and Modesto Orozco. Multiscale simulation of DNA. *Current opinion in structural biology*, 37:29–45, 2016.

[118] Oliver Henrich, Yair Augusto Gutierrez Fosado, Tine Curk, and Thomas E. Ouldridge. Coarse-grained simulation of dna using lammps. *Eur. Phys. J. E*, 41:57, 2018.

[119] Mariano Barbieri, Mita Chotalia, James Fraser, Liron-Mark Lavitas, Josée Dostie, Ana Pombo, and Mario Nicodemi. Complexity of chromatin folding is captured by the strings and binders switch model. *Proceedings of the National Academy of Sciences*, 109(40):16173–16178, 2012.

[120] Yanping Fan, Nikolay Korolev, Alexander P Lyubartsev, and Lars Nordenskiöld. An advanced coarse-grained nucleosome core particle model for computer simulations of nucleosome-nucleosome interactions under varying ionic conditions. *PLoS One*, 8(2):e54228, 2013.

[121] Hajime Kimura, Yasutoshi Shimooka, Jun-ichi Nishikawa, Osamu Miura, Shigeru Sugiyama, Shuji Yamada, and Takashi Ohyama. The genome folding mechanism in yeast. *The Journal of Biochemistry*, 154(2):137–147, 2013.

[122] Natalia Naumova, Maxim Imakaev, Geoffrey Fudenberg, Ye Zhan, Bryan R Lajoie, Leonid A Mirny, and Job Dekker. Organization of the mitotic chromosome. *Science*, 342(6161):948–953, 2013.

[123] Rosana Collepardo-Guevara and Tamar Schlick. Chromatin fiber polymorphism triggered by variations of dna linker lengths. *Proceedings of the National Academy of Sciences*, page 201315872, 2014.

[124] Ognjen Perišić, Rosana Collepardo-Guevara, and Tamar Schlick. Modeling studies of chromatin fiber structure as a function of DNA linker length. *Journal of molecular biology*, 403(5):777–802, 2010.

[125] Petr Šulc, Flavio Romano, Thomas E. Ouldridge, Lorenzo Rovigatti, Jonathan P. K. Doye, and Ard A. Louis. Sequence-dependent thermodynamics of a coarse-grained dna model. *The Journal of Chemical Physics*, 137(13):135101, 2012.

[126] Thomas E Ouldridge, Rollo L Hoare, Ard A Louis, Jonathan PK Doye, Jonathan Bath, and Andrew J Turberfield. Optimizing DNA nanotechnology through coarse-grained modeling: a two-footed DNA walker. *ACS nano*, 7(3):2479–2490, 2013.

[127] Pedro Fonseca, Flavio Romano, John S Schreck, Thomas E Ouldridge, Jonathan PK Doye, and Ard A Louis. Multi-scale coarse-graining for the study of assembly pathways in DNA-brick self-assembly. *The Journal of chemical physics*, 148(13):134910, 2018.

[128] Jonathan PK Doye, Thomas E Ouldridge, Ard A Louis, Flavio Romano, Petr Šulc, Christian Matek, Benedict EK Snodin, Lorenzo Rovigatti, John S Schreck, Ryan M Harrison, et al. Coarse-graining DNA for simulations of DNA nanotechnology. *Physical Chemistry Chemical Physics*, 15(47):20395–20414, 2013.

[129] Anna Stachiewicz and Andrzej Molski. A coarse-grained MARTINI-like force field for DNA unzipping in nanopores. *Journal of computational chemistry*, 36(13):947–956, 2015.

[130] Thomas A Knotts IV, Nitin Rathore, David C Schwartz, and Juan J de Pablo. A coarse grain model for DNA. *The Journal of chemical physics*, 126(8):02B611, 2007.

[131] Yair Augusto Gutierrez Fosado, Davide Michieletto, Jim Allan, CA Brackley, Oliver Henrich, and Davide Marenduzzo. A single nucleotide resolution model for large-scale simulations of double stranded DNA. *Soft matter*, 12(47):9458–9470, 2016.

[132] Ahmadreza F Ghobadi and Arthi Jayaraman. Effect of backbone chemistry on hybridization thermodynamics of oligonucleic acids: a coarse-grained molecular dynamics simulation study. *Soft matter*, 12(8):2276–2287, 2016.

[133] Joshua E Condon and Arthi Jayaraman. Effect of oligonucleic acid (ONA) backbone features on assembly of ONA–star polymer conjugates: a coarse-grained molecular simulation study. *Soft matter*, 13(38):6770–6783, 2017.

[134] Thomas E Cheatham. Simulation and modeling of nucleic acid structure, dynamics and interactions. *Current opinion in structural biology*, 14(3):360–367, 2004.

[135] Chris A Brackley, Stephen Taylor, Argyris Papantonis, Peter R Cook, and Davide Marenduzzo. Nonspecific bridging-induced attraction drives clustering of DNA-binding proteins and genome organization. *Proceedings of the National Academy of Sciences*, 110(38):E3605–E3611, 2013.

[136] Alexander D MacKerell Jr, Joanna Wiorkiewicz-Kuczera, and Martin Karplus. An all-atom empirical energy function for the simulation of nucleic acids. *Journal of the American Chemical society*, 117(48):11946–11975, 1995.

[137] Thomas E Cheatham III, Piotr Cieplak, and Peter A Kollman. A modified version of the cornell et al. force field with improved sugar pucker phases and helical repeat. *Journal of Biomolecular Structure and Dynamics*, 16(4):845–862, 1999.

[138] Eva Fadrna, Nad'a Spackova, Joanna Sarzyñska, Jaroslav Koca, Modesto Orozco, Thomas E Cheatham III, Tadeusz Kulinski, and Jiri Sponer. Single stranded loops of quadruplex DNA as key benchmark for testing nucleic acids force fields. *Journal of chemical theory and computation*, 5(9):2514–2530, 2009.

[139] Modesto Orozco, Agnes Noy, and Alberto Pérez. Recent advances in the study of nucleic acid flexibility by molecular dynamics. *Current opinion in structural biology*, 18(2):185–193, 2008.

[140] Davide Michieletto, Enzo Orlandini, and Davide Marenduzzo. Polymer model with epigenetic recoloring reveals a pathway for the de novo establishment and 3d organization of chromatin domains. *Physical Review X*, 6(4):041047, 2016.

[141] Thomas E Ouldridge. Dna nanotechnology: understanding and optimisation through simulation. *Molecular Physics*, 113(1):1–15, 2015.

[142] Tristan Cragnolini, Philippe Derreumaux, and Samuela Pasquali. Coarse-grained simulations of RNA and DNA duplexes. *The Journal of Physical Chemistry B*, 117(27):8047–8060, 2013.

[143] Jaakko J Uusitalo, Helgi I Ingólfsson, Parisa Akhshi, D Peter Tieleman, and Siewert J Marrink. Martini coarse-grained force field: extension to DNA. *Journal of chemical theory and computation*, 11(8):3932–3945, 2015.

[144] Daniel M Hinckley, Gordon S Freeman, Jonathan K Whitmer, and Juan J De Pablo. An experimentally-informed coarse-grained 3-site-per-nucleotide model of DNA: Structure, thermodynamics, and dynamics of hybridization. *The Journal of chemical physics*, 139(14):10B604_1, 2013.

[145] Nikolay Korolev, Di Luo, Alexander P Lyubartsev, and Lars Nordenskiöld. A coarse-grained DNA model parameterized from atomistic simulations by inverse Monte Carlo. *Polymers*, 6(6):1655–1675, 2014.

[146] Aymeric Naômé, Aatto Laaksonen, and Daniel P Vercauteren. A coarse-grained simulation study of the structures, energetics, and dynamics of linear and circular DNA with its ions. *Journal of chemical theory and computation*, 11(6):2813–2826, 2015.

[147] Alexey Savelyev and Garegin A Papoian. Chemically accurate coarse graining of double-stranded DNA. *Proceedings of the National Academy of Sciences*, 2010.

[148] EJ Sambriski, DC Schwartz, and JJ De Pablo. A mesoscale model of DNA and its renaturation. *Biophysical journal*, 96(5):1675–1690, 2009.

[149] Gordon S Freeman, Daniel M Hinckley, Joshua P Lequieu, Jonathan K Whitmer, and Juan J De Pablo. Coarse-grained modeling of DNA curvature. *The Journal of chemical physics*, 141(16):10B615_1, 2014.

[150] Gordon S Freeman, Joshua P Lequieu, Daniel M Hinckley, Jonathan K Whitmer, and Juan J De Pablo. DNA shape dominates sequence affinity in nucleosome formation. *Physical review letters*, 113(16):168101, 2014.

[151] Daniel M Hinckley and Juan J de Pablo. Coarse-grained ions for nucleic acid modeling. *Journal of chemical theory and computation*, 11(11):5436–5446, 2015.

[152] Joshua P Lequieu, Daniel M Hinckley, and Juan J de Pablo. A molecular view of DNA-conjugated nanoparticle association energies. *Soft Matter*, 11(10):1919–1929, 2015.

[153] Thomas E Ouldridge, Ard A Louis, and Jonathan PK Doye. DNA nanotweezers studied with a coarse-grained model of DNA. *Physical review letters*, 104(17):178101, 2010.

[154] Petr Šulc, Flavio Romano, Thomas E Ouldridge, Lorenzo Rovigatti, Jonathan PK Doye, and Ard A Louis. Sequence-dependent thermodynamics of a coarse-grained DNA model. *The Journal of chemical physics*, 137(13):135101, 2012.

[155] Benedict EK Snodin, Ferdinando Randisi, Majid Mosayebi, Petr Šulc, John S Schreck, Flavio Romano, Thomas E Ouldridge, Roman Tsukanov, Eyal Nir, Ard A Louis, et al. Introducing improved structural properties and salt dependence into a coarse-grained model of DNA. *The Journal of chemical physics*, 142(23):06B613_1, 2015.

[156] Thomas E Ouldridge. *Coarse-grained modelling of DNA and DNA self-assembly*. Springer Science & Business Media, 2012.

[157] Thomas E Ouldridge, Ard A Louis, and Jonathan PK Doye. Structural, mechanical, and thermodynamic properties of a coarse-grained DNA model. *The Journal of chemical physics*, 134(8):02B627, 2011.

[158] Flavio Romano, Alexander Hudson, Jonathan PK Doye, Thomas E Ouldridge, and Ard A Louis. The effect of topology on the structure and free energy landscape of DNA kissing complexes. *The Journal of chemical physics*, 136(21):06B602, 2012.

[159] Petr Šulc, Thomas E Ouldridge, Flavio Romano, Jonathan PK Doye, and Ard A Louis. Modelling toehold-mediated RNA strand displacement. *Biophysical journal*, 108(5):1238–1247, 2015.

[160] Benedict EK Snodin, Flavio Romano, Lorenzo Rovigatti, Thomas E Ouldridge, Ard A Louis, and Jonathan PK Doye. Direct simulation of the self-assembly of a small DNA origami. *ACS nano*, 10(2):1724–1737, 2016.

[161] Rahul Sharma, John S Schreck, Flavio Romano, Ard A Louis, and Jonathan PK Doye. Characterizing the motion of jointed DNA nanostructures using a coarse-grained model. *ACS nano*, 11(12):12426–12435, 2017.

[162] Flavio Romano and Lorenzo Rovigatti. A Nucleotide-Level Computational Approach to DNA-Based Materials. In *Design of Self-Assembling Materials*, pages 71–90. Springer, 2017.

[163] Megan C Engel, David M Smith, Markus A Jobst, Martin Sajfutdinow, Tim Liedl, Flavio Romano, Lorenzo Rovigatti, Ard A Louis, and Jonathan PK Doye. Force-Induced Unravelling of DNA Origami. *ACS nano*, 2018.

[164] Evan Spruijt, Samuel E Tusk, and Hagan Bayley. DNA scaffolds support stable and uniform peptide nanopores. *Nature nanotechnology*, page 1, 2018.

[165] Yougen Li, Yolanda D Tseng, Sang Y Kwon, Leo d'Espaux, J Scott Bunch, Paul L McEuen, and Dan Luo. Controlled assembly of dendrimer-like DNA. *Nature materials*, 3(1):38, 2004.

[166] Robin Holliday. A mechanism for gene conversion in fungi. *Genetics Research*, 5(2):282–304, 1964.

[167] Nadrian C Seeman and Neville R Kallenbach. Design of immobile nucleic acid junctions. *Biophysical journal*, 44(2):201–209, 1983.

[168] Yinli Wang, John E Mueller, Börries Kemper, and Nadrian C Seeman. Assembly and characterization of five-arm and six-arm DNA branched junctions. *Biochemistry*, 30(23):5667–5674, 1991.

[169] Xing Wang and Nadrian C Seeman. Assembly and characterization of 8-arm and 12-arm DNA branched junctions. *Journal of the American Chemical Society*, 129(26):8169–8176, 2007.

[170] Yusuke Sanada, Tomoki Shiomi, Tadashi Okobira, Mengmeng Tan, Makiya Nishikawa, Isamu Akiba, Yoshinobu Takakura, and Kazuo Sakurai. Polypod-Shaped DNAs: Small-Angle X-ray Scattering and Immunostimulatory Activity. *Langmuir*, 32(15):3760–3765, 2016.

[171] Nadrian C Seeman. Nucleic acid junctions and lattices. *Journal of theoretical biology*, 99(2):237–247, 1982.

[172] Anne-Marie Caminade, Cédric-Olivier Turrin, and Jean-Pierre Majoral. Dendrimers and DNA: combinations of two special topologies for nanomaterials and biology. *Chemistry-a European Journal*, 14(25):7422–7432, 2008.

[173] Elham Abbasi, Sedigheh Fekri Aval, Abolfazl Akbarzadeh, Morteza Milani, Hamid Tayefi Nasrabadi, Sang Woo Joo, Younes Hanifehpour, Kazem Nejati-Koshki, and Roghiyeh Pashaei-Asl. Dendrimers: synthesis, applications, and properties. *Nanoscale Research Letters*, 9(1):247, 2014.

[174] Katherine O Freedman, Janet Lee, Yougen Li, Dan Luo, Victoria B Skobeleva, and Pu Chun Ke. Diffusion of single star-branched dendrimer-like dna. *The Journal of Physical Chemistry B*, 109(19):9839–9842, 2005.

[175] Yougen Li, Yen Thi Hong Cu, and Dan Luo. Multiplexed detection of pathogen DNA with DNA-based fluorescence nanobarcodes. *Nature biotechnology*, 23(7):885, 2005.

[176] Jong B Lee, Young H Roh, Soong Ho Um, Hisakage Funabashi, Wenlong Cheng, Judy J Cha, Pichamon Kiatwuthinon, David A Muller, and Dan Luo. Multifunctional nanoarchitectures from DNA-based ABC monomers. *Nature nanotechnology*, 4(7):430, 2009.

[177] Soong Ho Um, Jong Bum Lee, Sang Yeon Kwon, Yougen Li, and Dan Luo. Dendrimer-like dna-based fluorescence nanobarcodes. *Nature protocols*, 1(2):995, 2006.

[178] Sigma-Aldrich. Oligonucleotide Quantification. https://www.sigmaaldrich.com/technical-documents/articles/biology/quantitation-of-oligos.html, 2018.

[179] Chemistry LibreTexts. The Beer-Lambert Law. https://chem.libretexts.org/Core/Physical_and_Theoretical_Chemistry/Spectroscopy/Electronic_Spectroscopy/Electronic_Spectroscopy_Basics/The_Beer-Lambert_Law, 2017. Contributed by Jim Clark.

[180] Dr. Sameh Magdeldin (Ed.). *Gel Electrophoresis-Principles and Basics*. InTech, 2012. ISBN: 978-953-51-0458-2.

[181] Bio-Rad. Protein Electrophoresis Equipment. http://www.bio-rad.com/en-uk/applications-technologies/protein-electrophoresis-equipment?ID=LUSOZFBEB, 2018.

[182] Third Edition Biochemistry. Chapter 6: Techniques of Protein and Nucleic Acid Purification. https://www.wiley.com/college/voet/047119350X/image_gallery/ch06/pages/F06-21.htm, 2004.

[183] Erika Eiser. Dynamic Light Scattering. In *Multi Length-Scale Characterisation*, volume 1, pages 233–282. John Wiley & Sons, Ltd, Chichester, UK, dec 2013.

[184] Bruce J Berne and Robert Pecora. *Dynamic light scattering: with applications to chemistry, biology, and physics*. Courier Corporation, 2000.

[185] Chuang Li, Xu Zhou, Yu Shao, Ping Chen, Yongzheng Xing, Zhongqiang Yang, Zhibo Li, and Dongsheng Liu. A supramolecular hydrogel with identical cross-linking point density but distinctive rheological properties. *Materials Chemistry Frontiers*, 1(4):654–659, 2017.

[186] Oguz Okay. DNA hydrogels: New functional soft materials. *Journal of Polymer Science Part B: Polymer Physics*, 49(8):551–556, 2011.

[187] Chuang Li, Alan Faulkner-Jones, Alison R Dun, Juan Jin, Ping Chen, Yongzheng Xing, Zhongqiang Yang, Zhibo Li, Wenmiao Shu, Dongsheng Liu, et al. Rapid Formation of a Supramolecular Polypeptide–DNA Hydrogel for In Situ Three-Dimensional Multilayer Bioprinting. *Angewandte Chemie International Edition*, 54(13):3957–3961, 2015.

[188] Chuang Li, Matthew J Rowland, Yu Shao, Tianyang Cao, Chun Chen, Haoyang Jia, Xu Zhou, Zhongqiang Yang, Oren A Scherman, and Dongsheng Liu. Responsive double network hydrogels of interpenetrating DNA and CB [8] Host–Guest supramolecular systems. *Advanced Materials*, 27(21):3298–3304, 2015.

[189] Chuang Li, Ping Chen, Yu Shao, Xu Zhou, Yuzhou Wu, Zhongqiang Yang, Zhibo Li, Tanja Weil, and Dongsheng Liu. A Writable Polypeptide–DNA Hydrogel with Rationally Designed Multi-modification Sites. *Small*, 11(9-10):1138–1143, 2015.

[190] Juan Jin, Yongzheng Xing, Yanli Xi, Xueli Liu, Tao Zhou, Xinxin Ma, Zhongqiang Yang, Shutao Wang, and Dongsheng Liu. A triggered DNA hydrogel cover to envelop and release single cells. *Advanced Materials*, 25(34):4714–4717, 2013.

[191] Yu Shao, Haoyang Jia, Tianyang Cao, and Dongsheng Liu. Supramolecular Hydrogels Based on DNA Self-Assembly. *Accounts of Chemical Research*, 50(4):659–668, 2017.

[192] Xu Zhou, Chuang Li, Yu Shao, Chun Chen, Zhongqiang Yang, and Dongsheng Liu. Reversibly tuning the mechanical properties of a DNA hydrogel by a DNA nanomotor. *Chemical Communications*, 52(70):10668–10671, 2016.

[193] Lorenzo Rovigatti, Francesca Bomboi, and Francesco Sciortino. Accurate phase diagram of tetravalent DNA nanostars. *The Journal of Chemical Physics*, 140(15):154903, 2014.

[194] Giovanni Nava, Marina Rossi, Silvia Biffi, Francesco Sciortino, and Tommaso Bellini. Fluctuating Elasticity Mode in Transient Molecular Networks. *Physical Review Letters*, 119(7):078002, 2017.

[195] John G Curro and Philip Pincus. A theoretical basis for viscoelastic relaxation of elastomers in the long-time limit. *Macromolecules*, 16(4):559–562, 1983.

[196] Robert D Groot and Wim GM Agterof. Dynamic viscoelastic modulus of associative polymer networks: Off-lattice simulations, theory and comparison to experiments. *Macromolecules*, 28(18):6284–6295, 1995.

[197] SF Edwards, PJ Lillford, and JMV Blanshard. Gels and networks in practice and theory. *Food structure and behaviour/edited by JMV Blanshard and P. Lillford*, 1987.

[198] Mohammed Filali, Mohamed Jamil Ouazzani, Eric Michel, Raymond Aznar, Grégoire Porte, and Jacqueline Appell. Robust phase behavior of model transient networks. *The Journal of Physical Chemistry B*, 105(43):10528–10535, 2001.

[199] Grégoire Porte, Christian Ligoure, Jacqueline Appell, and Raymond Aznar. Bridging interactions due to telechelic linkers balanced by screened Coulombic repulsions. *Journal of Statistical Mechanics: Theory and Experiment*, 2006(05):P05005, 2006.

[200] Akihiro Koike, Norio Nemoto, Tadashi Inoue, and Kunihiro Osaki. Dynamic light scattering and dynamic viscoelasticity of poly (vinyl alcohol) in aqueous borax solutions. 1. Concentration effect. *Macromolecules*, 28(7):2339–2344, 1995.

[201] Eric Michel, Mohammed Filali, Raymond Aznar, Grégoire Porte, and Jacqueline Appell. Percolation in a model transient network: Rheology and dynamic light scattering. *Langmuir*, 16(23):8702–8711, 2000.

[202] Federica Lo Verso, Athanassios Z. Panagiotopoulos, and Christos N. Likos. Aggregation phenomena in telechelic star polymer solutions. *Physical Review E*, 79:010401(R), 2009.

[203] Gábor Erdödi and Béla Iván. Novel Amphiphilic Conetworks Composed of Telechelic Poly(ethylene oxide) and Three-Arm Star Polyisobutylene. *Chem. Mater.*, 16(6):959–962, 2004.

[204] Erika Eiser, Jacob Klein, Thomas A Witten, and Lewis J Fetters. Shear of telechelic brushes. *Physical review letters*, 82(25):5076, 1999.

[205] Mahsa Vahabi, Bart E Vos, Henri CG de Cagny, Daniel Bonn, Gijsje H Koenderink, and FC MacKintosh. Normal stresses in semiflexible polymer hydrogels. *arXiv preprint arXiv:1712.02733*, 2017.

[206] Damien Montarnal, Mathieu Capelot, François Tournilhac, and Ludwik Leibler. Silica-like malleable materials from permanent organic networks. *Science*, 334(6058):965–968, 2011.

[207] Mathieu Capelot, Miriam M Unterlass, François Tournilhac, and Ludwik Leibler. Catalytic control of the vitrimer glass transition. *ACS Macro Letters*, 1(7):789–792, 2012.

[208] Séverine Rose, Alexandre Prevoteau, Paul Elzière, Dominique Hourdet, Alba Marcellan, and Ludwik Leibler. Nanoparticle solutions as adhesives for gels and biological tissues. *Nature*, 505(7483):382–385, 2014.

[209] Wei Pan, Hao Wen, Lin Niu, Cuicui Su, Chenyang Liu, Jiang Zhao, Chengde Mao, and Dehai Liang. Effects of chain flexibility on the properties of DNA hydrogels. *Soft matter*, 12(25):5537–5541, 2016.

[210] Junfang Li, To Ngai, and Chi Wu. The slow relaxation mode: from solutions to gel networks. *Polymer journal*, 42(8):609–625, 2010.

[211] Niu Lin, Xuyang Yang, Wei Pan, Tao Zhou, Dongsheng Liu, and Dehai Linag. Effects of Structural Flexibility on the Kinetics of DNA Y-Junction Assembly and Gelation. *Langmuir*, 32:12862, 2016.

[212] Emanuele Locatelli, Philip H Handle, Christos N Likos, Francesco Sciortino, and Lorenzo Rovigatti. Condensation and demixing in solutions of DNA nanostars and their mixtures. *ACS nano*, 11(2):2094–2102, 2017.

[213] Matthew R Jones, Nadrian C Seeman, and Chad A Mirkin. Programmable materials and the nature of the DNA bond. *Science*, 347(6224):1260901, 2015.

[214] Javier Fernandez-Castanon, Francesca Bomboi, Lorenzo Rovigatti, Marco Zanatta, Alessandro Paciaroni, Lucia Comez, Lionel Porcar, Charl J Jafta, Giulia C Fadda, Tommaso Bellini, et al. Small-angle neutron scattering and molecular dynamics structural study of gelling DNA nanostars. *The Journal of Chemical Physics*, 145(8):084910, 2016.

[215] Zhongyang Xing, Alessio Caciagli, Tianyang Cao, Iliya Stoev, Mykolas Zupkauskas, Thomas O'Neill, Tobias Wenzel, Robin Lamboll, Dongsheg Liu, and Erika Eiser. Microrheology of DNA Hydrogels. *arXiv preprint arXiv:1712.07956*, 2017.

[216] Petr Šulc, Thomas E Ouldridge, Flavio Romano, Jonathan PK Doye, and Ard A Louis. Simulating a burnt-bridges DNA motor with a coarse-grained DNA model. *Natural Computing*, 13(4):535–547, 2014.

[217] Mirjam E Leunissen and Daan Frenkel. Numerical study of DNA-functionalized microparticles and nanoparticles: Explicit pair potentials and their implications for phase behavior. *The Journal of chemical physics*, 134(8):084702, 2011.

[218] Stefano Angioletti-Uberti, Bortolo M Mognetti, and Daan Frenkel. Re-entrant melting as a design principle for DNA-coated colloids. *Nature materials*, 11(6):518–522, 2012.

[219] Stefano Angioletti-Uberti, Bortolo M Mognetti, and Daan Frenkel. Theory and simulation of DNA-coated colloids: a guide for rational design. *Physical Chemistry Chemical Physics*, 18(9):6373–6393, 2016.

[220] Stefano Angioletti-Uberti, Patrick Varilly, Bortolo M Mognetti, and Daan Frenkel. Mobile linkers on DNA-coated colloids: valency without patches. *Physical review letters*, 113(12):128303, 2014.

[221] Aleks Reinhardt and Daan Frenkel. Numerical evidence for nucleated self-assembly of DNA brick structures. *Physical review letters*, 112(23):238103, 2014.

[222] Hannah K Wayment-Steele, Daan Frenkel, and Aleks Reinhardt. Investigating the role of boundary bricks in DNA brick self-assembly. *Soft Matter*, 13(8):1670–1680, 2017.

[223] Francis W Starr and Francesco Sciortino. Model for assembly and gelation of four-armed dna dendrimers. *Journal of Physics: Condensed Matter*, 18(26):L347, 2006.

[224] Zhongyang Xing, Alessio Caciagli, Tianyang Cao, Iliya Stoev, Mykolas Zupkauskas, Thomas O'Neill, Tobias Wenzel, Robin Lamboll, Dongsheng Liu, and Erika Eiser. Microrheology of dna hydrogels. *Proceedings of the National Academy of Sciences*, page 201722206, 2018.

[225] Steve Plimpton. Fast parallel algorithms for short-range molecular dynamics. *Journal of Computational Physics*, 117(1):1–19, 1995.

[226] Peter J Daivis and BD Todd. A simple, direct derivation and proof of the validity of the SLLOD equations of motion for generalized homogeneous flows. *The Journal of chemical physics*, 124(19):194103, 2006.

[227] Denis J Evans and GP Morriss. Nonlinear-response theory for steady planar Couette flow. *Physical Review A*, 30(3):1528, 1984.

[228] MediaWiki. DNA model introduction. https://dna.physics.ox.ac.uk/index.php/DNA_model_introduction, 2017.

[229] Tine Curk, Jure Dobnikar, and Daan Frenkel. Rational design of molecularly imprinted polymers. *Soft Matter*, 12(1):35–44, 2016.

[230] Petr Štěpánek, Wyn Brown, and Søren Hvidt. Relaxation of concentration fluctuations in a shear field. *Macromolecules*, 29(27):8888–8893, 1996.

[231] Manlio Tassieri, RML Evans, Rebecca L Warren, Nicholas J Bailey, and Jonathan M Cooper. Microrheology with optical tweezers: data analysis. *New Journal of Physics*, 14(11):115032, 2012.

Appendix A

Preparation of polyacrylamide gel

10 % polyacrylamide gel supplemented with 11 mM $MgCl_2$ was prepared to analyse partial and full formations of branched DNA structures (30 to 150 bases). Recipe for preparation the gel is presented in Tab. A.1. To prepare the gel, one should first mix up 30 % acrylamide/bis-acrylamide (Sigma-Aldrich®), 10× TBE buffer (Sigma-Aldrich®), 0.5 M $MgCl_2$ solution and double-distilled H_2O (written as ddH_2O). Next, add TEMD (N,N,N,N- Tetramethylethylenediamine, Sigma-Aldrich®) and 10% ammounium persulfate (APS, Sigma-Aldrich®) in sequence and gentle vortex the mixture. The mixture solution is set for about 20 minutes to allow the polymerisation reaction's happening.

Table A.1 Recipe for preparation of 10 % polyacrylamide separating gel

Solution	Volume
Acrylamide/Bis-acrylamide, 30 %	5 mL
TBE buffer, 10×	750 µL
$MgCl_2$, 0.5 M	330 µL
ddH_2O	8.92 mL
TEMD	5 µL
Ammonium persulfate, 10 %	150 µL
Final volume	15.16 mL

Preparation of polyacrylamide gel

After setting up the gel, roughly 12 µL sample stained by DNA dye (Gel Loading Dye, Purple (6x), New England Biolab®) is loaded in each gel well, with the total molecular weight of DNA aiming at 200 $\sim$ 300 Da per well. 0.5$\times$ TBE buffer containing 11 mM $MgCl_2$ is prepared as running buffer. $MgCl_2$ added in both the gel and the running buffer is for stablising DNA hybridization while the samples migrating through the gel matrix.

Appendix B

DWS measurements with 230nm PS beads

B.0.1 Cooling and heating ramps

We also conducted the DWS measurements using 230 nm PS particles as probe beads, following the same routine as the 600 nm ones. The sample was 1.4 - 2 v/v % Y-shaped DNA containing 1 v/v % concentration of the colloids. Cooling down and measurements were taken starting from 50 °C to 17 °C at an interval of 1 °C. The decay time increases as the temperature goes up.

The ICF data for the cooling-down and heating-up ramps are shown in Fig. B.1A, and they are in good agreement with each other, indicating the thermal reversibility of the DNA hydrogen bonds between sticky ends.

MSD results converted from the the intensity correlation functions are shown in Fig. B.1B. *Top* and *bottom* figures that present the temperature-evolvement of MSD at cooling and heating ramps respectively show a similar trend, illustrating litter hysteresis. At high temperatures (read lines), the MSD curves are linear over the whole lag time region, confirming the $\langle \Delta r(t)^2 \propto \tau \rangle$ relation in a fluid. At low temperatures,

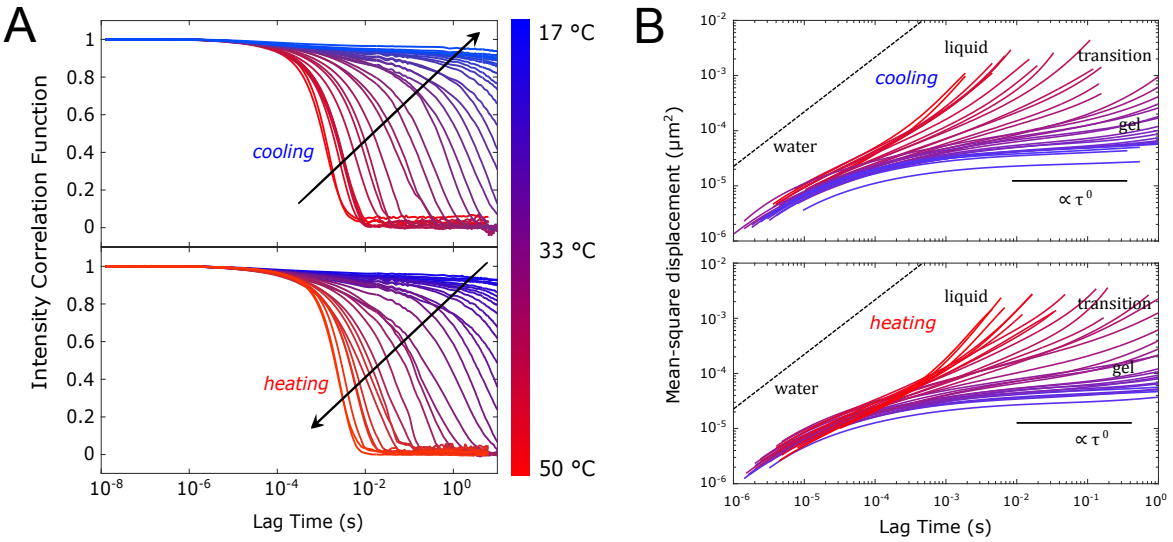

Fig. B.1 (A) The temperature-dependent intensity-correlation function (ICF) data measured from the described DNA hydrogel sample containing 1 v/v % of 230 nm sterically stablised polysterene particles. *Top* The cooling ramp for the temperature ranging from 50 °C to 17 °C (from the red lines to the blue lines), and *bottom* the corresponding heating ramp . (B) Mean-square displacements (MSD) extracted from the ICF curves. The dashed lines are the theoretical MSD curves for the tracer particles at room temperature in pure buffer solution, shown as reference. The gray regions in the plots indicate the melting-temperature transition region.

the MSD curves are linear at short lag times, but gradually reach a plateau on long time scales. This means the trace particles are diffusing thermally on short time scales, but confined on long time scales, which illustrates the formation of a network of surrounding environment.

The rheological moduli results, elastic modulus G'(ω) and viscous modulus G"(ω), are shown in Fig. B.2 . The results in cooling ramp (Fig. B.2 A and B) are in good agreement with that in the heating ramp, suggesting that little hysteresis and ageing effects are involved. The elastic modulus, G'(ω), obtained from the cooling and heating ramps shows a significant variation as the temperature changes over the melting-temperature transition, while the viscous modulus, G"(ω), retains the same trend over the same temperature range. The results for 230 nm tracer particles correspond to the ones for 600 nm trace particles shown in the main text, showing that it is independent

from the size of the tracer particles. The surface functions of the trace particles are also different, suggesting that we have successfully selected the particles whose surface functional group does not interact with DNA.

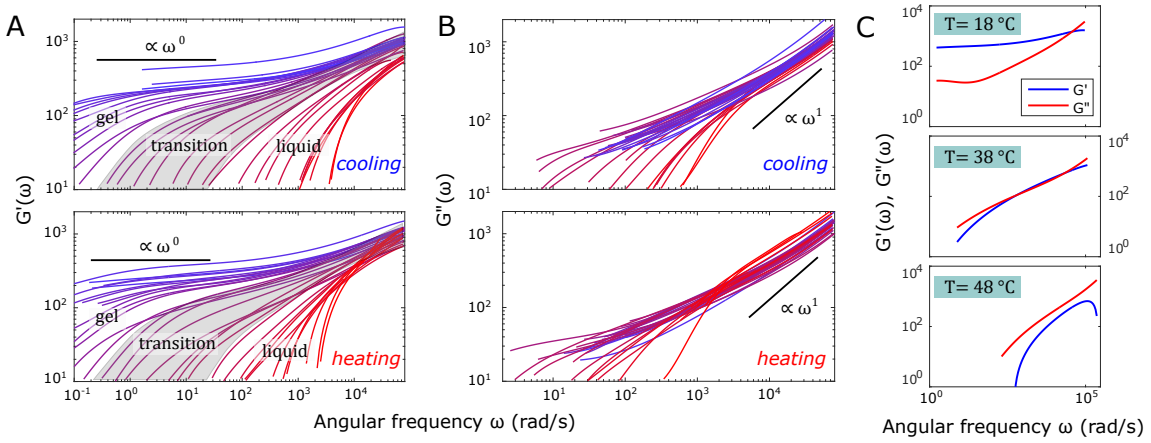

Fig. B.2 Temperature-evolution of the complex moduli $G'(\omega)$ and $G''(\omega)$ as a function of frequency extracted from the MSDs in Fig. B.1. (A) The elastic moduli $G'(\omega)$ measured in cooling and heating ramps. At temperatures above T_{m2}, G' drops down at a frequency below $10^2 \sim 10^4 rad/s$, showing close-to-zero elasticity; below T_{m2}, only th e onset of the decay in the ICF could be monitored. (B) The viscous modulus $G''(\omega)$ in cooling (*top*) ramp. (C) Comparison of $G'(\omega)$ and $G''(\omega)$ at temperatures of 18 °C, 38 °C, and 48 °C, representing typical behavior at temperatures below, around, and above T_m. At 18 °C, G'' is higher than G' at frequencies below the crossover frequency $\sim 10^4$ rad/s; at 38 °C, G' and G'' are overlapping over almost the entire frequency range; at 48 °C, G'' is higher than G' over the whole measurable frequency range, showing no crossover point at all.

B.0.2 Time evolution DWS measurements

To ensure the DNA hydrogel sample stays at its equilibrium state during the DWS measurements duration, we performed a series of time evolution experiments for the sample at the time sequences up to 25 minutes after loading, at temperatures ranging from below to above the melting-transition region. All measurements were performed on the DNA hydrogel sample at the T-DNA/T'-DNA concentration of 500 µM with 1 v/v % 230 nm sterically stablised polystyrene particles. Intensity correlation functions

(ICF) on various temperatures were obtained after 1, 3 , 5 , 7 , 10 , 15 and 25 minutes waiting time respectively after bringing the sample to a given temperature (Fig. B.3). Fig. B.4 shows the half-decay times extracted from the ICF results, showing the changes with temperature. Each data point was averaged over seven measurements at different times, and the error bar represents the statistic error. Results shows that the aging effect is minor compared to the temperature effect.

B.0.3 Microrheology: data analysis

Data analysis is performed via custom routines written in MATLAB (R2016b). The raw autocorrelation curves obtained by DWS measurements are fitted to a multiexponential function of the form:

$$g_1(\tau) = \sum_i a_i e^{-\Gamma_i \tau} \tag{B.1}$$

The form of the fit is motivated by the fact that the autocorrelation function $g_1(\tau)$ for the detector geometry adopted is nearly exponential and is thus expected to be well represented by the chosen functional form [105]. The parameters a_i and Γ_i are obtained via the well known CONTIN method [230]. The mean square displacement (MSD) $\langle \Delta r^2(\tau) \rangle$ is obtained from the fitted autocorrelation curves by inverting the following equation [105] and solving for x:

$$g_1(\tau) = \frac{\frac{L/l^* + 4/3}{a^* + 2/3} \sinh(a^* x) + 2/3\, x\, \cosh(a^* x)}{(1 + 4/9\, x^2) \sinh(L/l^*\, x) + 4/3\, x\, \cosh(L/l^*\, x)} \tag{B.2}$$

where $x = \sqrt{q_0^2 \langle \Delta r^2(\tau) \rangle}$, $a^* = z_0/l^*$, z_0 is the distance into the sample from the incident surface to the place where the diffuse source is located (calibration parameters outputted from the DWS setup), $q_0 = 2\pi n_s/\lambda$ is the photon wave vector in the solvent, λ is the laser wavelength, n_s is the index of refraction of the solvent and L is the cuvette thickness.

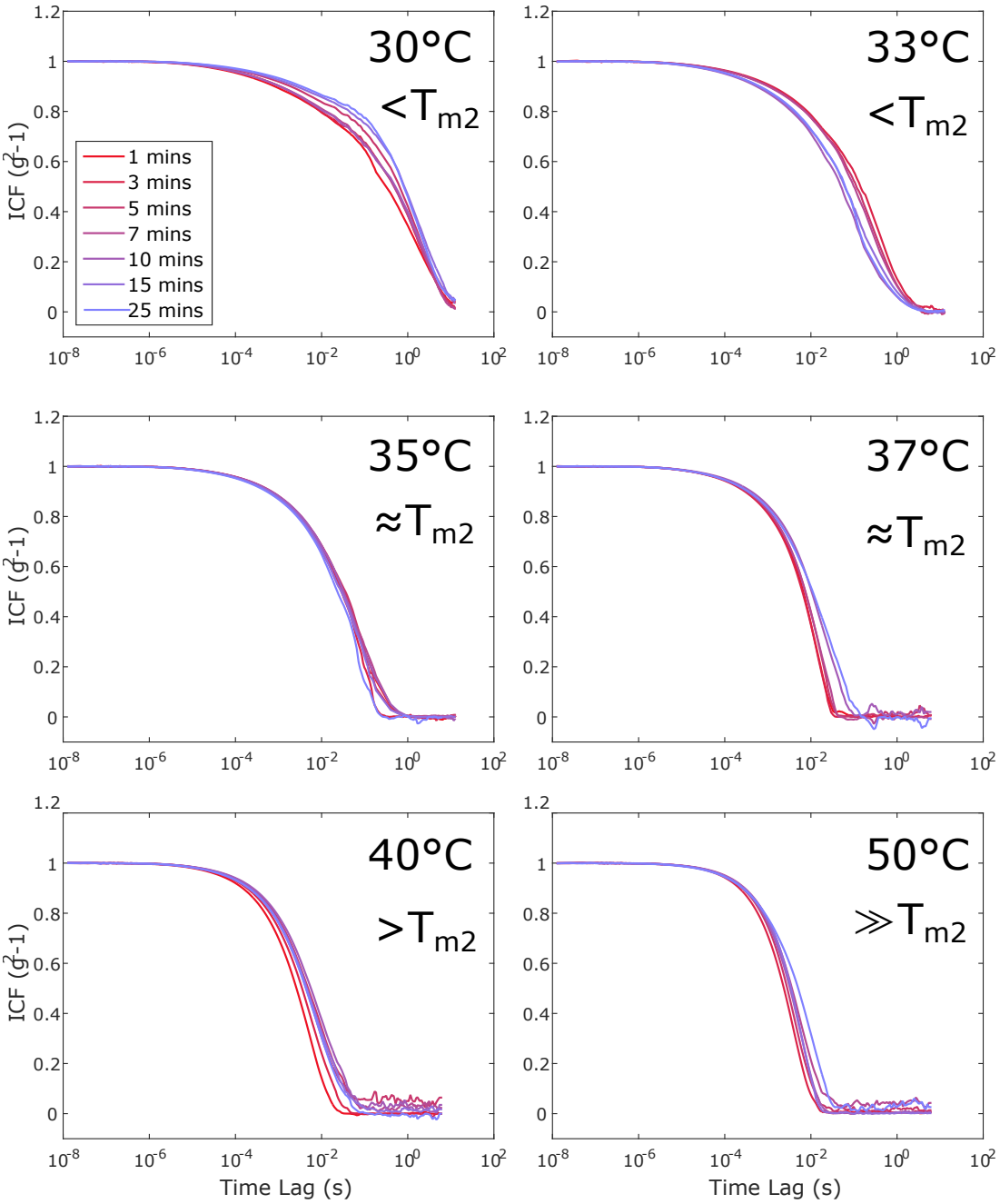

Fig. B.3 Aging effects at different temperatures. All figures are obtained from the DNA hydrogel sample with a DNA concentration of 500 µM using 230 nm sterically stablised polystyrene particles. The intensity correlation functions (ICF) were measured 1, 3, 5, 7, 10, 15 and 25 minutes directly after placing the sample into the cell.

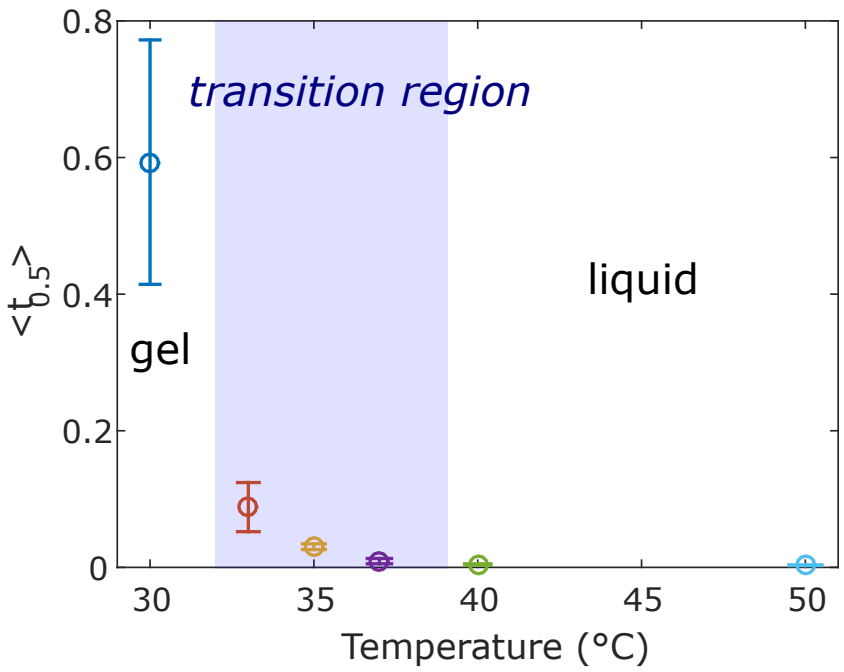

Fig. B.4 Half-decayed time point extracted from ICF results against temperature. The transition region is marked in blue region. The region on the left is the gel state and on the right is the liquid state.

The MSD curves are converted into the complex modulus $G^*(\omega)$ by direct conversion following the approach by Evans and expanded by Tassieri [231].

Appendix C

Re-scaled temperature for melting curves

We can manipulate the pair interactions by changing the potential depth between attractive pairs. Fig. C.1A shows the melting curves at $\epsilon^{\text{pair}} = 2$, 4 and 6 ϵ_{LJ} with other parameters retain the same as in the main text (simulation taken in a $\rho = 1.39\,\sigma_{\text{LJ}}^{-3}$ system). We can clearly see the curve shifting rightwards as the potential depth decreasing. If we rescale the simulation temperature T to the rescaled temperature T^* following the equation below

$$T^* = T/\epsilon^{\text{pair}}, \tag{C.1}$$

we can easily obtain a merge of the curves shown in Fig. C.1. Though there is a small gap between the rescaled melting curve, it may be due to the other potentials involved in the overall rescaling process.

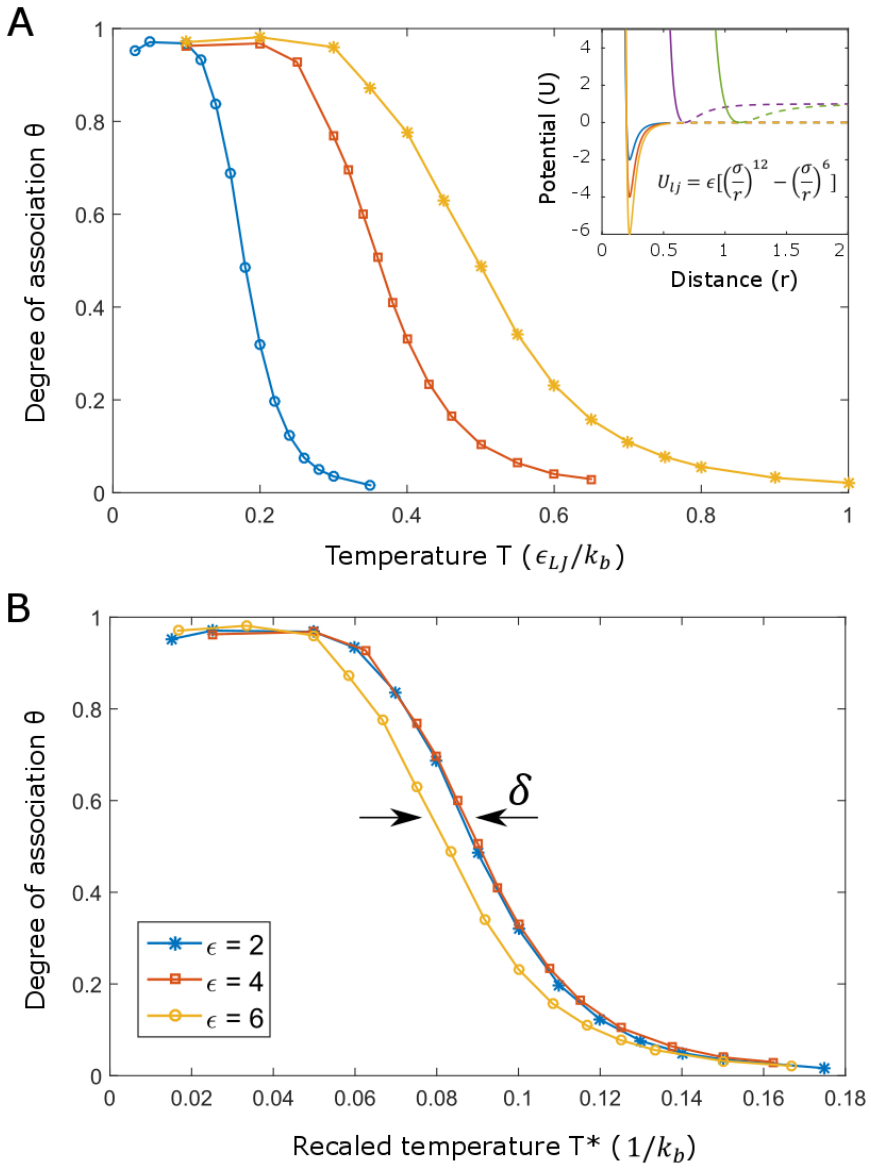

Fig. C.1 The melting curves varied on $\epsilon = 2$, 4, and 6 ϵ_{LJ}. **A.** Degree of association θ against the unitless temperature T. The values of the temperatures were taken from the simulations directly. The figure embedded on right-top corner plots all the pair potentials involved. The solid lines are the working part, while the dashed lines stand for the truncated parts. The purple and green curves stand for WCA potentials of A-B patches and standard beads respectively. **B.** Degree of association θ against the rescaled temperature T^*. Simulations were taken on a system of $\rho = 1.39\,\sigma_{\mathrm{LJ}}^{-3}$ at a cubic simulation box at the length of 30 σ_{LJ}.

Appendix D

Calculating characteristic distances of basic configurations

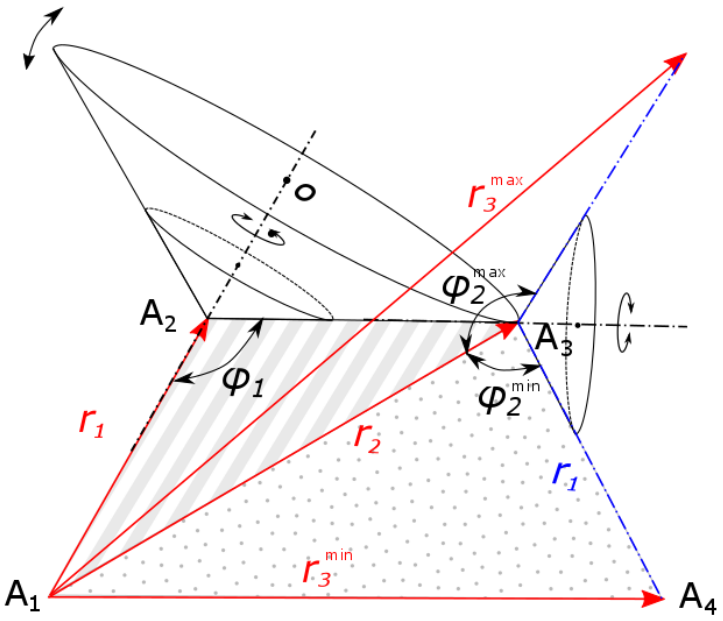

Fig. D.1 Simplified geometrical sketch of four connected Y-shaped units.

Here we introduce the calculations for r_1, r_2 and r_3. Fig. D.1 presents the geometrical relation between central points of four Y-shaped units (marked as A_1, A_2, A_3 and A_4).

As mentioned in Section IV, r_1 is twice length as l shown in Eq. D.1

$$r_1 = 2 \times l \tag{D.1}$$

where $l = 2.48\,\sigma_{\mathrm{LJ}}$ is the arm length of Y-shaped units, estimated according to parameter setting in Section II. Therefore, $r_1 \approx 4.96\,\sigma_{\mathrm{LJ}}$. Applying laws of cosines to the triangles marked in stripe and dots in Fig. D.1, we can acquire r_2 and r_3 using

$$r_2 = \sqrt{r_1^2 + r_1^2 - 2 \times r_1 \times r_1 \cos(\varphi_1)} \tag{D.2}$$

$$r_3 = \sqrt{r_1^2 + r_2^2 - 2 \times r_1 \times r_2 \cos(\varphi_2)}. \tag{D.3}$$

We know that φ_1 is 120°, but φ_2 is unknown because it depends on the rotation of smaller cone sketched in Fig. D.1. However, we can obtain the range of φ_2 as the minimum (Eq. D.4) and maximum (Eq. D.5) values as 90° and 150° respectively.

$$\varphi_2^{min} = \angle A_2 A_3 A_4 - \angle A_1 A_3 A_2 = 120^\circ - 30^\circ = 90^\circ. \tag{D.4}$$

$$\varphi_2^{max} = \angle A_2 A_3 A_4 + \angle A_1 A_3 A_2 = 120^\circ + 30^\circ = 150^\circ. \tag{D.5}$$

So we can estimate from Eqn. D.2 to D.5 that $r_2 \approx 8.59\,\sigma_{\mathrm{LJ}}$ and r_3 ranges between $9.92 \sim 13.12\,\sigma_{\mathrm{LJ}}$ (marked in Fig. 4.7(a) and (b)). By assuming that φ_2 is uniformly distributed between $\varphi_2^{\min} = 90^\circ$ and $\varphi_2^{\max} = 150^\circ$ (Eq. D.6),

$$f(\varphi_2) = \begin{cases} 3/\pi, & \text{if } 90^\circ \leq \varphi_2 \leq 150^\circ \\ 0, & \text{otherwise} \end{cases} \tag{D.6}$$

we can calculate the expectation of r_3 as follows:

$$\begin{aligned}\langle r_3 \rangle &= \int_0^{\pi} \varphi_2 \; f(\varphi_2) \; d\varphi_2 \\ &= \int_{\pi/2}^{5\pi/6} 2 \; r_1 \sqrt{1 - \frac{\sqrt{3}}{2} \cos \varphi_2} \; d\varphi_2\end{aligned} \tag{D.7}$$

Therefore, we estimate from Eq. D.7 that $\langle r_3 \rangle \approx 2.37 \; r_1 \approx 11.76 \; \sigma_{\mathrm{LJ}}$.

Appendix E

Pre-testing results in linear elasticity simulation

E.1 Determining the linear region

We perform xy-direction shear deformation at constant shear rate to determine the linear region of the system. Fig. E.1 shows the shear stress responses σ_{xy} against the shear strain γ at various shear rates $\dot{\gamma}$. In the oscillatory shear, we choose the strain amplitude γ_0 within the region where the stress and rate retains linear relationship.

E.2 Integration errors

We tested the integration errors while applying oscillatory shear at various time step interval δt and period T_p (Fig. E.2). The integration error is evaluated by the amplitude of the output stress σ_0. There is a threshold, below which the output stress amplitude σ_0 stays the same; otherwise it drops down as time interval increases. This effect is more obvious for short period, i.e. high frequency, so special care needs to be taken in the simulations.

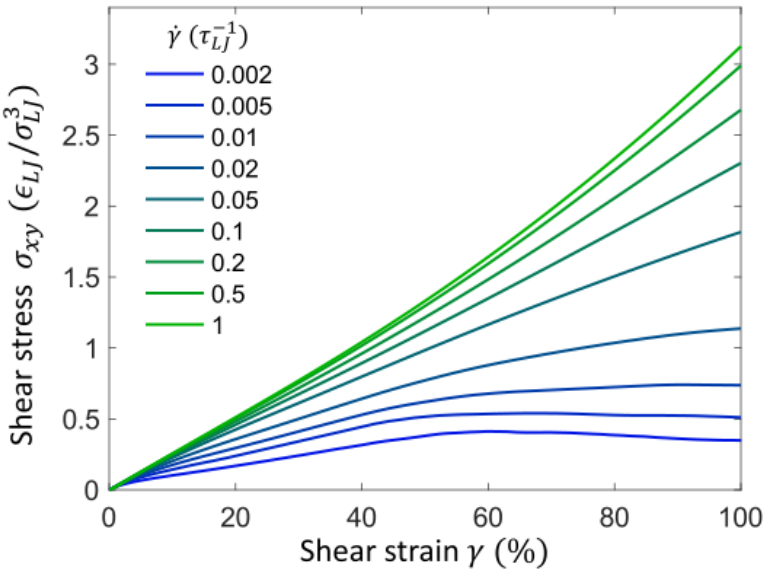

Fig. E.1 Shear stress against shear strain ranging from 0 to 100% at various shear rates.

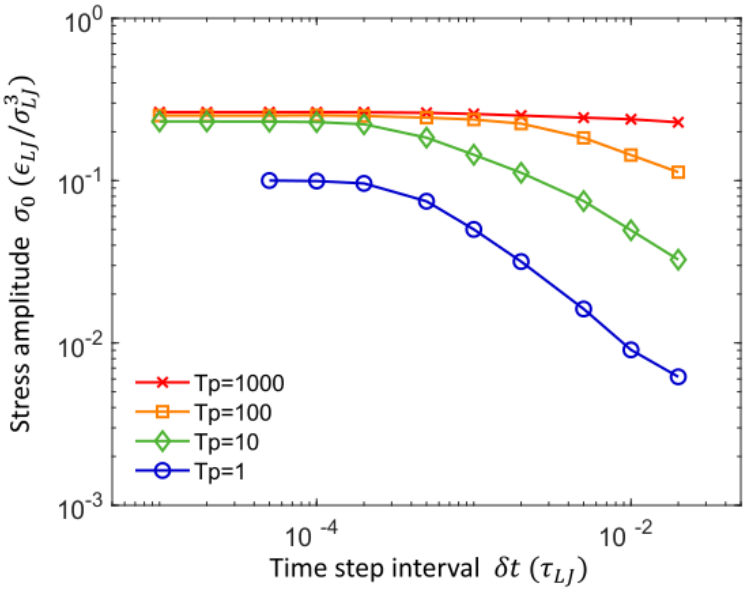

Fig. E.2 Stress amplitude against time step interval δt at various shearing periods (i.e. shear frequency).